



**Functional Characterization of the Bivalent Cation
Transporter 3 in *Arabidopsis thaliana* and *Hordeum vulgare***

Dissertation

zur Erlangung des

Doktorgrades der Naturwissenschaften (Dr. rer. nat.)

der

Naturwissenschaftlichen Fakultät III

Agrar- und Ernährungswissenschaften, Geowissenschaften
und Informatik

der

der Martin-Luther-Universität Halle-Wittenberg

vorgelegt von

Frau Jie He

geb. am 02.11.1991 in Zhangjiagang, Suzhou, Jiangsu, China

Halle (Saale), 20.12.2021

Gutachter:

1. Professor Dr. Edgar Peiter
2. Professor Dr. Patrick Gerd Bienert

Table of contents

Table of contents	i
List of abbreviations	vi
List of figures	xi
List of tables	xiv
1 Introduction.....	1
1.1 Manganese in plants.....	1
1.2 Manganese in the Golgi apparatus	2
1.3 Mn ²⁺ transport in <i>A. thaliana</i> and <i>H. vulgare</i>	10
1.3.1 Mn ²⁺ transport in <i>A. thaliana</i>	10
1.3.2 Mn ²⁺ transport in <i>Hordeum vulgare</i>	20
1.4 Generation of crop mutants by CRISPR-mediated mutagenesis	21
1.5 Objectives of this work	22
2 Materials and methods	23
2.1 Plasmids and constructs	23
2.2 Plant material	25
2.2.1 <i>A. thaliana</i> lines	25
2.2.1.1 Screening of <i>A. thaliana bicat3</i> mutants.....	25
2.2.1.2 <i>A. thaliana</i> complementation lines: <i>bicat3-1::gBICAT3</i>	25
2.2.1.3 <i>A. thaliana</i> promoter-GUS lines: <i>PrBICAT3-GUS</i>	26
2.2.1.4 <i>A. thaliana</i> complementation lines with Venus tag: <i>bicat3-1::PrBICAT3-BICAT3-Venus</i>	26
2.2.2 <i>H. vulgare bicat3</i> CRISPR mutants	27
2.2.2.1 Identification of HvBICAT3	27

2.2.2.2 Design of sgRNAs.....	27
2.2.2.3 Vector construction.....	28
2.2.2.4 <i>H. vulgare</i> transformation.....	29
2.2.2.5 Screening of <i>H. vulgare</i> mutants.....	30
2.3 Plant cultivation.....	32
2.3.1 Cultivation of <i>A. thaliana</i> on agar plates.....	32
2.3.2 Cultivation of <i>A. thaliana</i> in hydroponic nutrient solution.....	33
2.3.3 Cultivation of <i>H. vulgare</i> in hydroponic nutrient solution.....	33
2.3.4 Cultivation of <i>A. thaliana</i> and <i>H. vulgare</i> on soil.....	34
2.4 Histochemical GUS staining.....	34
2.5 Yeast complementation assays.....	35
2.6 Subcellular localization of BICAT3 and HvBICAT3.....	35
2.6.1 Subcellular localization of BICAT3.....	35
2.6.2 Ultrastructural localization of BICAT3-Venus.....	36
2.6.3 Subcellular localization of HvBICAT3.....	37
2.7 Reciprocal crossing of Arabidopsis.....	37
2.8 Arabidopsis pollen tube growth assays.....	38
2.8.1 Observation of BICAT3-Venus in pollen and pollen tubes.....	38
2.8.2 <i>In vivo</i> and <i>semi in vivo</i> pollen tube growth assays.....	38
2.8.3 Ruthenium red staining of pollen tubes.....	39
2.8.4 Immunostaining of pollen tubes.....	39
2.9 Seed size measurements.....	40
2.10 Seed germination assays.....	40
2.11 Photosynthesis measurements.....	40

2.12 Analysis of metal concentrations in plants.....	41
2.13 Analysis of metal concentrations in chloroplasts	42
2.14 Grafting	43
2.15 Leaf sectioning and cell size measurements.....	43
2.16 Callose detection	44
2.17 Glycoprotein assays.....	45
2.18 Monosaccharide and sugar linkage determination.....	46
3 Results I - The Golgi-localized Bivalent Cation Transporter3 determines manganese allocation and glycosylation of matrix polysaccharides	48
3.1 BICAT3 localizes to the Golgi apparatus and is ubiquitously expressed	48
3.2 BICAT3 acts as Ca ²⁺ and Mn ²⁺ transporter in yeast.....	50
3.3 Growth of <i>bicat3</i> mutants is differentially affected by Mn ²⁺ and Ca ²⁺ supply .	53
3.4 <i>bicat3</i> mutants accumulate a higher concentration of manganese in chloroplasts and have an improved photosynthesis under Mn ²⁺ deficiency	60
3.5 BICAT3 is essential for glycosylation and matrix polysaccharide biosynthesis under low Mn ²⁺ availability.....	65
3.6 Mutation of <i>BICAT3</i> hampers pollen tube growth and the development of siliques	70
3.7 <i>bicat3</i> pollen tubes accumulate less low methyl-esterified homogalacturonan compared to wild-type pollen tubes	74
4 Results II - Functional analysis of Golgi-localized HvBICAT3 using CRISPR/Cas9 genome editing in <i>H. vulgare</i>.....	77
4.1 BICAT proteins in <i>A. thaliana</i> and <i>H. vulgare</i>	77
4.2 HvBICAT3 localizes to the Golgi apparatus	78
4.3 HvBICAT3 acts as Ca ²⁺ and Mn ²⁺ transporter in yeast	79

4.4 Design of <i>HvBICAT3</i> editing targets and constructs.....	80
4.5 Generation of CRISPR/Cas9-mediated <i>hvbicat3</i> mutants.....	82
4.6 Selection of transgene-free homozygous <i>hvbicat3</i> mutants.....	84
4.7 The growth of <i>H. vulgare</i> is affected by mutation of <i>HvBICAT3</i>	89
5 Discussion.....	93
5.1 Functions of <i>BICAT3</i> and <i>HvBICAT3</i> in yeast	93
5.2 <i>BICAT3</i> is essential for Ca^{2+}/Mn^{2+} homeostasis in plants, especially the resistance to Mn^{2+} deficiency	95
5.3 <i>BICAT3</i> restricts manganese bioavailability for chloroplasts	96
5.4 <i>BICAT3</i> determines matrix polysaccharide biosynthesis	97
5.5 <i>BICAT3</i> determines pollen tube growth and seed set in <i>Arabidopsis</i>	101
5.6 Functional similarities and diversities of <i>BICAT3</i> and <i>HvBICAT3</i>	102
5.7 Efficient targeted mutagenesis of the <i>HvBICAT3</i> gene in <i>H. vulgare</i> via CRISPR/Cas9-mediated genome editing.....	104
6 Conclusions.....	107
7 Summary	108
8 Appendix.....	109
8.1 List of primers	109
8.2 List of constructs	110
8.3 Media composition	110
8.4 List of chemicals	113
8.5 List of enzymes	115
9 References	116
10 Bibliography.....	136

10.1 Peer-reviewed publications	136
10.2 Poster presentations.....	136
11 Curriculum Vitae	137
12 Acknowledgments	138
13 Declaration under Oath	139

List of abbreviations

µg	Microgram
µm	Micrometer
µM	Micromolar
µmol	Micromole
½ MS	Half-strength Murashige & Skoog medium
A	Alanine
AGPs	Arabinogalactan proteins
Amp	Ampicillin
AMP-FLP	Amplified fragment length polymorphism
Arabidopsis	<i>Arabidopsis thaliana</i> L. Heyn
ATP	Adenosine triphosphate
<i>A. tumefaciens</i>	<i>Agrobacterium tumefaciens</i>
BAK	BRI1-associated receptor kinase 1
Barley	<i>Hordeum vulgare</i>
BASTA	Glufosinate (Bayer Crop Science, Germany)
BICAT	Bivalent cation transporter
bp	Base pair
BR	Brassinosteroid
BRI1	Brassinosteroid insensitive 1
BSA	Bovine serum albumin
BS	Backscattering spectrometry
B4GALT1	β-1,4-galactosyltransferase 1
Ca	Calcium
[Ca ²⁺] _{cyt}	Cytosolic free calcium
Cas	CRISPR-associated proteins
CAX	Calcium exchanger
CCC	Calcium sensitive cross complementer
CCHA1	Chloroplast-localized Ca ²⁺ /H ⁺ Antiporter 1
CCX	Cation/calcium exchanger
CDF	Cation diffusion facilitator
cDNA	Complementary DNA
CDS	Coding sequence
CFP	Cyan fluorescent protein
cMCU	Chloroplast-localized mitochondrial calcium uniporter
Co	Cobalt
CO ₂	Carbon dioxide
ConA	Concanavalin A
COT1	Cobalt toxicity 1
CRISPR	Clustered regularly interspaced short palindromic repeats
CrRLK1L	Catharanthus roseus receptor like kinase 1-like
CT	Cytoplasmic tail

Cu	Copper
d	Day
D	Aspartic acid
DAPH	3-Deoxy-D-arabio-heptulosonate 7-phosphate
DMSO	Dimethyl sulfoxide
DNA	Desoxyribonucleic acid
DSB	Double strand break
DW	Dry weight
DTT	Dithiothreitol
DxD	Asp-[any amino acid]-Asp
E	Glutamic acid
ECA	ER-type calcium ATPase
<i>E. coli</i>	<i>Escherichia coli</i>
EDTA	Ethylene diamine tetraacetic acid
EGFP	Enhanced green fluorescent protein
EGTA	Ethylenglycol diamine tetraacetic acid
ER	Endoplasmic reticulum
EXT	Extensin
EYFP	Enhanced yellow fluorescent protein
Fe	Iron
FER	Feronia
FRO2	Ferric reduction oxidase 2
FUT11/12	α -1,3-fucosyltransferase
FUT13	α -1,4-fucosyltransferase
Fv/Fm	Maximal quantum yield of photosystem II (YII)
FW	Fresh weight
g	Gram
G	Glycine
GalA	Galacturonic acid
GALS	Galactan β -1,4-galactosyltransferase
GALT1	β -1,3-galactosyltransferase
GALT2-6	Hyp-O-galactosyltransferases
GAUT	Galacturonosyltransferase
GDH	Glutamate dehydrogenase
gDNA	Genomic DNA
GDT1	Gcr1-dependent translation factor1
Glc	Glucose
GlcA	Glucuronic acid
GNT1	N-acetylglucosaminyltransferase I
GM2	Golgi α -mannosidase
GNT2	N-acetylglucosaminyltransferase II
GTs	Glycosyltransferases
GUS	β -glucuronidase activity

GUX1	Glucuronic acid substitution of xylan 1
h	Hour
H ⁺	Proton
HDR	Homology-directed repair
HG	Homogalacturonan
H ₂ O ₂	Hydrogen peroxide
HPAT	Hydroxyproline O-arabinosyltransferase
HPGT	Hydroxyproline O-galactosyltransferase
HRGP	Hydroxyproline-rich glycoprotein
IAA	Indole-3-acetic acid
IAR3	IAA-alanine resistant 3
ICP-MS	Inductively coupled plasma-mass spectrometry
IGPD	Imidazole glycerol-phosphate dehydratase
Indels	Insertions or deletions
IPUT1	Inositol phosphoryl-ceramide glucuronosyl transferase 1
IRT	Iron-regulated transporter
IRX9	β-1,4-xylosyltransferase in xylan biosynthesis
JA	Jasmonate
K	Potassium
Kan	Kanamycin
LRXs	Leucine-rich repeat extensins
M	Molar
[Mn ²⁺] _{Golgi}	Golgi manganese
MCU	Mitochondrial Ca ²⁺ uniporter
MES	2-(N-morpholino) ethanesulfonic acid
Mg	Magnesium
mg	Milligram
MGP4	Male gametophyte defective 4
MICU1	Mitochondrial calcium uptake 1
min	Minute
mM	Milimolar
Mn	Manganese
MnSOD	Manganese superoxide dismutase
MNS1/2	Golgi-α-mannosidase I
MNS3	ER-type-α-mannosidase I
MP-AES	Microwave plasma atomic emission spectrometry
mRNA	Messenger RNA
MTP	Metal tolerance protein
NHEJ	Non-homologous end joining
NLS	Nuclear localization signal
N-terminus	Amino terminus
NBT	Nitro tetrazolium blue
ng	Nanogram

nM	Nanomolar
NRAMP	Natural resistance associated macrophage protein
O ₂	Oxygen
OEC	Oxygen-evolving complex
PAM	Protospacer adjacent motif
PAM71	Photosynthesis affected mutant 71
PAM71-HL	PAM71-homolog
PCR	Polymerase chain reaction
PGSIPs	Plant glycogenin-like starch initiation proteins
pH	Negative decadic logarithm of proton activity
PIXE	Particle-induced X-ray emission
PM	Plasma membrane
PME	Pectin methylesterase
PMEI	Pectin methylesterase inhibitor
PMR1	Plasma membrane ATPase related 1
Pr	Promoter
PS	Photosynthesis
PSII	Photosystem II
PVC	Pre-vacuolar compartment
qRT-PCR	Quantitative reverse transcription PCR
RG	Rhamnogalacturonan
rH	Relative humidity
RLP	Receptor-like protein
RNA	Ribonucleic acid
ROS	Reactive oxygen species
s	Second
S	Serine
<i>S. cerevisiae</i>	<i>Saccharomyces cerevisiae</i>
SERCA	Sarco/endoplasmic reticulum Ca ²⁺ -ATPase
sgRNA	Single guide RNA
SMF	Suppressor of mitochondria import function
SOD	Superoxide dismutase
SPCA	Secretory pathway Ca ²⁺ ATPase
SXRF	Synchrotron X-ray fluorescence
T	Threonine
TALENs	Transcription activator-like effectors
TCA	Citric acid cycle
T-DNA	Transfer DNA
TGN	Trans-Golgi network
TMD	Transmembrane domain
TMEM165	Transmembrane protein165
UPF0016	Uncharacterized protein family 0016
UTR	Untranslated region

VIT	Vacuolar iron transporter
WAK	Wall-associated kinase
WT	Wild type
x-Gluc	5-Bromo-4-chloro-3-indolyl- β -D-glucuronic acid
XXT1/2	Xyloglucan xylosyltransferases
Xyl	Xylose
XYLT	β -1,2-xylosyltransferase
ZFNs	Zinc finger nucleases
ZIP	Zinc-regulated, Iron-regulated transporter-like protein
Zn	Zinc
ZRC1	Zinc resistance conferring 1
ZRT	Zinc Regulated Transporter

List of figures

Figure 1. Mn ²⁺ and Ca ²⁺ dependence of glycosylation in the Golgi.	5
Figure 2. Intracellular transport proteins for Ca ²⁺ and Mn ²⁺ in Arabidopsis.....	13
Figure 3. Workflow of <i>Hvbicat3</i> mutant screening from T0 generation to the homozygous T2 generation	31
Figure 4. Golgi-localized BICAT3 has a ubiquitous expression in <i>A. thaliana</i>	49
Figure 5. BICAT3 does not co-localize with mitochondria and peroxisomes.	50
Figure 6. GUS staining of ProBICAT3-GUS seedlings grown under different Mn ²⁺ and Ca ²⁺ supply.	50
Figure 7. <i>BICAT3</i> complements Ca ²⁺ - and Mn ²⁺ -sensitive yeast strains.	51
Figure 8. BICAT3 does not complement Fe-sensitive (<i>ccc1Δ</i>), Zn-sensitive (<i>zrc1Δ</i>), Cu-sensitive (<i>cup2Δ</i>) and Co-sensitive (<i>cot1Δ</i>) yeast strains.	52
Figure 9. Genotypic characterization of <i>bicat3</i> mutants.....	53
Figure 10. <i>bicat3-1</i> shows retarded growth compared to the wild type under Mn ²⁺ deficiency (0 μM MnSO ₄).....	55
Figure 11. <i>bicat3-1</i> shows retarded root growth compared to the wild type under Ca ²⁺ toxicity (50 mM CaCl ₂).....	56
Figure 12. <i>bicat3-1</i> shows improved growth compared to the wild type under Mn ²⁺ toxicity (1 mM MnSO ₄).....	57
Figure 13. <i>bicat3-1</i> and wild type growth phenotype under different Ca ²⁺ and Mn ²⁺ supply.	58
Figure 14. Phenotypes of Col-0, <i>bicat3-1</i> , and <i>bicat3-2</i> under control and Mn ²⁺ deficiency (0.05 μM MnSO ₄) conditions.....	59
Figure 15. Absence of BICAT3 causes higher Mn content of chloroplasts and improved photosynthesis compared to the wild type under Mn ²⁺ deficiency (0.05 μM MnSO ₄).....	61
Figure 16. Phenotypes of Col-0 and <i>bicat3-1</i> under different Mn ²⁺ (MnSO ₄) supply levels.	62

Figure 17. Phenotypes of Col-0 and <i>bicat3-1</i> reciprocally grafted plants under control and Mn ²⁺ deficiency (0.05 μM MnSO ₄) conditions.	64
Figure 18. The cell size and shape of <i>bicat3-1</i> leaves change under Mn ²⁺ deficiency (0.05 μM MnSO ₄) compared to the wild type.	66
Figure 19. Cell wall matrix sugar components are affected in <i>bicat3</i> shoots compared to the wild type under Mn ²⁺ deficiency (0.05 μM MnSO ₄).	67
Figure 20. <i>bicat3-1</i> accumulates more callose in leaves compared to the wild type under Mn ²⁺ deficiency (0.05 μM MnSO ₄).	68
Figure 21. Glycoprotein pattern of <i>bicat3-1</i> shoots is altered by Mn ²⁺ deficiency (0.05 μM MnSO ₄) in <i>bicat3</i> mutants.	69
Figure 22. <i>bicat3-1</i> and <i>bicat3-2</i> mutants produce shorter siliques compared to the wild type.	70
Figure 23. The <i>bicat3-1</i> mutant shows male gametophyte defects that lead to shorter siliques compared to the wild type.	71
Figure 24. The <i>bicat3-1</i> mutant produces bigger seeds and germinates faster than the wild type.	72
Figure 25. The absence of <i>BICAT3</i> hampers pollen tube growth.	73
Figure 26. <i>Semi in vivo</i> pollen tube growth assays of Col-0, <i>bicat3-1</i> , <i>bicat3-2</i> , and complementation line (Comp) of <i>bica3-1</i> mutant.	74
Figure 27. <i>bicat3</i> mutant pollen tubes grow aberrantly <i>in vitro</i> and show abnormal pectin distribution.	75
Figure 28. <i>bicat3</i> mutant pollen tubes contain less low methyl-esterified homogalacturonan compared to the wild type.	76
Figure 29. HvBICAT3 is similar to BICAT3.	78
Figure 30. HvBICAT3 is localized in the Golgi apparatus.	79
Figure 31. HvBICAT3 complements a Ca ²⁺ -sensitive yeast strain, and partially a Mn ²⁺ -sensitive yeast strain.	80
Figure 32. Targets and vectors for CRISPR/Cas9-mediated mutagenesis of <i>HvBICAT3</i>	81

Figure 33. Screening of T0 generation mutants of <i>HvBICAT3</i>	83
Figure 34. Screening of T1 generation mutants of <i>HvBICAT3</i> for large deletions by PCR.....	85
Figure 35. Verification of T1 generation mutants of <i>HvBICAT3</i> by EcoRV restriction.....	86
Figure 36. PCR amplification of a <i>Cas9</i> fragment to screen for transgene-free progenies of T1 generation mutants of <i>HvBICAT3</i>	87
Figure 37. Mutations detected in DNA from leaves of some T1 generation <i>hvbicat3</i> mutants.....	88
Figure 38. SpCas9-induced frame-shift mutations in <i>HvBICAT3</i> lead to premature STOP codons and mutated protein sequences.	88
Figure 39. Exemplary sequence alignments of T2 progenies of <i>hvbicat3_10-3</i> and <i>hvbicat3_14-7</i> mutants.	89
Figure 40. Ears of wild type (WT) and <i>hvbicat3</i> mutants.	90
Figure 41. Growth phenotypes of <i>hvbicat3</i> mutants and wild type (WT) under control and Mn ²⁺ deficiency conditions.	90
Figure 42. <i>hvbicat3</i> mutants produce curly leaves under Mn deficiency.....	91
Figure 43. Second youngest leaves of <i>hvbicat3</i> mutants contain more Mn and have better photosynthesis compared to wild type (WT) under Mn ²⁺ deficiency.....	92

List of tables

Table 1. Frequency of types of T0 generation mutants of <i>HvBICAT3</i>	84
Table 2. Mutation rate of targets in T0 generation plants.	84
Table 3. List of primers used in this study.	109
Table 4. List of constructs used in this study.	110
Table 5. Media for <i>H. vulgare</i> tissue culture.	110
Table 6. Media for <i>E. coli</i> , <i>A. tumefaciens</i> , and <i>S. cerevisiae</i> culture.	111
Table 7. Media for <i>A. thaliana</i> and <i>H. vulgare</i> culture.	112
Table 8. List of chemicals used in this study.	113
Table 9. List of enzymes used in this study.	115

1 Introduction

1.1 Manganese in plants

Manganese (Mn) is an essential trace metal for plants (Andresen et al., 2018). It functions in diverse processes during plant growth and development as a cofactor of enzymes or a catalytic metal in clusters (Alejandro et al., 2020). One of the most prominent roles of Mn^{2+} is to constitute the Mn_4O_5Ca catalytic cluster in the oxygen-evolving complex (OEC) of photosystem II (PSII) for water oxidation, and consequently the supply of electrons and protons for the photosynthetic electron transport chain and ATP production, respectively. Furthermore, thylakoid-associated phosphatase38 (TAP38/PPH1), which is critical for state transition between PSI and PSII, requires a binuclear Mn^{2+} or Mg^{2+} center (Wei et al., 2015). Some chloroplast-localized enzymes involved in the synthesis of amino acids, carotenoids, chlorophyll, and gibberellins also require Mn^{2+} for their functions, for instance, Imidazole Glycerol-Phosphate Dehydratase (IGPD) (Bisson et al., 2015), 3-deoxy-D-arabino-heptulosonate 7-phosphate (DAPH) synthase (Entus et al., 2002), phytoene synthetase, mevalonic kinase, and *ent*-kaurene synthetase (Dogbo et al., 1988; Rohdich et al., 2006).

Besides the roles of Mn^{2+} in chloroplasts, it is also involved in scavenging of Reactive Oxygen Species (ROS) as a component of mitochondria- and peroxisome-localized Manganese Superoxide Dismutase (MnSOD) (He et al., 2021). In addition, mitochondrial arginases are Mn^{2+} -containing enzymes, functioning in hydrolyzing arginine to ornithine and urea (Cao et al., 2010). They are also engaged in crosstalk between arginine metabolism and the accumulation of polyamines and nitric oxides (NO) in abiotic stress signaling pathways (He et al., 2021). Moreover, Mn^{2+} is critical for phytohormone balance, as it is a cofactor of auxin amidohydrolases in the endoplasmic reticulum, which are substantial for auxin activation (LeClere et al., 2002). IAA-Alanine Resistant 3 (IAR3), one of the *A. thaliana* auxin amidohydrolases, also plays a role in jasmonate (JA) signaling

since it hydrolyzes the bioactive form of JA (JA-Ile) (Widemann et al., 2013). The function of Mn^{2+} in the Golgi apparatus will be described in detail in the following section.

1.2 Manganese in the Golgi apparatus

This section has been published in: He J, Rössner N, Hoang MTT, Alejandro S, Peiter E (2021) Transport, functions, and interaction of calcium and manganese in plant organellar compartments. *Plant Physiology*, DOI: 10.1093/plphys/kiab122. The section has been written by Jie He.

The Golgi apparatus is a hub of the secretory pathway, and ion homeostasis of this compartment is important for the function of the entire plant cell (Hawes and Satiat-Jeunemaitre, 2005). As cofactor of glycosyltransferases (GTs), Mn^{2+} plays a pivotal role in glycosylation reactions in the Golgi apparatus (Nagashima et al., 2018). GTs are classified into three groups based on their three-dimensional folds, GT-A, GT-B, and GT-C (Moremen and Haltiwanger, 2019). Most of the GT-A fold enzymes contain conserved DxD (Asp-[any amino acid]-Asp) motifs which interact with the phosphate group of the nuclear sugar donor through the coordination of a divalent cation, which is typically Mn^{2+} (Breton et al., 2006). Although no DxD motif exists in GT-B fold GTs, some of them require a divalent cation for their optimal activity (Breton et al., 2006). For instance, additional Mn^{2+} strongly enhances the catalytic activity of a fucosyltransferase by increasing its affinity to receptors, even though the divalent cation is not absolutely essential for its enzymatic activity (Palma et al., 2004).

In all eukaryotes, GTs modify proteins in a complex and coordinated way (Nguema-Ona et al., 2014; Schoberer and Strasser, 2018). Thereby, *N*-linked protein glycosylation is initiated in the ER. The intermediate *N*-glycans are

transmitted to the *cis*-Golgi and processed further by ER-type- α -mannosidase I (MNS3) to remove a mannose residue, followed by maturation while progressing through the Golgi stack from *cis*- to *trans*-face. This is accomplished by Golgi- α -mannosidase I (MNS1 and MNS2), *N*-acetylglucosaminyltransferase I (GNT1), Golgi β -mannosidase (GM2), *N*-acetylglucosaminyltransferase II (GNT2), β -1,3-fucosyltransferase (FUT11 and FUT12), β -1,2-xylosyltransferase (XYLT), β -1,3-galactosyltransferase (GALT1), and β -1,4-fucosyltransferase (FUT13) (Nagashima et al., 2018). Among them, some have been shown to coordinate Mn^{2+} for their catalytic activity (Figure 1A), and mutants of them show abnormal growth phenotypes. Extensins (EXTs) and arabinogalactan proteins (AGPs) are two major O-glycosylated protein components of the plant cell wall. They belong to the hydroxyproline-rich glycoprotein (HRGP) superfamily and account for around 10% of cell wall dry weight.

The *N*- and O-glycosylation of proteins and lipids is essential for plant development and stress responses (Kobayashi, 2016; Nagashima et al., 2018; Huby et al., 2020; Mortimer and Scheller, 2020; Seifert, 2020; Silva et al., 2020). Arabinogalactan proteins (AGPs) have been proposed to represent Ca^{2+} capacitors that reversibly bind and release apoplastic Ca^{2+} in a pH-dependent manner by their β -linked glucuronic acid (GlcA) residues and which thereby determine numerous biological processes, such as pollen tube growth and guidance, seedling growth, and Ca^{2+} oscillations in roots (Lampert et al., 2018; Lopez-Hernandez et al., 2020). Accordingly, mutants of Mn^{2+} -dependent Hyp-O-galactosyltransferases (GALT2-6) that are involved in AGP biosynthesis (Figure 1A), show defects in root, leaf, and pollen tube growth (Basu et al., 2015; Basu et al., 2015). Based on the Uniprot database (www.uniprot.org), some further *A. thaliana* GTs involved in O-glycosylation are predicted to contain a DxD motif or to bind Mn^{2+} by sequence similarity (Figure 1A).

Unlike protein glycosylation, the synthesis of matrix polysaccharides (pectin and hemicellulose) takes place exclusively in the Golgi. Some of the *A. thaliana*

GTs involved in this process have been described to work in a Mn^{2+} -dependent manner (Figure 1B). Matrix sugars account for two thirds of the *A. thaliana* primary cell wall, contribute substantially to the mechanical properties of it, and are thus critical for plant growth and development (Gigli-Bisceglia et al., 2020). Similar to dicot plants, graminaceous plants encompass considerable amounts of matrix sugars in the primary cell wall (Gigli-Bisceglia et al., 2020). Nevertheless, the proportions of certain matrix sugars are different in the cell wall of graminaceous and non-graminaceous plants. For instance, pectins account for 2–10% of the primary cell wall of grasses, while 35% of the primary cell wall of dicots is made of pectin (Mohnen, 2008).

Xyloglucans interact with cellulose and form a load-bearing structure of the cell wall. They are necessary for wall extensibility, organ formation, and meristem profile and phyllotaxis (Park and Cosgrove, 2012; Rui and Anderson, 2016; Zhao et al., 2019). Golgi-localized Xyloglucan Xylosyltransferases (XXT1 and 2) are Mn^{2+} -dependent and involved in xyloglucan biosynthesis (Culbertson et al., 2016; Culbertson et al., 2018). The *xxt1xxt2* double mutant is smaller than the wild type in shoot size, with a diminished amount and abnormal composition of xyloglucans. Biosynthesis of cell wall sugars might be mutually affected, as *xxt1xxt2* not only displays a defect in xyloglucan production but also in cellulose production and pectin methylation at the shoot apical meristem (Zhao et al., 2019). Another class of matrix sugars, pectins, play pivotal roles in a plethora of biological processes, including cell adhesion (Bouton et al., 2002; Smithers et al., 2019), morphogenesis of epidermal cells (Altartouri et al., 2019; Haas et al., 2020), organ formation (Peaucelle et al., 2011), shoot and root elongation (Bouton et al., 2002; Kim et al., 2015), pollen tube growth (Kim et al., 2015; Lund et al., 2020), fertilization (Duan et al., 2020), photosynthesis (Weraduwage et al., 2016), and stomatal functions (Amsbury et al., 2016; Yi et al., 2018; Rui et al., 2019), and pectins also confer tolerance to biotic and abiotic stresses (Bacete et al., 2018; Wu et al., 2018; De Lorenzo et al., 2019; Gigli-Bisceglia et al., 2020).

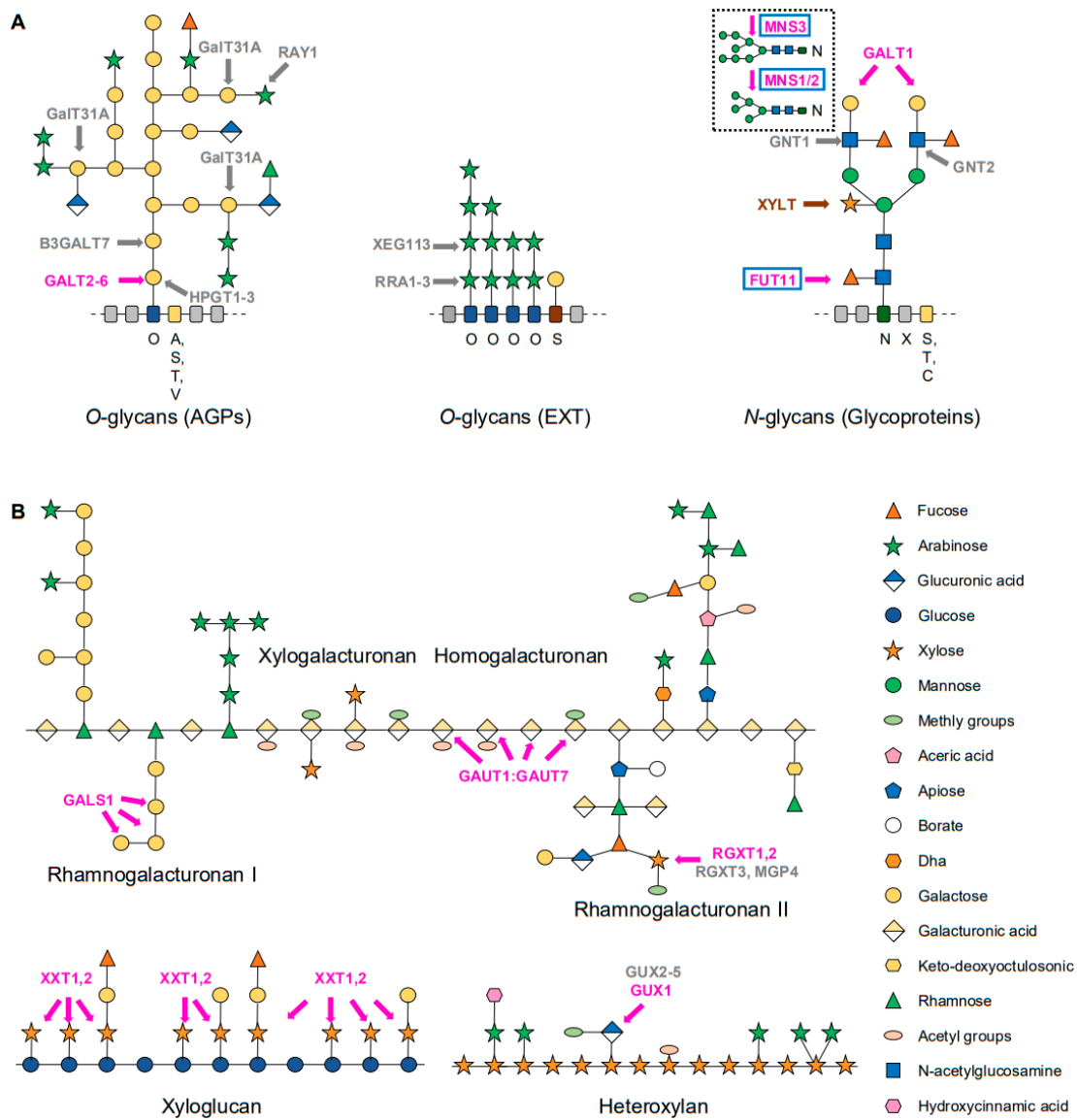


Figure 1. Mn^{2+} and Ca^{2+} dependence of glycosylation in the Golgi.

Enzymes are either marked in magenta for those experimentally confirmed to require Mn^{2+} or in grey for those predicted to be Mn^{2+} -dependent. Enzymes that are also activated by Ca^{2+} are marked by blue boxes. An enzyme that does not absolutely depend on Mn^{2+} is marked in brown. A, Schematic representation of enzymes involved in synthesis of O-glycans attached to plant arabinogalactan proteins (AGP) and extensins (EXT), and specific complex-type N-glycans attached to plant glycoproteins. The glycan models presented are modified from Nguema-Ona et al. (2014) and Showalter and Basu (2016). Among those core enzymes of deglycosylation (insert) and glycosylation, ER-type- α -mannosidase I (MNS3), Golgi- α -mannosidase I (MNS1 and MNS2) (Liebminger et al., 2009), and α -1,3-fucosyltransferase (FUT11) (Both et al., 2011) are activated by Ca^{2+} or Mn^{2+} . β -1,2-xylosyltransferase (XYLT) (Pagny et al., 2003), β -1,3-galactosyltransferase (GALT1) (Strasser et al., 2007), and hydroxyproline O-galactosyltransferase (GALT2,3,4,5,6) (Basu et al., 2015) are reported to coordinate Mn^{2+} for their catalytic activity. Activity of XYLT is stimulated or inhibited by Mn^{2+} (Bencúr et al., 2005). Based on the Uniprot database (www.uniprot.org), some

further Arabidopsis GTs involved in *N*- or *O*-glycosylation are predicted to contain a DxD motif or to bind Mn^{2+} by sequence similarity, i.e., β -1,2-N-acetylglucosaminyltransferase (GNT1 and 2), β -1,2-arabinosyltransferase (RRA1,2,3 and XEG113), hydroxyproline-*O*-galactosyltransferase (HPGT1,2,3), β -1,3-galactosyltransferase (B3GALT7), β -1,6-galactosyltransferase (GALT31A), and β -arabinofuranosyltransferase (RAY1). B, Schematic representation of enzymes involved in the synthesis of matrix sugars of the plant cell wall. The structures of matrix sugars are modified from Burton et al. (2010). Enzymes shown to require Mn^{2+} are galactan synthase 1 (AtGALS1) that catalyzes the addition of galactose from UDP- α -D-Gal to β -1,4-galactan chains of rhamnogalacturonan I and the transfer of an arabinopyranose from UDP- β -L-Ara_p to galactan chains (Ebert et al., 2018; Laursen et al., 2018); a polygalacturonate (1,4)- α -D-galacturonosyltransferase complex (GAUT1:GAUT7) that catalyzes the transfer of galacturonic acid onto the homogalacturonan (Amos et al., 2018); (1,3)- α -D-xylosyltransferases (AtRGXT1 and 2) that synthesize rhamnogalacturonan-II (RG II) (Egelund et al., 2006; Petersen et al., 2009); xyloglucan xylosyltransferases (XXT1 and 2) that are involved in xyloglucan biosynthesis (Culbertson et al., 2016; Culbertson et al., 2018); and GUX1 that adds GlcA to xylan (Rennie et al., 2012). In addition, based on the Uniprot database (www.uniprot.org), further Arabidopsis GTs involved in matrix sugar biosynthesis are predicted to contain a DxD motif or to bind Mn^{2+} by sequence similarity, i.e. rhamnogalacturonan α -1,3-D-xylosyltransferase (MGP4 and RGXT3) for RGII biosynthesis, and UDP-GlcA:xylan glucuronyltransferase (GUX2,3,4,5) for heteroxylan biosynthesis. Figure taken from He et al. (2021).

Eight Plant Glycogenin-like Starch Initiation Proteins (PGSIPs) exist in *A. thaliana*, of which PGSIP1 to 5 were later annotated as Glucuronic acid sUbsitution of Xylan 1 (GUX1) through 5, respectively. Albeit initially believed to be involved in starch synthesis, *GUX1* encodes a glucuronosyltransferase mediating the addition of GlcA to xylan and requiring Mn^{2+} for its catalytic activity (Rennie et al., 2012). Another member of this protein family, PGSIP6/IPUT1/MOCA1, is a showcase example for a Mn^{2+} -dependent glycosylation process playing multiple crucial roles in signaling and development. Using the same sugar donor as GUX1, PGSIP6 catalyzes the transfer of a GlcA residue to glycosyl inositol phosphoryl ceramide (GIPC) sphingolipids and hence was renamed to Inositol Phosphoryl-ceramide gLUcuronosyl Transferase 1 (IPUT1) (Rennie et al., 2014). GIPCs are abundant in the plasma membrane, where they make up about a quarter of the total lipids, and also reside in tonoplast and ER membranes. Homozygous *iput1* T-DNA insertional loss-of-function mutants are

lethal (Rennie et al., 2014), but expression of *IPUT1* under a pollen-specific promoter in an *iput1* knockout line allowed to generate pollen-specifically rescued homozygous *iput1* mutants (Tartaglio et al., 2017). These mutants contain fewer GIPCs and a severely altered sphingolipidome, and showed severe dwarfism, compromised pollen tube guidance and constitutive activation of salicylic acid-mediated defense pathways, indicating important roles of GIPC sphingolipid glycosylation.

Based on its homology to GUX1, PGSIP6/IPUT1/MOCA1 is bound to be Mn^{2+} -dependent, which has yet to be confirmed experimentally. In this respect, it is interesting to note that Bian et al. (2018) identified a mutant of this gene in a screen for hypersensitivity to low Mn^{2+} supply. This mutant contains a non-synonymous point mutation which, however, is not close to the Mn^{2+} -binding site of the protein, but which may cause a partial loss in enzymatic activity, leading to the Mn^{2+} -dependent growth defect. It is unclear whether the mutant protein requires higher $[Mn^{2+}]_{Golgi}$ to function, or whether Mn^{2+} may even have a regulatory role. Finally, the most recent characterization of the PGSIP6/IPUT1/MOCA1 protein combines this role of Mn^{2+} with Ca^{2+} signaling. Intriguingly, a mutant called *moca1* (*monovalent cation-induced $[Ca^{2+}]_i$ increase 1*) that carries a four-amino acid-deletion in PGSIP6/IPUT1/MOCA1, was identified in a screen for aberrant $[Ca^{2+}]_{cyt}$ signals in response to salt (Na^+) stress (Jiang et al., 2019). Transient $[Ca^{2+}]_{cyt}$ elevation is an early and essential response to salt stress (Dodd et al., 2010). However, the Na^+ sensor in plants has been unknown. Due to the abolished Na^+ -triggered $[Ca^{2+}]_{cyt}$ signal in the *moca1* mutant, GIPCs synthesized by the PGSIP6/IPUT1/MOCA1 protein are believed to fulfill this role by coordinating Na^+ to gate Ca^{2+} influx channels (Jiang et al., 2019). Taken together, this implies that Na^+ sensing, Ca^{2+} signal generation, and hence salt tolerance, depend on a correct Mn^{2+} supply to the Golgi. Furthermore, based on the multitude of reported phenotypes in mutants of *PGSIP6/IPUT1/MOCA1*, it remains to be confirmed

whether its enzymatic product indeed functions as Na^+ sensor, or whether its role is more indirect.

The requirement of bivalent cations by GTs is likely to be more complex as generally anticipated, as the concentration of the cation is an important factor, and in some cases, cations can act in an inhibitory way. For instance, the activity of GALT5 is enhanced by Mn^{2+} but inhibited by Ca^{2+} (Basu et al., 2015). Besides, the activity of XylIT, which does not absolutely depend on metal ion cofactors, is enhanced by 1 mM Mn^{2+} , while higher Mn^{2+} concentrations are inhibitory (Bencúr et al., 2005). Cation concentrations and interactions in the Golgi thus appear to modulate, or even regulate GT enzymes.

The synthesis of complex matrix sugars and glycan chains of glycoproteins and glycolipids demands a meticulous spatial arrangement and coordination of enzymes in Golgi compartments. Compartmental organization of cell wall biosynthesis and sub-compartmental organization of Golgi-resident *N*-glycan processing enzymes have been studied over decades (Dunphy and Rothman, 1985; Zhang and Staehelin, 1992; Schoberer and Strasser, 2011; Driouich et al., 2012; Schoberer et al., 2013). The sub-compartmental localization of GTs corresponds to the sequential elongation of oligosaccharide chains. It is highly associated with the CTS region (comprised of cytoplasmic tail (CT), transmembrane domain (TMD) and stem region) of the proteins, but is not only determined by it (Saint-Jore-Dupas et al., 2006). GTs also form homodimers or heterodimers, which are required for the right subcellular localization and efficient production in the Golgi (Atmodjo et al., 2013; Schoberer et al., 2013; Zeng et al., 2016). Recently, heterogeneous localization of a GT enzyme and its products has even been revealed on the level of individual Golgi cisternae. A xylan backbone biosynthetic protein, IRX9, was shown to be localized specifically in the inner margin of *medial*-Golgi cisternae, whereas its product, xylan, localized mostly in the outer margin of *trans*-Golgi cisternae, indicating a distinct localization of synthesis and packing of xylan within Golgi cisternae (Meents et al., 2019).

Whether such nanoscale heterogeneities are accompanied by heterogeneities of cations that regulate the biosynthetic enzymes as well as the vesicular trafficking of their products is unknown but to be expected.

There is evidence that the Golgi and TGN take in a central position in subcellular Mn^{2+} allocation. In yeast, Smf2, a transporter belonging to the Natural Resistance Associated Macrophage Protein (NRAMP) family, is assumed to be crucial for releasing Mn^{2+} from vesicular compartments (*trans*-Golgi and late endosomes) to the cytosol (Garcia-Rodriguez et al., 2015), whereby Mn^{2+} can subsequently be transferred to the mitochondria by unknown transporters and to the Golgi by Pmr1. Accordingly, an *smf2* Δ mutant exhibits reduced SOD2 activity and Mn^{2+} accumulation in mitochondria, and a defective glycosylation of secreted invertase (Luk and Culotta, 2001). In *A. thaliana*, the TGN-localized NRAMP2 is believed to be functionally epistatic to NRAMP3 and NRAMP4, two vacuolar Mn^{2+} and Fe^{2+} transporters, involved in redistribution of Mn^{2+} to vacuoles and chloroplasts under Mn^{2+} deficiency (Alejandro et al., 2017). Mutants for *NRAMP2* show reduced photosynthesis and Mn^{2+} concentrations in chloroplasts and vacuoles. Based on a model put forward by Krieger-Liszkay and Thomine (2018), Mn^{2+} released from TGN and vacuole to cytosol can be subsequently translocated to the chloroplast stroma by Bivalent Cation Transporter 2 (BICAT2) and further imported by BICAT1 to the thylakoid lumen to supply the water-splitting complex and maintain photosynthetic efficiency under Mn^{2+} deficiency. This implies that vesicular compartments are essential for inter-organellar Mn^{2+} distribution.

Studies in the animal field suggest a crucial role of the Golgi in Mn^{2+} storage and detoxification. By combining synchrotron X-ray fluorescence (SXRF) nanoprobe with particle-induced X-ray emission (PIXE) microanalysis and backscattering spectrometry (BS), Carmona et al. (2010) observed an accumulation of Mn^{2+} within the Golgi of PC12 dopaminergic cells at physiological concentrations, and a further increase of the Golgi-allocated fraction when cells were exposed to 100 μ M $MnCl_2$, a sub-cytotoxic level. Upon exposure to toxic

concentrations, Mn^{2+} was also detected in cytoplasm and nucleus. Based on monitoring the subcellular distribution of Mn^{2+} in living HEK293T cells by a fluorescent Mn^{2+} sensor and by nano-SXRF imaging, Das et al. (2019) obtained evidence that the Golgi, besides its function as a Mn^{2+} storage organelle under physiological conditions, has an additional role in trafficking under sub-cytotoxic Mn^{2+} conditions. No direct measurement of compartmental Mn^{2+} concentrations has been conducted in plants yet. However, a crucial role of the Golgi in Mn^{2+} detoxification has been inferred from the Mn^{2+} -hypersensitive phenotype of the Golgi-localized Mn^{2+} transporter MTP11 (Peiter et al., 2007). It would be highly interesting to develop genetically encoded Mn^{2+} indicators to monitor the subcellular Mn^{2+} distribution under different levels of Mn^{2+} supply. In analogy to genetically encoded Ca^{2+} indicators, specificity to Mn^{2+} may be conferred by a Mn^{2+} -specific binding domain, for example from the cyanobacterial Mn^{2+} sensor MntS (Yamaguchi et al., 2002). In combination with a more complete inventory of Golgi-localized Mn^{2+} transport proteins, this would help to elucidate poorly understood plant Golgi functions, such as different Mn^{2+} requirements of complex glycosylation processes, inter-organellar Mn^{2+} transit, Mn^{2+} storage and detoxification, and, in particular, Mn^{2+} - Ca^{2+} interactions.

1.3 Mn^{2+} transport in *A. thaliana* and *H. vulgare*

1.3.1 Mn^{2+} transport in *A. thaliana*

This section has been partially published in: He J, Rössner N, Hoang MTT, Alejandro S, Peiter E (2021) Transport, functions, and interaction of calcium and manganese in plant organellar compartments. *Plant Physiology*, DOI: 10.1093/plphys/kiab122. The published parts have been written by Jie He.

Mn is present in many oxidation states in soil, among which Mn^{2+} is the only plant-available form. Plenty of factors affect the Mn dynamics in soil and thus its availability for plants, e.g. pH, oxygen level, organic molecules, plant root exudates (protons, carboxylates, enzymes), and the existence of Mn-oxidizing and Mn-reducing microorganisms (Alejandro et al., 2020). Mn^{2+} deficiency is prevalent in plants growing on dehydrated, well-aerated, and alkaline soils, whereas Mn^{2+} toxicity is prevalent in muddy and acidic soils. Both Mn^{2+} toxicity and deficiency are detrimental to the development and reproduction of plants (Marschner, 2012). Mn^{2+} toxicity is easy to notice by the most typical symptoms of chlorotic leaves and necrotic spots (Millaleo et al., 2010). In contrast, short- and mid-term Mn^{2+} deficiency occurs as a latent disorder without apparent symptoms. However, such a latent deficiency can be detected by measuring photosynthetic performance parameters such as maximal quantum yield (F_v/F_m) of photosystem II (YII) and the fluorescence induction curve (OJIP curve) (Schmidt et al., 2016; Schmidt et al., 2020). The MnSOD activity stayed unchanged while the photosynthetic activity was affected in *A. thaliana* under Mn^{2+} starvation (Lanquar et al., 2010), implying a disparate allocation of Mn^{2+} between cellular compartments for Mn^{2+} -dependent processes (Alejandro et al., 2020).

Mn^{2+} transport in plants has been covered comprehensively in Alejandro et al. (2020), and the interaction with Ca^{2+} transport has been reviewed in detail by He et al. (2021). Due to the similar ionic radii and binding coordination of Mn^{2+} and Ca^{2+} , transport proteins of many families discriminate poorly between the two cations (Figure 2). In plants, primary active transport of Ca^{2+} is mediated by P_{2A} - and P_{2B} -type ATPases, called ECAs (ER Ca^{2+} -ATPases) and ACAs (Autoinhibited Ca^{2+} -ATPases), respectively. The former also transport Mn^{2+} , and the latter are feedback-regulated by a Ca^{2+} /calmodulin-binding autoinhibitory domain. Those pumps have recently been reviewed by Bossi et al. (2020).

A large number of secondary active transporters, belonging to different families, contribute to organellar Ca^{2+} and Mn^{2+} homeostasis. The Calcium

Exchanger (CAX) family, reviewed by Pittman and Hirschi (2016), contains both Ca^{2+} -specific transporters and those transporting Ca^{2+} and Mn^{2+} ; both are energized by H^+ antiport (Waight et al., 2013). The Bivalent Cation Transporter (BICAT) family, with its chloroplast-localized members BICAT1 and BICAT2, has been identified only recently as a family of $\text{Ca}^{2+}/\text{Mn}^{2+}$ transport proteins (Uncharacterized Protein Family 0016, UPF0016) with a yet unresolved transport mechanism (Thines et al., 2020). Members of the Cation Diffusion Facilitator (CDF) family, called Metal Tolerance Proteins (MTPs) in plants, mediate the H^+ -driven active export of metals, including Mn^{2+} , out of the cytosol into organelles (Montanini et al., 2007; Gustin et al., 2011; Ricachenevsky et al., 2013). Transport of Mn^{2+} , besides Fe^{2+} , into the vacuolar organelle is also mediated by transporters of the Vacuolar Iron Transporter (VIT) family (Kim et al., 2006). NRAMP proteins, in turn, import metals, including Mn^{2+} , from the apoplast or from organelles into the cytosol (Nevo and Nelson, 2006). The ZRT, IRT-like Protein (ZIP) family also harbors proteins transporting Mn^{2+} across organellar membranes (Milner et al., 2013).

In *A. thaliana*, Mn^{2+} is acquired by the high-affinity transporter NRAMP1 and may also enter the root in high amounts via the Fe^{2+} uptake transporter Iron-Regulated Transporter1 (IRT1). However, the pathway of xylem loading and translocation of Mn^{2+} in dicots is dubious (Alejandro et al., 2020). A loss-of-function mutant of plasma membrane-localized ZIP2, which is mainly expressed in the root stele, showed tolerance to Mn^{2+} toxicity and increased accumulation of Mn^{2+} in roots under Mn^{2+} toxicity, suggesting a role of ZIP2 in loading Mn^{2+} into the root stele for subsequent root-to-shoot translocation (Milner et al., 2013). Plants have different mechanisms to tolerate high Mn^{2+} levels, e.g. by sequestration in organellar compartments, or deposition in the cell wall and in trichomes (Alejandro et al., 2020).

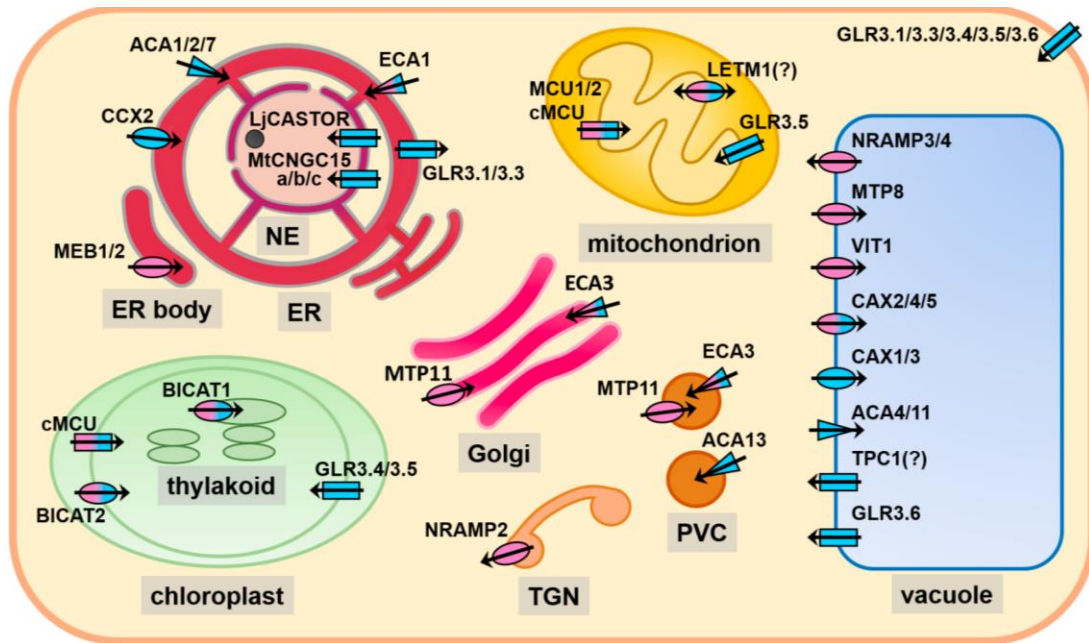


Figure 2. Intracellular transport proteins for Ca^{2+} and Mn^{2+} in Arabidopsis

Organelle pumps (triangles), transporters (ellipses), and channels (rectangles) that were experimentally shown to permeate Ca^{2+} (blue), Mn^{2+} (magenta), or both (blue/magenta) are displayed in a hypothetical plant cell. Only *A. thaliana* proteins are shown, except for LjCASTOR and MtCNGC15s, for which a function of the *A. thaliana* homologs as Ca^{2+} channels has not been examined yet. Note that the absence of an experimentally confirmed substrate, e.g. Mn^{2+} in the case of Ca^{2+} channels (GLR, CNGC, TPC1) does not exclude its permeation. Conductance of Mn^{2+} by (c)MCUs is inferred from their mammalian homologs. The permeation of Ca^{2+} by NRAMPs can be excluded on a structural basis, as discussed in the text. ER, endoplasmic reticulum; NE, nuclear envelope; PVC, pre-vacuolar compartment; TGN, trans-Golgi network. Figure taken from He et al. (2021).

Intracellularly, Mn^{2+} may be sequestered in vacuoles by CDF/MTP and CAX transporters, which is an important mechanism of its detoxification and its storage in seeds (Eroglu et al., 2016; Eroglu et al., 2017; He et al., 2021). CAX2 mediates vacuolar Mn^{2+} sequestration, but plays only a minor role in Ca^{2+} transport (Pittman et al., 2004). A three-amino-acid region has been identified as instrumental for Mn^{2+} specificity of this transporter (Shigaki et al., 2003). However, albeit its overexpression in tobacco caused an increased Mn^{2+} tolerance (Hirschi et al., 2000), in a *cax2* knockout mutant sensitivity to Mn^{2+} was initially reported to be unaffected (Pittman et al., 2004), but later shown to be increased (Connorton et

al., 2012). This discrepancy indicates that this transporter is not generally important for Mn^{2+} detoxification. CAX5 also transports Ca^{2+} and Mn^{2+} , but had a lower transport velocity for both elements than its close relative CAX2 and also differs in expression pattern, with only CAX5 being upregulated by elevated levels of Mn^{2+} (Edmond et al., 2009). Further work is required to examine a potential functional redundancy or co-operation of CAX2 and CAX5. The vacuolar Ca^{2+} transporter CAX4 is transcriptionally upregulated by Mn^{2+} stress and Ca^{2+} depletion, and a *cax4* knockout mutant is Mn^{2+} -sensitive (Cheng et al., 2002; Mei et al., 2009), making it likely that CAX4 is involved in the tolerance to Mn^{2+} toxicity. In this respect, the resistance of *cax1* mutants to Mn^{2+} toxicity and their altered Mn^{2+} accumulation may be the result of an induction of CAX4 expression (Cheng et al., 2003). In addition, auxin responses of roots were altered in the *cax4* mutant (Mei et al., 2009). Mechanistic explanation of this phenotype may lie in the involvement of Ca^{2+} homeostasis in auxin signaling (Dindas et al., 2018) or in the role of Mn^{2+} in auxin deconjugation.

High cytosolic Mn^{2+} has the potential to inhibit Fe(III) reduction mediated by Ferric chelate reductase 2 (FRO2), hence triggering Fe chlorosis (Eroglu et al., 2016). In Arabidopsis, this problem is circumvented by sequestration of Mn^{2+} in root vacuoles by the vacuolar transporter MTP8 (Eroglu et al., 2016). Consequently, *mtp8* mutants are prone to iron chlorosis upon Fe limitation in the presence of Mn^{2+} . Vacuolar Mn^{2+} accumulation by MTP8 also protects seeds from Mn^{2+} toxicity during imbibition (Eroglu et al., 2017). In the embryo of developing Arabidopsis seeds, Mn^{2+} is allocated specifically in the subepidermal cell layer on the abaxial side of the cotyledons and in the cortex of the hypocotyl, whereby MTP8 mediates the import into protein storage vacuoles of those cells (Chu et al., 2017; Eroglu et al., 2017) (Figure 2). The physiological importance of this vacuolar Mn^{2+} storage is reflected in poor germination of *mtp8* mutant seeds derived from Mn^{2+} -limited mother plants (Eroglu et al., 2017). In the absence of MTP8, Mn^{2+} is

allocated to the prevascular bundles by VIT1 (Figure 2), albeit the primary function of VIT1 is to move Fe^{2+} into vacuoles of developing embryos (Kim et al., 2006).

Mn^{2+} homeostasis also depends on remobilization from organelles or the apoplast into the cytosol. ZIP1, a transporter of the Zinc Regulated Transporter (ZRT) family is localized in root vacuoles and likely involved in remobilizing Mn^{2+} , but its function in cellular Mn^{2+} homeostasis is still unknown (Milner et al., 2013). Proteins of the NRAMP family, Arabidopsis NRAMP3 and -4, also remobilize vacuolar Mn^{2+} (Thomine et al., 2003; Oomen et al., 2009). Mutation of *NRAMP3* and -4 renders the plant hypersensitive to Mn^{2+} deficiency, which is associated with a decrease in chloroplastic Mn^{2+} and reduced photosynthetic activity (Lanquar et al., 2010). This indicates an important role of these vacuolar Mn^{2+} efflux transporters for Mn^{2+} loading into the chloroplasts. A mechanistic explanation of the distribution of released vacuolar Mn^{2+} remains to be established, and possibly involves vesicular trafficking, as discussed above.

ECA1, a $\text{P}_{2\text{A}}$ -type ATPase, is the only transport protein described so far that transfers Mn^{2+} into the endoplasmic reticulum (Liang et al., 1997; Johnson et al., 2009). Arabidopsis *eca1* mutants show growth inhibition by high Mn^{2+} , indicating that ECA1 is important for tolerance to toxic levels of Mn^{2+} (Wu et al., 2002). The absence of a phenotype under standard growth conditions suggests the existence of other mechanisms responsible for Mn^{2+} transport into the ER, with ECA2 and ECA4 being suitable candidates (Liang et al., 1997). Specific ER subcompartments, named ER bodies, contain two $\text{Mn}^{2+}/\text{Fe}^{2+}$ transporters, Membrane Protein of Endoplasmic Reticulum Body 1 (MEB1) and MEB2, that are distantly related to the vacuolar transporter VIT1 (Yamada et al., 2013). ER bodies have been found only in Brassicales (Matsushima et al., 2003), where they are constitutively present in roots and induced by wounding or jasmonate treatment in epidermal cells of mature leaves. It has been proposed that this organellar structure functions in metal sequestration and in the defense against herbivores by accumulating EE-type myrosinases (Yamada et al., 2011). Since Mn^{2+} may

stimulate myrosinase activity (Ohtsuru and Kawatani, 1979), the loading of Mn^{2+} into ER bodies is likely required for their function. Specific mechanisms of Mn^{2+} release from the ER in plants are still unknown.

To fulfill its function in the OEC, Mn^{2+} needs to cross the chloroplast envelope and the thylakoid membrane. Both steps are mediated by members of the BICAT family, with BICAT1/PAM71/CCHA1 supplying the thylakoid lumen and BICAT2/CMT1 operating in the inner envelope (Schneider et al., 2016; Eisenhut et al., 2018; Zhang et al., 2018). These transporters were described independently by several groups and tagged with an array of non-systematic names that may lead to confusion. Owing to its phenotype, a thylakoid-localized transporter was first described as Photosynthesis Affected Mutant 71 (PAM71), with a second member named PAM71-homolog (PAM71-HL) (Schneider et al., 2016). For its presumed transport function and localization, this protein was also named Chloroplast-localized Ca^{2+}/H^{+} Antiporter 1 (CCHA1) (Wang et al., 2016). Later, PAM-71-HL was renamed Chloroplast Manganese Transporter 1 (CMT1) based on one of its substrates and its localization (Eisenhut et al., 2018; Zhang et al., 2018). This situation was unsatisfactory because proteins of this family are neither all likely to be localized in chloroplasts, nor are they selective transporters for Ca^{2+} or Mn^{2+} . In our analysis of those proteins, we therefore renamed them Bivalent Cation Transporter 1 (BICAT1) and BICAT2, based on the substrate spectrum of all known eukaryotic homologs (Frank et al., 2019). This nomenclature has found wide acceptance in the community (Stael, 2019; Navazio et al., 2020; Ruiz et al., 2020; Schmidt et al., 2020).

BICAT1 is localized in the thylakoid, while BICAT2 resides in the inner envelope of the chloroplast (Schneider et al., 2016; Wang et al., 2016; Eisenhut et al., 2018; Zhang et al., 2018; Frank et al., 2019). The complementation of yeast mutants defective in Mn^{2+} and Ca^{2+} transport indicated the permeation of both cations by those proteins. Interestingly, two studies employing different mutants indicated that BICAT2 mediates Mn^{2+} influx into or Mn^{2+} efflux from the cytosol

(Eisenhut et al., 2018; Zhang et al., 2018). Transport of Ca^{2+} by BICAT1 and BICAT2 was confirmed by transport assays employing *E. coli* or yeast vesicles (Frank et al., 2019). In agreement with an activity in Ca^{2+} transport, Arabidopsis mutants devoid of *BICAT1* or *BICAT2* were defective in $^{45}\text{Ca}^{2+}$ uptake by illuminated isolated thylakoids and chloroplasts, respectively (Frank et al., 2019). Frank et al. (2019) proposed that BICAT2 may import cytosolic Ca^{2+} during the light phase. Imported Ca^{2+} may be bound, and released to the stroma upon darkness. Stromal Ca^{2+} may subsequently be translocated by BICAT1 into thylakoids or released into the cytosol. This is, however, complicated by the other function of those transporters, the transport of Mn^{2+} into the chloroplast and the lumen. Mutants of *BICAT2* are defective in Mn^{2+} accumulation in chloroplasts, and Mn^{2+} partitioning is altered in *bicat1* (Schneider et al., 2016; Eisenhut et al., 2018; Zhang et al., 2018). Consequently, Mn^{2+} binding to PSII complexes is reduced and the mutants are defective in PS II activity, which is most severe in *bicat2*. In *bicat1*, but not in *bicat2*, PSII activity was restored by supplementation of Mn^{2+} (Schneider et al., 2016; Eisenhut et al., 2018). Phenotypically, *bicat2* mutants display severe defects in growth, chloroplast morphology, and photosynthetic activity, while *bicat1* mutants are less affected and the *bicat1bicat2* phenotype is similar to that of *bicat2*. This highlights the dominant role of BICAT2 in chloroplast structure and functions (Schneider et al., 2016; Eisenhut et al., 2018; Zhang et al., 2018; Frank et al., 2019). Further investigations are required to unravel the transport mode and selectivity of chloroplast BICATs that determines their dual function. Their parallel interference in Ca^{2+} and Mn^{2+} homeostasis necessitates discriminative mechanisms and complicates the analysis of the role of those transporters *in planta*.

With the recent description of a chloroplast-localized Mitochondrial Calcium Uniporter (cMCU), a Ca^{2+} channel in the chloroplast inner envelope, as well as in root mitochondria, was identified (Teardo et al., 2019). Since mammalian MCU

proteins are permeable to Mn^{2+} (Kamer et al., 2018), a role of cMCU may lie in Mn^{2+} supply to or release from chloroplasts, what remains to be studied.

As mentioned before, Mn^{2+} supply to the chloroplast is also dependent on the NRAMP2 transporter in the *trans*-Golgi network (Alejandro et al., 2017). This transporter is functionally epistatic to the vacuolar Mn^{2+} exporters NRAMP3 and NRAMP4, pointing to a crucial function of vesicular compartments for intra-organellar Mn^{2+} distribution (He et al., 2021). The Arabidopsis NRAMP2 protein rescues the low- Mn^{2+} -sensitive phenotype of the $\square smf2$ yeast mutant, which is devoid of the yeast NRAMP transporter SMF2 that mediates intracellular Mn^{2+} distribution in yeast. Growth of *nramp2* mutants was strikingly sensitive to Mn^{2+} deficiency (Alejandro et al., 2017; Gao et al., 2018), and in one study, expression of NRAMP2 was induced in both shoots and roots under this stress (Alejandro et al., 2017). Defects in Mn^{2+} supply of chloroplasts and vacuoles suggest that NRAMP2 redistributes Mn^{2+} to these organelles, as discussed above (Alejandro et al., 2017). Moreover, NRAMP2 has been suggested to promote the reutilization of root- Mn^{2+} , as Mn concentrations were found to be higher in roots and lower in young leaves under Mn^{2+} starvation (Gao et al., 2018). However, since *nramp2* shoots accumulated more Mn^{2+} than those of the wild type in another study (Alejandro et al., 2017), this aspect demands further scrutiny.

The relevance of Mn^{2+} translocation through the Golgi apparatus and TGN is also supported by the severely aberrant Mn^{2+} handling in mutants of *MTP11*, that are very hypersensitive to Mn^{2+} excess and hypertolerant to Mn^{2+} limitation. MTP11 has been localized in the pre-vacuolar compartment (PVC) and the Golgi, and, based on higher Mn^{2+} levels in the mutants, suggested to promote Mn^{2+} detoxification by vesicular secretion (Delhaize et al., 2007; Peiter et al., 2007). Its capacity to transport Mn^{2+} by Mn^{2+}/H^+ antiport was shown by direct transport assays (Delhaize et al., 2007; Peiter et al., 2007). *mtp11* knockout mutants are hypersensitive and *MTP11* overexpressors hypertolerant to Mn^{2+} toxicity.

Another Mn^{2+} transporter, the P_{2A} -type ATPase ECA3, has similarly been localized in the Golgi and PVC, and *eca3* mutants are equally sensitive to Mn^{2+} toxicity (Li et al., 2008; Mills et al., 2008). ECA3 is suggested to function as Ca^{2+}/Mn^{2+} pump as shown in yeast complementation studies. Two studies localized it to the Golgi and the PVC (Li et al., 2008; Mills et al., 2008). An involvement in Ca^{2+} and Mn^{2+} homeostasis is supported by phenotypes of *eca3* mutants, which are hypersensitive to low Ca^{2+} or high Mn^{2+} supply. The protein was thus suggested to detoxify Mn^{2+} via loading it into vesicles followed by exocytosis, and to ensure Ca^{2+} -dependent processes in the Golgi (Li et al., 2008; Mills et al., 2008). As an equivalent mechanism has been suggested for MTP11 and ECA3, it ought to be analyzed if both proteins operate in the same pathway or even interact.

Considering the specific targeting of enzymes to distinct Golgi subcompartments as well as the different cation requirements of GTs (see 1.2), a concerted regulation of the concentration and ratio of Ca^{2+} and Mn^{2+} in the Golgi apparatus is likely to be crucial. The UPF0016 family, that comprises BICAT1 and BICAT2, contains proteins from many eukaryotes, bacteria and archaea, all of which harbor one or two copies of the consensus motif E- ϕ -G-D-(KR)-(ST) (ϕ can be any hydrophobic residue) and share conserved functions with members of the Cation/ Ca^{2+} exchanger (CCX) superfamily (Demaegd et al., 2014). Alike the regulation of Ca^{2+} and Mn^{2+} homeostasis in chloroplasts by BICAT1 and BICAT2, Gcr1-Dependent Translation Factor1 (GDT1) in yeast and its human homolog Transmembrane Protein165 (TMEM165) determine Ca^{2+} and Mn^{2+} homeostasis in the Golgi. Initially believed to be Ca^{2+}/H^+ antiporters that regulate Ca^{2+} and pH homeostasis (Demaegd et al., 2013), they were subsequently shown to also transport Mn^{2+} (Stribny et al., 2020). This renders them crucial for Golgi-localized Mn^{2+} -dependent processes in yeast and humans (Potelle et al., 2016; Foulquier and Legrand, 2020). In human cells, the Ca^{2+}/Mn^{2+} transporter TMEM165 is important for glycosylation, in particular the activity of Mn^{2+} -dependent β -1,4-

galactosyltransferase 1 (B4GALT1), which co-localizes with TMEM165 in the trans-Golgi, and some $\text{Ca}^{2+}/\text{Mn}^{2+}$ -ATPases are also potentially involved in Ca^{2+} and Mn^{2+} supply of Golgi-localized GTs (Foulquier et al., 2012; Foulquier and Legrand, 2020). In yeast, the $\text{Ca}^{2+}/\text{Mn}^{2+}$ -ATPase Pmr1 and the $\text{Ca}^{2+}/\text{Mn}^{2+}$ transporter GDT1 are both required for protein glycosylation (Dürr et al., 1998; Colinet et al., 2016).

Unlike in animals and yeast, Golgi-localized Mn^{2+} transport proteins identified in plants so far have been associated with Mn^{2+} detoxification, whereas our understanding of the Mn^{2+} supply of the complex Golgi-localized glycosylation processes is quite rudimentary. A role of ECA3 in glycosylation remains to be elucidated, and further transport proteins to support this function remain to be identified, whereby homologs of GDT1/TMEM165 represent promising candidates.

1.3.2 Mn^{2+} transport in *Hordeum vulgare*

To date, only few transporters implicated in Mn^{2+} transport have been identified in barley (*Hordeum vulgare* L.). Intriguingly, unlike IRT1 orthologs in *A. thaliana* and rice, HvIRT1 plays a vital role in Mn^{2+} uptake and translocation, but not in Fe uptake (Long et al., 2018). HvIRT1 is localized in the plasma membrane (Pedas et al., 2008). It is prominently expressed in the epidermis of roots under normal conditions, and its expression can be induced in cortex and pericycle cells by Mn^{2+} deficiency (Long et al., 2018). In addition, HvNramp5 is another plasma membrane-localized Mn^{2+} transporter in *H. vulgare* roots, which is expressed more strongly in the epidermis of the root tips than in the basal part of roots (Wu et al., 2016). Although both HvIRT1 and HvNramp5 are involved in Mn^{2+} uptake by roots, HvIRT1 is dominant for Mn^{2+} uptake under Mn^{2+} -limited conditions, while HvNramp5 contributes to constitutive Mn^{2+} uptake (Wu et al., 2016).

A member of the CAX family, HvCAX2 is ubiquitously expressed in leaves and roots, where it likely transports Ca^{2+} and Mn^{2+} into vacuoles (Edmond et al.,

2009). Pedas et al. (2014) identified HvMTP8.1 and HvMTP8.2, two CDF family proteins, which localized in the Golgi apparatus when transiently expressed in onion epidermal cells. Both proteins complemented the Mn^{2+} sensitivity of the *pmr1* Δ yeast mutant strain, indicating that they are able to transport Mn^{2+} . The expression pattern of *HvMTP8.1* and *HvMTP8.2* in *H. vulgare* roots was conversely regulated under different Mn^{2+} conditions. Expression of *HvMTP8.1* was induced by Mn^{2+} toxicity and repressed by Mn^{2+} deficiency, whereas this pattern was reversed in *HvMTP8.2*, indicating diverse functions in Golgi Mn^{2+} homeostasis regulation in *H. vulgare* roots (Pedas et al., 2014).

1.4 Generation of crop mutants by CRISPR-mediated mutagenesis

Genome editing methods have been improved drastically during the last few years. Compared to editing systems mediated by Zinc Finger Nucleases (ZFNs) and Transcription Activator-Like Effectors (TALENs) which require DNA-protein interactions for specific editing, systems mediated by Clustered Regularly Interspaced Short Palindromic Repeats (CRISPR)-associated Cas proteins are more accurate, efficient, and cost-effective (Chen et al., 2019). Moreover, they only require a single guide RNA (sgRNA) for precise genome editing (Chen et al., 2019). Cas proteins have different targets due to their distinct properties. Cas9 and Cas12a (also named Cpf1) nucleases trigger double strand DNA (dsDNA) breaks, while Cas13 triggers RNA breaks (Knott and Doudna, 2018). SpCas9 from *Streptococcus pyogenes* is the most commonly harnessed Cas nuclease which recognizes an 'NGG' protospacer adjacent motif (PAM) sequence for its binding and function (Knott and Doudna, 2018). Recently, scientists have eliminated the limitation of PAM requirement of SpCas9 to expand its usage (Walton et al., 2020). In the CRISPR/Cas9 system, sgRNA targets Cas9 to specific genome loci, and RuvC and HNH nuclease domains of Cas9 catalyze a double strand break (DSB) at around 3-4 bp upstream of the 5' end of the PAM. Afterwards, the DSB will be

repaired via homology-directed repair (HDR) pathways when a homologous donor DNA is available, or via non-homologous end joining (NHEJ) pathways, which will consequently generate nucleotide substitutions, short insertions, or deletions (indels) (Gaillochet et al., 2021). CRISPR/Cas9 systems have been developed as valuable tools for exploring gene functions and improving crops traits (Zhang et al., 2021).

1.5 Objectives of this work

In plants, not only *N*- and *O*-glycosylation of proteins demands Mn^{2+} , but also a plethora of glycosyltransferases involved in the synthesis of cell wall matrix polysaccharides (He et al., 2021). It has been known for long that those reactions are spatially organized to form an efficient assembly line. Specific Mn^{2+} transporters are thus expected to be required for specific glycosylation steps, as it is the case in animals. In plants, it is largely unknown which processes present a bottleneck under Mn^{2+} limitation. Moreover, the specific role of Golgi-localized Mn^{2+} transporters and the functional interaction of their activity with other Mn^{2+} -requiring processes are poorly understood despite some recent progress. This work is aimed to elucidate the localization, function, and roles of an Arabidopsis candidate protein, BICAT3, that is potentially involved in Mn^{2+} supply of the Golgi, in a reverse genetic approach. Furthermore, by employing molecular, cell biological and physiological methods, the conservation and distinction of functions of BICAT3 should be assessed between Arabidopsis and barley using T-DNA knockout mutants and loss-of-function mutants generated by CRISPR/Cas9, respectively.

2 Materials and methods

2.1 Plasmids and constructs

For cloning the *BICAT3* genomic sequence and native promoter (gDNA), leaves of soil-grown *A. thaliana* Col-0 were ground in liquid nitrogen. DNA samples were extracted by using DNeasy Plant Mini Kit (QIAGEN, Hilden, Germany). The DNA fragments were amplified in a thermocycler (Mastercycler nexus GSX1, Eppendorf, Hamburg, Germany) by using gene-specific primers containing specific restriction sites (see Appendix) and Phusion DNA polymerase (F-503S, Thermo Fisher Scientific, Waltham, USA).

For cloning the coding sequence (CDS) of *BICAT3* and *HvBICAT3*, RNAs were isolated from leaves of soil-grown *A. thaliana* Col-0 plants and *H. vulgare* (cv. Golden Promise) plants using the Spectrum Plant Total RNA Kit (STRN250-1KT, Sigma Aldrich, St. Louis, USA) with an on-column DNase treatment with DNase I (30 U) for 15 min at room temperature (Omega bio-tek, Norcross, USA). cDNA was generated by using one μg of RNA and Protoscript II Reverse Transcriptase (NEB, Ipswich, USA). The coding region of *BICAT3* and *HvBICAT3* was amplified in a thermocycler by using gene-specific primers containing specific restriction sites (see Appendix). Phusion DNA polymerase (F-503S, Thermo Fisher Scientific) and ExTaq DNA polymerase (RR001, Takara, Shiga, Japan) were used for cloning the coding region of *BICAT3* and *HvBICAT3*, respectively.

The amplified DNA or cDNA fragments and the respective vectors were digested as described below. Digested vectors were dephosphorylated with Shrimp Alkaline Phosphatase (2 U; NEB) for 15 min at 37°C if a single restriction enzyme was used. Otherwise ligation was directed performed after digestion and purification, with T4 ligase (200 U) at 16°C overnight. The amounts of vector and insert were calculated as follows: $[(100 \text{ ng vector} \times \text{bp insert})/\text{bp vector}] \times 3 = \text{insert [ng]}$. All purification steps were performed with the Wizard SV Gel and PCR Clean-Up System (Promega, Madison, USA). Electro-competent *E. coli* cells

(TOP10; Thermo Fisher Scientific) were transformed with ligation reactions by electric shock of 2500V in an electroporator (2510, Eppendorf). After incubation in SOC media at 37°C for 1 h and 180 rpm in a shaking incubator (Certomat IS, Sartorius, Göttingen, Germany), transformed bacteria were plated on selective LB media. Minipreparation of single colonies was performed with the Pure Yield Plasmid Miniprep System (Promega). The individual constructs will be described in the respective sections. All restriction enzymes were obtained from NEB and are listed in the Appendix.

For uracil-specific excision reagent (USER)-based cloning (Nour-Eldin et al., 2006), DNA or cDNA fragments of *BICAT3* and *HvBICAT3* were amplified with Phusion U Polymerase (F-555S, Thermo Fisher Scientific). USER-compatible vectors were digested in a total volume of 200 μ L [1.4 U PacI restriction endonuclease (R0547, NEB), 15 μ g plasmid, 1 x CutSmart Buffer (B7204, NEB)], incubated for 6 h at 37°C in an incubator (Mettler, Schwabach, Germany). 0.4 units of PacI restriction endonuclease and 1 unit of nicking endonuclease Nt.BbvCI (R0632, NEB) were added, and digest reactions were further incubated overnight at 37°C. The digested vector was separated on an agarose gel and purified as described before. The USER reaction was performed with 0.5 μ L USER enzyme (M5505S, NEB), 3.9 μ L of purified DNA amplicons, 1 μ L PacI/Nt.BbvCI-digested vector, and 0.6 μ L 10 x taq buffer. The USER reaction was incubated for 30 min at 37°C and 1 h at 25°C to ligate DNA. Chemical-competent *E. coli* cells (TOP10; Thermo Fisher Scientific) were transformed with ligation reactions by heat shock at 42°C for 1.5 min incubation with ligations on ice for 20 min. Transformed bacteria were plated on selective LB media after incubation in 600 μ L SOC media at 37°C for 1 h and 180 rpm in a shaking incubator (Certomat IS).

Primers, constructs, and media are listed in the Appendix.

2.2 Plant material

2.2.1 *A. thaliana* lines

2.2.1.1 Screening of *A. thaliana bicat3* mutants

A. thaliana T-DNA insertion mutant lines were obtained from Nottingham Arabidopsis Stock Centre (NASC). *bicat3-1* (GABI_027F07) and *bicat3-2* (SALK_97998) mutants in Columbia-0 (Col-0) background were part of the GABI collection and the SALK collection, respectively (Ülker et al., 2008). Homozygous plants were identified by using gene-specific primers as listed in the Appendix. The insertions were identified with GABI_LB primer for the lines of the GABI collection and SALK_LB primer for the lines of the SALK collection (s. Appendix).

For identification of gene knockout and knockdown, RNA extraction and cDNA synthesis was performed as described above (s. 2.1). For reverse transcriptase PCR, gene-specific primers were used. To test the quality of the cDNA, *Beta-6 Tubulin (TUB6; At5g12250)* was amplified as an internal control. For quantification of gene expression in a knockdown mutant, quantitative reverse transcription PCR (qRT-PCR) was performed in a realplex⁴ Mastercycler system (Eppendorf) by using the POWER SYBR Green PCR mastermix (Applied Biosystems, Foster City, USA). *Actin2 (ACT2; At3g18780)* was used as a control.

2.2.1.2 *A. thaliana* complementation lines: *bicat3-1::gBICAT3*

For complementation of the *bicat3-1* mutant line, genomic DNA of *BICAT3* including the 5'UTR and promoter region (2017 bp upstream of the ATG) and the 3'UTR (493 bp downstream of the TAG) was amplified from Col-0 genomic DNA and cloned into pGreenII0229 (Hellens et al., 2000) using SmaI-containing primers. The vector and the amplicons were digested with SmaI, purified, dephosphorylated and ligated as described in 2.1. *Agrobacterium tumefaciens* (GV3101) bacteria were transformed with the construct by electric shock of 2500V

in an electroporator (2510, Eppendorf). After incubation in SOC media at 28°C for 2 h and 180 rpm in a shaking incubator (Certomat IS), transformed bacteria were plated on selective YEB media containing kanamycin (50 µg mL⁻¹), rifampicin and gentamycin (25 µg mL⁻¹). A single positive colony was plated on a fresh selective YEB plate containing the same antibiotics and incubated for three days at 28°C. Homozygous *bicat3-1* plants were stably transformed with the *A. tumefaciens* transformant by the floral-dip method (Clough and Bent, 1998). Seedlings were selected on ½ MS plates (s. Appendix) containing kanamycin (50 µg mL⁻¹).

2.2.1.3 *A. thaliana* promoter-GUS lines: *PrBICAT3-GUS*

For promoter-GUS studies, the promoter region of *BICAT3* (1811 bp upstream of the start codon) was amplified from Col-0 genomic DNA using *Sma*I-containing primers (s. Appendix) and cloned into pBI101, upstream of the *uidA* gene (Jefferson et al., 1987). *A. tumefaciens* (GV3101) bacteria were transformed with the construct as described above (s. 2.2.1.2). *A. thaliana* Col-0 plants were stably transformed with the *A. tumefaciens* transformant by the floral-dip method. Seedlings were selected on ½ MS plates (s. Appendix) containing kanamycin (50 µg mL⁻¹).

2.2.1.4 *A. thaliana* complementation lines with Venus tag: *bicat3-1::PrBICAT3-BICAT3-Venus*

To assemble the pCAMBIA2300u-*PrBICAT3-BICAT3-Venus-tNos* vector, the region 1811 bp upstream of the *BICAT3* start codon, *BICAT3-Venus*, and a *Nos* terminator were amplified from Col-0 genomic DNA, pART7-*BICAT3-Venus*, and pILTA381, respectively, using USER cloning-compatible primers (Nour-Eldin et al., 2006) (s. Appendix). The pART7-*BICAT3-Venus* vector was generated by inserting the *BICAT3* CDS into pART7-*Venus* using *Xma*I-containing primers (s. Appendix). *A. tumefaciens* (GV3101) bacteria were transformed with the construct

as described above (s. 2.2.1.2). *bicat3-1* plants were stably transformed with the *A. tumefaciens* transformant by the floral-dip method. Seedlings were selected on ½ MS plates (s. Appendix) containing kanamycin (50 µg mL⁻¹). This line was used in pollen tube and immunogold localization experiments.

2.2.2 *H. vulgare bicat3* CRISPR mutants

2.2.2.1 Identification of HvBICAT3

To retrieve *H. vulgare* BICAT proteins, the amino acid sequences of *A. thaliana* BICATs (BICAT1_At1G64150, BICAT2_At4G13590, BICAT3_At5g36290, BICAT4_At1g25520 and BICAT5_At1g68650) were used as queries for blastp searches at the IPK Galaxy Blast Suite [<https://galaxy-web.ipk-gatersleben.de/>; Afgan et al. (2018)]. The amino acid sequences of *A. thaliana* and *H. vulgare* BICAT proteins were aligned by ClustalW (Larkin et al., 2007). A phylogenetic tree was generated by MEGA7 using the Neighbor-joining method (Kumar et al., 1994). The evolutionary distances were computed using the Equal input method and all ambiguous positions were removed by pairwise method. The gene sequence of *HvBICAT3* was confirmed in the Golden Promise cultivar by PCR with ExTaq DNA polymerase (RR001, Takara) using '*HvBICAT3_F1*' and '*HvBICAT3_R2*' primers (s. Appendix) and subsequent Sanger sequencing.

2.2.2.2 Design of sgRNAs

The CRISPR-GE website [<http://skl.scau.edu.cn/home/>; Xie et al. (2017)] was used to design sgRNAs for generation of *H. vulgare hvbicat3* mutants. 5'-NGG-3' was selected as PAM sequence. *H. vulgare* (ASM32608v1) was selected as target genome. A sequence of 840 bp downstream of the ATG of the *HvBICAT3* genomic sequence was used to design sgRNAs. sgRNAs without 'bad site warning' and pairing, with low potential off-target risk, residing in CDS and without

Bsal sites [GGTCTC], Bpil sites [GAAGAC], and polyT stretches [≥ 5 Ts; transcriptional termination] were selected, and the off-target risks were further checked by BLAST analysis of sgRNAs sequences at the IPK Galaxy Blast Suite. Three sgRNAs localized in the third, fourth, and fifth exons of *HvBICAT3* were selected based on analyses of the predicted off-target risk and on-target efficiency of sgRNAs. The target site in the fifth exon containing an EcoRV restriction site adjacent to the protospacer adjacent motif (PAM) was selected to facilitate mutant screening.

2.2.2.3 Vector construction

To generate pMGE632:sgRNA and pMGE634:sgRNA constructs for mutating *HvBICAT3*, cloning overhangs 'agca' and 'aac' were added to forward and reverse primers of sgRNAs, respectively. The following steps were done as previously described in Kumar et al. (2018) with minor modifications. Forward and reverse primers of sgRNAs were hybridized separately in pair by heating the mixture (5 μ L of 10 μ M stock of each primer and 40 μ L ddH₂O) to 98°C for 5 min and cooling down to room temperature. Hybridized primers were diluted 100 times and were cloned into sgRNA shuttle vectors by pipetting 1 μ L shuttle vector, 1 μ L hybridized oligo nucleotide, 1 μ L 10 x ligation buffer, 1 μ L BSA (1 mg mL⁻¹), 0.5 μ L Bpil, 0.5 μ L T4 DNA ligase, and 5 μ L ddH₂O into a PCR reaction tube and running 20 cycles of 37°C for 2 min and 16°C for 5 min, with a terminating cycle of 50°C for 10 min and 80°C for 10 min. TOP10 chemical-competent cells were transformed with cut/ligation reactions (pMGE625 M1: sgRNA1, pMGE626 M2: sgRNA2, pMGE628 M3: sgRNA3, and pMGE629 M4E: sgRNA3). Transformants were directly inoculated in Ampicillin (50 μ g mL⁻¹)-selective LB liquid media. Liquid cultures were used for polyclonal plasmid preparation. sgRNA transcriptional units (TUs) were assembled into genome-editing vectors (recipient vectors: pMGE632 and pMGE634) by pipetting 1 μ L of each shuttle vector, 3 μ L recipient vector, 2 μ L

10 x ligation buffer, 1 μ L Bsal, 1 μ L T4 DNA ligase, and 9 μ L ddH₂O into a PCR reaction tube and running 35 cycles of 37°C for 2 min and 16°C for 5 min, with a terminating cycle of 50°C for 10 min and 80°C for 10 min. TOP10 chemical-competent cells were transformed with cut/ligation reactions by heat shock. Transformants were plated on LB media containing Spectinomycin (25 μ g mL⁻¹). Colonies were checked by colony-PCR with 'JS1558+M13_F' primers. Plasmid from a single positive colony was mini-prepped. MGE632:sgRNAs constructs were sequenced with 'JS1558', 'M13_F', and 'HvBICAT3_sgRNA1_F' primers; pMGE634: sgRNAs constructs were sequenced with 'JS1132', 'M13_F', 'HvBICAT3_sgRNA1_F', and 'HvBICAT3_sgRNA2_F' primers (s. Appendix). Schematic diagrams of pMGE632:sgRNAs and pMGE634:sgRNAs constructs are presented in the Results section (Fig. 32B).

2.2.2.4 *H. vulgare* transformation

For *H. vulgare* transformation, *A. tumefaciens* AGL1 was transformed with pMGE632:sgRNAs or pMGE634:sgRNAs and plated on a selective YEB plate (100 μ g mL⁻¹ Rifampicin, 25 μ g mL⁻¹ Carbenicillin and 25 μ g mL⁻¹ Spectinomycin). Positive *Agrobacterium* transformants were identified by PCR using 'JS1558+M13_F' primers (s. Appendix). *Agrobacteria* were cultured 24 h at 28°C in 10 mL YEB media containing antibiotics as mentioned above. pMGE632:sgRNAs and pMGE634:sgRNAs constructs were independently transformed into spring *H. vulgare* cultivar 'Golden Promise'. In each transformation, 100 immature seeds from the middle of the *H. vulgare* spikes were harvested and sterilized with 70% ethanol followed by 20 min in bleach (3% NaOCl + 0.02% Tween 20). Subsequently, seeds were washed 2-3 times with sterile ddH₂O after neutralizing with sterile ddH₂O (pH 3 with HCl). Scutelli were isolated under a dissecting microscope in a sterile laminar flow hood. Afterwards, every 25 scutelli were placed on a Petri dish containing callus induction media (C-) (s. Appendix) and

immersed in 200 μL of *Agrobacteria* culture for 40 min. Ten inoculated scutelli were transferred to a fresh plate containing the same media and cultured 2 days in the dark at 24°C. Thereafter, inoculated scutelli were transferred to fresh plates containing the same media with antibiotics (C+) (s. Appendix) and cultured 2 weeks in the dark at 24°C to eliminate agrobacteria and induce callus formation. Fast-growing calli were transferred and cultured 2 weeks in the dark at 24°C on fresh callus induction plates (C+). This selection step was repeated once more. Then, calli were transferred to shoot induction media (T) (s. Appendix) and cultured 2 weeks under long-day conditions with low light in a Percival (Perry, USA) CU-36 tissue culture cabinet (16/8h light, 150 $\mu\text{mol m}^{-2} \text{s}^{-1}$, 22/18°C, 65% RH). Calli with developing leaves were transferred to root induction media (R) (s. Appendix) and cultured for 3-4 weeks under the same conditions. Small plantlets were transferred to jars containing callus induction medium (without dicamba, growth regulators, and antibiotics) and further cultured under the same conditions until roots reached the bottom of the glass tube. Regenerated plantlets were carefully transferred to 1L soil boxes and cultured in the greenhouse (16/8h light, 600 $\mu\text{E m}^{-2} \text{s}^{-1}$, 20/14 °C, 65% RH) until maturity.

2.2.2.5 Screening of *H. vulgare* mutants

DNA of T0 mutants was isolated from a single leaf disc, and T-DNA insertions were confirmed by PCR with 'zCas9-F' and 'zCas9-R' primers. The 'HvBICAT3_F2' and 'HvBICAT3_CRISPR_R2' primers (s. Appendix) were used to amplify and screen for mutations in *HvBICAT3*. The 'HvBICAT3_CRISPR_R2' primer was used to sequence those amplicons. The mutations were characterized by cloning the amplicons into pGEMTeasy. Six independent pGEMTeasy constructs from each transformation were sequenced by using an M13 primer. Biallelic and chimeric plants were cultured further for seed generation. T1 mutant screening was performed as described for T0, except that only three independent

pGEMTeasy constructs from each transformation were sequenced by using a M13 primer. Bi-allelic, heterozygous and WT progenies were validated by digesting PCR amplicons with EcoRV for 3 h at 37°C, and separating on a 1.5% agarose gel. Digested amplicons presenting completely digested fragments (485 and 153 bp) were considered as wild type (WT) and amplicons showing bands in different sizes as mutants. In addition, *Cas9* was amplified by using the ‘zCas9-F’ and ‘zCas9-R’ primers to screen for transgene-free T1 CRISPR mutants. These mutants were cultured for propagation. To confirm the homozygous mutations, ten progenies of each homozygous T1 mutant were checked by PCR and sequencing. The whole workflow is presented schematically in Figure 3.

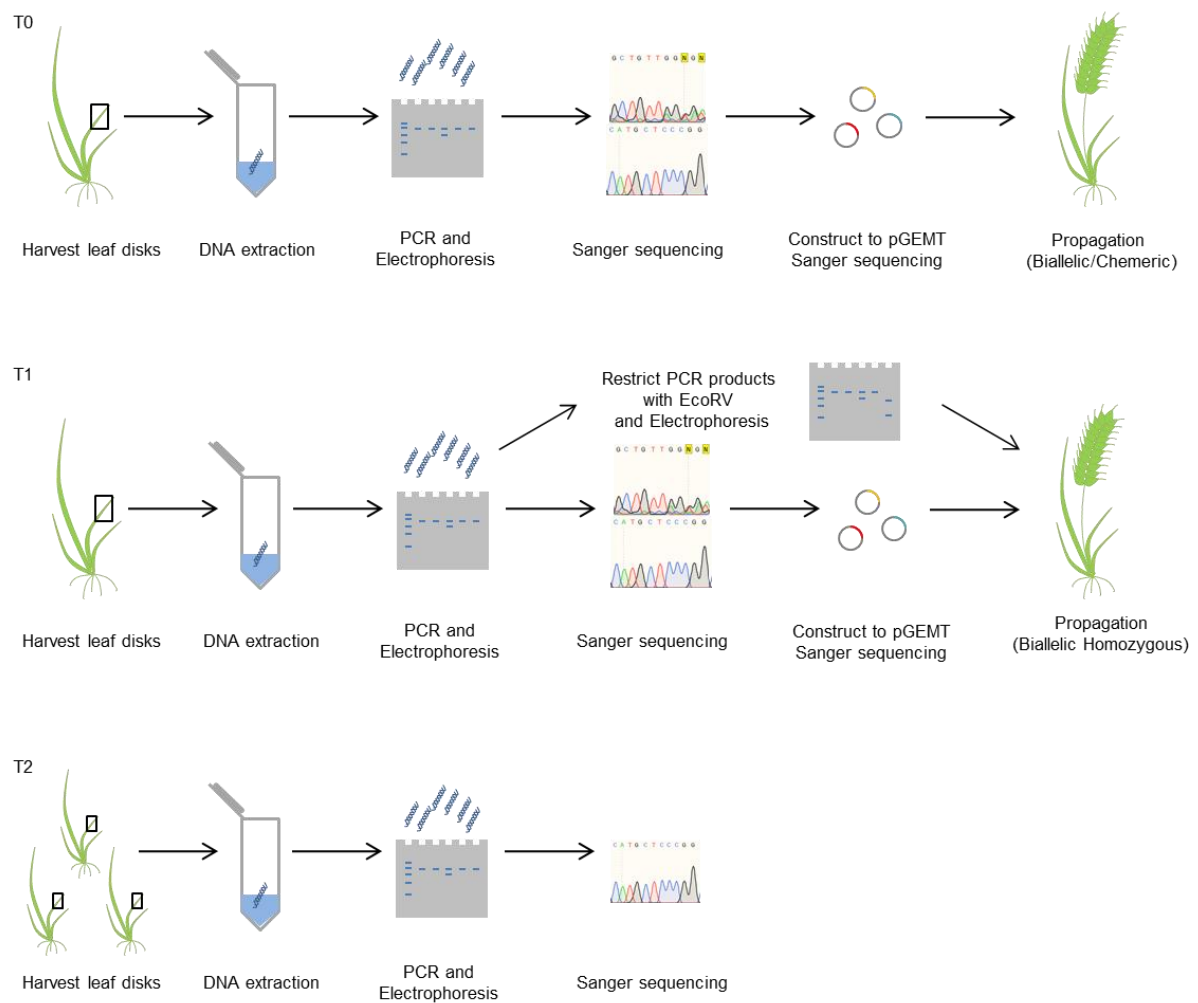


Figure 3. Workflow of *Hvbicat3* mutant screening from T0 generation to the homozygous T2 generation

2.3 Plant cultivation

2.3.1 Cultivation of *A. thaliana* on agar plates

To cultivate seedlings on half-strength Murashige and Skoog ($\frac{1}{2}$ MS) agar plates (s. Appendix), seeds of WT and transgenic *A. thaliana* were sterilized in 70% (v/v) ethanol for 1 min, 30% (v/v) bleach and 0.02 % Triton X-100 for 5 min, and rinsed five times with sterile water. Seeds were stratified for 3 d at 4°C in darkness.

For testing the growth of plants under Mn^{2+} deficiency on plates, stratified seeds were sown on self-made $\frac{1}{2}$ MS agar plates (50 mL per 11.5*11.5 cm square plate) with or without Mn^{2+} , containing 8 g L⁻¹ agar (No. 2266.1, Carl Roth, Karlsruhe, Germany) and 2.5 g L⁻¹ sucrose. Plants were cultured for two weeks in a growth cabinet (AR75, Percival Scientific) set to 21°C day and 19°C night temperature and 16 h light period with a light intensity of 150 $\mu\text{mol m}^{-2} \text{s}^{-1}$ photons, and a relative humidity of 65 %. For root length measurements, plates were scanned every other day from the 4th day until the 14th day after sowing. Primary root length of seedlings was measured by the NeuronJ plugin of Fiji (Schindelin et al., 2012).

For testing the growth of plants under Ca^{2+} and Mn^{2+} toxicity on plates, stratified seeds were pre-cultured seven days on $\frac{1}{2}$ MS (M0231, Duchefa Biochemie), containing 8 g L⁻¹ agar (Phyto Agar P1003, Duchefa Biochemie) and 2.5 g L⁻¹ sucrose, adjusted to pH 5.8 with KOH. Plants were cultured in a growth cabinet as above. Seven-day old seedlings were transferred to new $\frac{1}{2}$ MS media with or without additional 50 mM $CaCl_2$ or 1 mM $MnSO_4$, and cultured for another eight days. Plates were scanned every other day after transferring the seedlings for root length measurement, and primary root lengths of seedlings were measured as above.

2.3.2 Cultivation of *A. thaliana* in hydroponic nutrient solution

For cultivation of *A. thaliana* in hydroponics, sterile and stratified seeds were sown on ½ MS (M0231, Duchefa Biochemie) containing 8 g L⁻¹ agar (Phyto Agar P1003, Duchefa Biochemie) and 2.5 g L⁻¹ sucrose, adjusted to pH 5.8 with KOH. After 12 days of growth, seedlings were transferred to seedling holders created by removing the tip of a 1.5 mL centrifuge tube and a cylindrical polyethylene foam piece (BKF A. Fleuren GmbH, Friesoythe, Germany). A nutrient solution modified after Peiter et al. (2007) was used as hydroculture basal medium (s. Appendix). After growing for 10 days in 1 L containers with basal medium (40 seedlings per container), roots and seedling holders were washed three times with ddH₂O. Seedlings were transferred to 4 L containers containing control or treatment media (15 seedlings per container), and cultivated further for two weeks. In the case of recovery experiments, plants were cultivated in basal media for one more week after two weeks of Mn²⁺ deficiency treatment. Plants on plates and in hydroponics were cultured in a growth cabinet (ATC26, Conviron, Winnipeg, Canada) set to 21°C day and 19°C night temperatures and 10 h light period with a light intensity of 150 μmol m⁻² s⁻¹ photons. The nutrient solution was aerated and changed twice a week.

2.3.3 Cultivation of *H. vulgare* in hydroponic nutrient solution

Seeds were germinated on wet tissue paper in square dishes at room temperature in darkness for 4 days. Plants were transferred to hydroponic culture and supplied with ½-strength nutrient solution for the first three days and further cultured for four days in complete nutrient solution (s. Appendix). Plants were transferred to fresh complete or Mn²⁺-deficient (0 μM) nutrient solution and cultured 11 days more. Photosynthetic activities of the second youngest leaves were measured at 11 days after onset of treatment (DAF) with an IMAGING-PAM MAXI Version (IMAGING-PAM *M-Series*, Walz, Effeltrich, Germany) as described

in the following section (2.11). Plants were cultured in a growth cabinet (ATC26, Conviron) set to 20°C day and 18°C night temperatures and 16 h light period with a light intensity of 300 $\mu\text{mol photons m}^{-2} \text{ s}^{-1}$, RH 60%. The nutrient solution was refreshed twice a week.

2.3.4 Cultivation of *A. thaliana* and *H. vulgare* on soil

Plants were cultivated in standardized ED73 soil (Einheitserde Werkverband e.V., Sinntal-Altengronau, Germany) mixed with 1/3 vermiculite (w/w) (Gärtnereibedarf Kammlott GmbH, Erfurt, Germany) and 10 g L⁻¹ (w/w) BioMükk® (BioFa AG, Münsingen, Germany). Plants were grown in air-conditioned greenhouse cabinets with supplemental light (high-pressure sodium lamps; 16 h photoperiod) set to 20/18°C for *A. thaliana* and to 20/14°C for *H. vulgare*.

2.4 Histochemical GUS staining

Promoter-GUS lines were generated as described in 2.2.1.3. Plants were cultivated either on sterile ½ MS agar plates or on soil. Plant materials were transferred to GUS staining solution containing 100 mM sodium phosphate buffer (pH 7.0), 10 mM EDTA, 3 mM K₄[Fe(CN)₆], 0.5 mM K₃[Fe(CN)₆], 0.1% Triton X-100 (v/v), and 2 mM 5-Bromo-4-chloro-3-indolyl-beta-D-glucuronic acid (X-Gluc, X-Gluc Direct, Malaga, Spain) in DMSO. Samples were vacuum-infiltrated with staining solution two times for 5 min and subsequently stained for 3 h at 37°C. Chlorophyll was removed by 80% ethanol (v/v). Of 15 independent promoter-GUS lines, 13 showed the same staining pattern. Two homozygous single-insertion lines were chosen for in-depth analysis. The stained tissues were documented with an AxioCam HRc digital camera (Carl Zeiss, Jena, Germany) mounted on a SteREO Discovery V.20 stereo microscope (Carl Zeiss).

For GUS staining of pollen and pollen tubes, pollen was harvested and cultured *in vitro* for 3 h as described below (2.8.3) and subsequently stained with GUS staining solution for 3 h at 37°C.

2.5 Yeast complementation assays

The pRS416-BICAT3 plasmid was prepared by inserting the *BICAT3* full-length sequence in pRS416 using BamHI and XhoI. The pRS416-HvBICAT3 plasmid was prepared by inserting the *HvBICAT3* full-length sequence in pRS416 using BamHI and EcoRI.

Yeast wild type (BY4741, Y00000, Euroscarf, Oberursel, Germany), and mutants BY4741-*pmr1*Δ and BY4741-*gdt1*Δ*pmr1*Δ were transformed with pRS416, pRS416-BICAT3, or pRS416-HvBICAT3 as described (Frank et al., 2019). Transformants were selected on synthetic complete (SC) media lacking uracil. Yeast drop assays of BICAT3 were performed on AP-Ura (pH 5.5) (s. Appendix) media to assess Mn²⁺ toxicity and Ca²⁺ toxicity, as described previously (Peiter et al., 2007; Frank et al., 2019). Yeast drop assays of HvBICAT3 were performed on SC-Ura (pH 5.5) (s. Appendix) and AP-Ura (pH 5.5) media to assess Mn²⁺ toxicity and Ca²⁺ toxicity, respectively.

2.6 Subcellular localization of BICAT3 and HvBICAT3

2.6.1 Subcellular localization of BICAT3

The full-length *BICAT3* coding sequence was used to construct pART7-BICAT3-Venus and pART7-BICAT3-mCherry. Organellar markers for co-localization experiments were generated by Nelson et al. (2007). Protoplasts of the *A. thaliana* Col-0 wild type and an ST-GFP *trans*-Golgi marker line (Hawes and Satiat-Jeunemaitre, 2005) were prepared and transiently transformed with the constructs as described previously (Peiter et al., 2007). 24 h after transformation,

GFP and mCherry fluorescence was observed by confocal laser microscopy using a LSM 880META with a planapochromatic lens (63x/1.4 Oil) (Carl Zeiss). Images shown in Figure 4 were taken in Lambda mode (410-651 nm) with a resolution of 1024x1024 in plane scan mode for single lines with four repetitions. As excitation light source, an argon laser with an excitation wavelength of 488 nm and a main dichroic beam splitter 488/561 nm was used. GFP and mCherry signals were separated by linear unmixing with previously generated spectra. Spectra were obtained from protoplasts transiently transformed with the pART7 vector containing the respective fluorophore. Pictures shown in Figure 5 were acquired by the same microscope in channel mode with a resolution of 512x512 pixels. Excitation light source was a 488 nm argon laser (GFP) and a 561 nm diode laser (mCherry). GFP and mCherry fluorescence were detected at emission wavelengths of 499-553 nm and 588-633 nm, respectively.

2.6.2 Ultrastructural localization of BICAT3-Venus

For ultrastructural localization of BICAT3-Venus, leaf segments were transferred into aluminum planchettes and high-pressure frozen with an HPM 10 instrument (BAL-TEC, Liechtenstein). Subsequently the material was cryo-substituted in 0.25% glutaraldehyde (Sigma Aldrich) and 0.1% uranyl acetate (Chemapol, Czech Republic) in acetone for 2 days at -80°C using cryosubstitution equipment (FSU, BAL-TEC). This was followed by embedding in HM20 (Polysciences Europe, Eppelheim, Germany) at -20°C. For immunolabelling of ultrathin sections, a polyclonal anti-Venus antibody (St. John's Laboratory, London, UK; diluted 1:300) was employed, which was detected by a rabbit anti goat secondary antibody conjugated with 10 nm gold (G5527, Sigma Aldrich; diluted 1:100). Sections were post-stained with uranyl acetate and lead citrate with an EMSTAIN instrument (Leica, Wetzlar, Germany) and observed with a Libra 120 transmission electron microscope (Carl Zeiss) operated at 120 kV. Images were

taken by using a dual-speed on-axis SSCCD camera (BM-2k-120; TRS, Moorenweis, Germany).

2.6.3 Subcellular localization of HvBICAT3

The full-length *HvBICAT3* CDS was amplified by PCR with 'USER *HvBICAT3_F*' and 'USER *HvBICAT3_R*nost' primers and cloned into pART7-Venus by USER cloning as described in 2.1. Protoplasts of *H. vulgare* cv. Golden Promise leaves were prepared and transformed with the constructs as described previously for *A. thaliana* (Peiter et al., 2007) with minor modifications. The enzyme solution to digest the leaf cell walls contained 13 g L⁻¹ Cellulysin RS (Duchefa Biochemie) and 8 g L⁻¹ Macerase R-10 (Duchefa Biochemie).

24 h after transformation, Venus and mCherry fluorescence was observed by confocal laser scanning microscopy using a LSM 880META with a Plan apochromatic lens (63x/1.4 Oil) (Carl Zeiss). Pictures were taken in channel mode with a resolution of 1144x1208 pixels. Excitation light source was a 488 nm argon laser (Venus) and a 561 nm diode laser (mCherry). Venus and mCherry fluorescence were detected at an emission wavelength of 493-574 nm and 578-638 nm, respectively.

2.7 Reciprocal crossing of Arabidopsis

Four-to-five-week-old plants grown in the greenhouse were used for reciprocal crossing. Anthers were removed from the late unopened flowers, avoiding damage of the female reproductive part. Emasculated plants were cultivated overnight in the greenhouse for further maturation of the stigma. The stigmatic surfaces of emasculated flowers were pollinated with the desired pollen. Pollinated plants were further cultivated in the greenhouse until siliques were matured. Siliques were documented by an SLR camera (Pentax K-10D).

2.8 Arabidopsis pollen tube growth assays

2.8.1 Observation of BICAT3-Venus in pollen and pollen tubes

For observation of BICAT3-Venus in pollen and pollen tubes, pollen of *bicat3-1* stably expressing *BICAT3-Venus* were harvested and cultured *in vitro* for 3 h as described below (2.8.3) and subsequently observed by fluorescence microscopy using an AxioCam MRm Rev. 3 camera mounted on an Axio Observer.Z1 (Carl Zeiss) microscope equipped with a Filter Set FS46HE (ex. BP500/25, FT 515, em. BP535/30) (Carl Zeiss) and a Plan Apochromatic lens (40x/1.3 oil) (Carl Zeiss).

2.8.2 *In vivo* and *semi in vivo* pollen tube growth assays

For the *in vivo* pollen assay, 4-5-week-old plants grown on soil in the greenhouse were used. Anthers were removed from late unopened flowers, avoiding damage of the female reproduction part. Emasculated plants were cultivated further overnight for maturation of the stigmata. The stigmatic surfaces of emasculated flowers were pollinated with desired pollen. Pistils were harvested 48 h after pollination and decolorized in 1:3 acetic acid/ethanol until they were transparent. Pistils were further incubated in 8 M NaOH overnight and subsequently stained with Aniline blue solution [0.1 g L⁻¹ Aniline blue (CI 42780, Carl Roth), 150 mM K₂HPO₄] for 5 h in dark after washing three times with 150 mM K₂HPO₄. Pictures were documented with an LSM 880META with a Plan-apochromatic lens (20x/0.8) (Carl Zeiss) in tile scanning mode. Samples were excited with a 405 nm argon laser, and fluorescence was detected by with an emission wavelength of 498 nm.

The *semi in vivo* pollen tube growth assay was performed as described by Dickinson et al. (2018). A part of the pollinated pistils, above the junction to the ovary, was excised 1 h after hand-pollination and subsequently placed on a gel pad in a humid chamber. Pictures were documented with a SteREO Discovery

V.20 stereomicroscope (Carl Zeiss). Pollen tubes lengths were measured by NeuronJ plugin of Fiji software (Schindelin et al., 2012).

2.8.3 Ruthenium red staining of pollen tubes

For detection of pectin in pollen tubes, pollen were cultured *in vitro* for 6 h as described in Ischebeck et al. (2008). Pollen tubes were subsequently stained by 0.1 g L⁻¹ Ruthenium Red (Sigma Aldrich) for 10 min. Pictures were documented with an AxioCam MRc camera mounted on an Axioskop microscope (Carl Zeiss).

2.8.4 Immunostaining of pollen tubes

Freshly opened flowers from 4-5-week-old *A. thaliana* plants grown on soil in greenhouse were harvested and incubated in a humid box at 22°C for 30 min. Pollen was collected into filter-sterilized liquid pollen germination media (5 mM KCl, 1 mM MgSO₄, 5 mM CaCl₂, 0.1 g L⁻¹ H₃BO₃, 100 g L⁻¹ sucrose, pH 7.5) by washing flowers up and down in the medium. Pollen grains were incubated at 30°C for 40 min before further incubation at 22°C for 3 h. For immunostaining, pollen tubes were fixed in freshly prepared 30 g L⁻¹ paraformaldehyde and 100 g L⁻¹ sucrose in PIPES buffer [50 mM PIPES (pH 6.9), 2 mM EGTA, 2 mM MgSO₄] at room temperature for 2 h. Pollen tubes were subsequently washed twice in PIPES buffer and three times in PBS (pH 7.2). For removing the residual paraformaldehyde, pollen tubes were incubated in 0.1 M NH₄Cl PBS buffer for 5 min and once in PBS (pH 7.2). For detection of low-esterified homogalacturonan, pollen tubes were further incubated overnight in the 1:10-diluted primary antibody solution (JIM5, Plant Probes, University of Leeds, UK) in PBS (pH 7.2) buffer with 50 g L⁻¹ BSA at 4°C after blocking in PBS (pH 7.2) buffer with 50 g L⁻¹ BSA for 0.5 h. Pollen tubes were washed four times in PBS (pH 7.2) buffer with 1 g L⁻¹ BSA, followed by 90 min incubation with 1:500 diluted secondary antibody solution [goat anti-rat IgG cross-adsorbed, Alexa Fluor 488 (A-11006, Thermo Fisher Scientific)].

Pollen tubes were subsequently washed three times with PBS (pH 7.2) buffer and transferred to microscopy slides. Fluorescence was observed by confocal laser scanning microscopy using a LSM 880META with a Plan-apochromatic lens (40x/0.95) (Carl Zeiss). Pictures of pollen tubes were taken in channel mode with the same gain and a resolution of 1024x1024. Samples were excited with an 488 nm argon laser and fluorescence was detected with an emission wavelength of 546 nm.

2.9 Seed size measurements

The measurement of seed size was carried out with transmitted light scanning as described previously with slight modifications (Herridge et al., 2011). Seeds were stochastically spread on a petri dish and photographed at a 1200 dpi resolution with a flatbed scanner (Epson perfection v750 pro). Seed size was quantified by the 'particle analysis' function of the Fiji software with a setting of 'arbitrary' to 162 greyscale (Schindelin et al., 2012).

2.10 Seed germination assays

Sterilized and stratified seeds were sown on 10 layers of sterilized wet Blue Roll paper moistened with ddH₂O and cultured in darkness at 22°C. Germinated seeds with emerged radicles were counted every 8 h for 3 d.

2.11 Photosynthesis measurements

For measuring photosynthetic parameters of *A. thaliana*, plants were dark-adapted for 30 min. Images were captured, and maximal photochemical efficiency of PSII (Fv/Fm) and photochemical efficiency of PSII (Y (II)) changes with increasing light intensities were determined by PAM fluorescence imaging (IMAGING-PAM *M-Series*, Walz, Effeltrich, Germany). Saturating flashes (902

$\mu\text{mol m}^{-2} \text{ s}^{-1}$) were used to measure the maximum quantum yield of PSII. The photochemical efficiency of PSII was measured under a series of flashes with increasing intensity (1, 7, 21, 42, 69, 101, 140, 185, 237, 361, 512, 681, 902 $\mu\text{mol m}^{-2} \text{ s}^{-1}$). All fluorescence measurements were performed on intact plants at room temperature.

For measuring photosynthetic parameters of *H. vulgare*, plants were dark-adapted for 30 min. Images were captured, and maximal photochemical efficiency of PSII (Fv/Fm) and photochemical efficiency of PSII (Y (II)) changes with increasing light intensities were also determined by PAM fluorescence imaging. Saturating flashes (1083 $\mu\text{mol} \cdot \text{m}^{-2} \cdot \text{s}^{-1}$) were used to measure the maximum quantum yield of PSII. The photochemical efficiency of PSII of plants was measured under a series of flashes (1, 7, 25, 53, 88, 129, 175, 231, 293, 439, 619, 820, 1083 $\mu\text{mol} \cdot \text{m}^{-2} \cdot \text{s}^{-1}$). All fluorescence measurements were performed on excised 2nd youngest leaves at room temperature.

2.12 Analysis of metal concentrations in plants

For determination of metal concentrations of hydroponically cultured *A. thaliana* (s. 2.3.2), shoots were harvested and dried for 3 d at 65°C in a drying cabinet (Linn High Therm, Eschenfelden, Germany). Roots were sequentially washed in ice-cold washing buffer I (1 mM MES-KOH, pH 5.8) for 10 min, in washing buffer II (10 mM EDTA and 1 mM MES-KOH, pH 5.8) for 10 min, and rinsed in ddH₂O before they were also dried in the same cabinet.

For determination of metal concentrations of *H. vulgare*, the 2nd youngest leaf of hydroponically grown plants (s. 2.2.3) was harvested and dried; roots were sequentially washed as described above and dried.

Dried materials were weighed into PFA vessels (CEM, Matthews, USA) and digested in 65% HNO₃ (v/v) for 20 min at 190°C in a MARS 5 Xpress (CEM) microwave oven with the temperature ramped to 190°C in 15 min. Elements were

analyzed by microwave plasma - atomic emission spectrometry (MP-AES; 4210, Agilent Technologies, Palo Alto, CA, USA).

2.13 Analysis of metal concentrations in chloroplasts

For the determination of metal concentrations in chloroplasts, plants were cultivated and treated in a hydroponic system as described above. After removing midrib veins, leaf samples (around 2 g fresh weight) were homogenized in 45 mL homogenization buffer [0.4 M sorbitol, 20 mM Tricine-NaOH (pH 8.4), 10 mM EDTA, 1 g L⁻¹ BSA, 5 mM NaHCO₃, and 1 mM MgCl₂] by using a blender (Waring, Stamford, CT, USA) at low speed for 5 s. The mixture was filtered through 75 µm mesh (pre-wetted with homogenization buffer) into 50 mL tubes. Subsequently, the extracts were squeezed through two layers of pre-wetted 10 µm nylon mesh and concentrated at 1500 g for 5 min. The pellet was resuspended in at least 2 mL washing buffer [80 mM sorbitol, 4 mM Tricine-NaOH (pH 8.4), 0.5 mM EDTA, and 1 mM MgCl₂] and then loaded gently onto a discontinuous 40/85% (w/v) Percoll gradient in washing buffer followed by centrifugation (4000 g, 15 min, 4°C) in a swinging bucket rotor. Around 1 mL intact chloroplasts were recovered from the 40/85% (w/v) Percoll interphase. Three volumes of washing buffer (around 3 mL) were added, gently mixed, and centrifuged (10 min at 200 g followed by 1 min at 1700 g; 4°C). Chloroplasts were washed three times with 2 mL cold washing buffer. The integrity of the chloroplasts was verified by microscopy, and the number of chloroplasts was estimated by counting with a Neubauer chamber. 500 µL chloroplast suspension together with 100 µL 65% HNO₃ were pipetted into a 15 mL Falcon tube and digested overnight at 70°C. The ion concentrations were determined by ICP-MS using a Cetac ASX-560 (Teledyne, Cetac Technologies, Omaha, NE, USA) autosampler, a MicroFlow PFA-200 nebulizer, and an iCAP-RQ ICP-MS instrument (Thermo Fisher Scientific).

2.14 Grafting

For reciprocal grafting of *bicat3-1* and Col-0 wild type, stratified seeds were sown onto ½ MS plates, which were placed vertically in a growth cabinet set to 21°C day and 19°C night temperatures and 10 h light period with a light intensity of 150 $\mu\text{mol photons m}^{-2} \text{s}^{-1}$ and grown for 5-6 days. Grafting was performed by using the 'Two Segment Shoot-Root Graft' method according to Melnyk (2017) with some modifications. Sterile water was added to an empty Petri dish containing two pieces of sterile Whatman® 3MM Chr cellulose chromatography paper (WHA3030917, Whatman, Maidstone, UK) and one sterile Amersham Hybond-N⁺ membrane (RPN303B, Cytiva, Marlborough, MA, USA) strip on the top. One cotyledon of the seedling was cut off and discarded, and a transverse butt-end cut through the hypocotyl close to the shoot was made. Scions and rootstocks were grafted on the Hybond membrane strip and the redundant water in the petri dish was removed by sterile Whatman paper strips. Three days after grafting, 1 mL sterile water was added to plates. One week after grafting, successfully grafted plants which were well attached and without adventitious roots were transferred to ½ MS plates containing 0.8% agar (Phyto Agar P1003, Duchefa Biochemie) and 0.25% sucrose. After recovering for one week, well-developed grafted plants were transferred to hydroponic solution. Grafted plants grew in complete hydroponic basal media for 12 d and were cultured for two more weeks after transfer to treatment media. In order to create Mn²⁺-deficient conditions, 0.05 $\mu\text{M MnSO}_4$ instead of 3.5 $\mu\text{M MnSO}_4$ was added to basal medium. Plants were cultured as described above for hydroponic cultures.

2.15 Leaf sectioning and cell size measurements

To visualize leaf flatness, leaves were embedded in 30 g L⁻¹ low-melting agarose (Biozym Scientific, Hessisch Oldendorf, Germany). 40 μm sections were

prepared with a vibrating microtome (HyraX V 50, Carl Zeiss) and documented with an AxioCam MRc camera mounted on an Axioskop microscope (Carl Zeiss).

To quantify leaf cell size and shape, leaf segments were fixed with 3% (w/v) glutaraldehyde (Sigma Aldrich) in 0.1 M sodium cacodylate buffer (SCB; pH 7.2) for 3 h at room temperature. After fixation, the samples were rinsed in SCB and postfixed with 1% (w/v) osmium tetroxide (Carl Roth) in SCB for 1 h at room temperature. Subsequently, the leaf segments were rinsed with water, dehydrated in a graded ethanol series (10%, 30%, 50%, 70% (containing 1% (w/v) uranyl acetate), 70%, 90% and 2×100% for 30 min each), infiltrated with epoxy resin according to Spurr (1969), and polymerized at 70°C for 18 h. Semi-thin sections (1 µm) were transferred to glass slides and stained with 0.1% toluidine blue. Images were taken by using an Axioskop 20 light microscope (Carl Zeiss) equipped with an AxioCam MRc camera (Carl Zeiss). Morphometric measurements were performed with the iTEM software (Olympus SIS, Münster, Germany).

2.16 Callose detection

Plants were cultivated as described in 2.3.2. Callose depositions in leaves were analysed by aniline blue staining according to Rissel et al. (2017) with slight modifications. Leaves were fixed and de-stained in 1:3 acetic acid/ethanol. Fixed leaves were washed in 150 mM K_2HPO_4 for 30 min and subsequently incubated in aniline blue solution [0.1 g L⁻¹ aniline blue (CI 42780, Carl Roth), 150 mM K_2HPO_4] in the dark for 3 h. Stained leaves were embedded in 50% glycerol. Callose depositions were documented using an AxioCam MRm Rev. 3 camera mounted on an Axio Observer.Z1 (Carl Zeiss) microscope. Samples were excited with a HXP 120 lamp (Carl Zeiss) by using a FS49 filter set (ex. 365, FT395, em. 445/50) (Carl Zeiss).

For the ultrastructural localization of callose, the material was prepared as described above (s. 2.15). Ultrathin sections (70 nm) were made with an Ultracut

R ultramicrotome (Leica). Sections were transferred to Formvar-coated nickel grids. Immunogold labeling of callose was performed using a monoclonal β -1,3-glucan antibody (#400-2, Biosupplies; diluted 1:500) in combination with a goat anti-mouse 10 nm gold conjugated secondary antibody (#G7777, Sigma Aldrich; diluted 1:100). Sections were post-stained with uranyl acetate and lead citrate and observed with a Libra 120 transmission electron microscope (Carl Zeiss) as described in 2.6.2.

2.17 Glycoprotein assays

Plants were cultivated as described in 2.3.2. Glycoprotein pattern determinations were based on Veit et al. (2015) with some modifications. Liquid-nitrogen-ground plant material (100-150 mg) was mixed with 4 μ L PBS-T [1 PBS tablet (P4417, Sigma Aldrich), 200 mL ddH₂O, 200 μ L Tween 20 (9127, Carl Roth)], 100 μ M PMSF, and 1 μ M Leupeptin per mg powder and incubated on ice for 15 min, with vortexing every 3 min. Samples were centrifuged two times at 9600 *g* and 4°C for 15 min. The supernatant was transferred to new tubes after each centrifugation. 200 μ L of the supernatant were mixed with 200 μ L 2x Laemmli buffer and incubated at 95°C for 5 min. Samples were briefly spun and 45 μ L supernatant per sample were loaded on two 12.5% SDS gels (1.5 mm) and run at 150 V for approximately 1.5 h. After running, gels were stained with Coomassie Brilliant Blue or blotted to nitrocellulose membrane (10600125, Amersham Protran, Cytiva). For Western blot, proteins were transferred to a nitrocellulose membrane for 1 h at 100V using a tank blot system. After transfer, the membrane was blocked in blocking solution (3% BSA in PBST) overnight at 4°C. The membrane was transferred into ConA (Concanavalin A-peroxidase, L6397, Sigma Aldrich) solution (2 mg L⁻¹ ConA in PBS-T, 1 mM MnCl₂, 1 mM CaCl₂, 1 mM MgCl₂) and incubated for 3 h. Membranes were rinsed twice with PBS-T, then washed four times for 5 min with PBS-T and once with PBS. 10 mL ECL solution A (250 mg L⁻¹ Luminol

dissolved in 10 mL DMSO, 0.1 M Tris-HCl, pH 8.6), 1 mL ECL solution B (1.1 g L⁻¹ *para*-coumaric acid in DMSO), and 5 µL H₂O₂ [30% (w/v)] were mixed in a plastic box on ice. The membrane was transferred into the ECL solution with protein side facing down and incubated while agitating manually for around 1 min in the dark. Luminescence of the membrane was recorded immediately with a chemiluminescence imager (Fusion Solo S, Vilber, Eberhardzell, Germany).

2.18 Monosaccharide and sugar linkage determination

For analysis of monosaccharides and sugar linkages, plants were cultivated as described in 2.3.2. For alcohol-insoluble residue (AIR) preparation, 18 to 25 mg of lyophilized shoot materials from each genotype were ground using a steel ball for a total of 5 min at 30 Hz in a ball mill (MM400, Retsch, Haan, Germany). AIR was obtained by sequentially washing the ground material once with 1 mL of 70% ethanol, once with 1 mL of chloroform:methanol (1:1 v/v), and once with 1 mL of acetone. Following the addition of ethanol, the steel balls were removed with a magnet. After each washing step, the AIR was pelleted by centrifugation (20 000 g for 5 min), and the supernatant was carefully discarded using a plastic Pasteur pipette. After the final wash, the pellet was resuspended in 300 µL of acetone and dried in a fume hood overnight. The AIR material (2.5-3 mg) was de-starched by α-amylase (A3403-500KU, Sigma Aldrich) and pullulanase (E2412-50ML, Sigma Aldrich) in 0.1 M phosphate buffer (pH 7.0). The samples were incubated at 80°C in a thermomixer at 300 rpm for 30 min. After cooling down, the samples were incubated horizontally at 225 rpm for 24 h in a 37°C incubator. The pelleted de-starched AIR samples were dried after washing twice with water and once with acetone. For monosaccharide quantification, 0.2 to 0.5 mg of the AIR material was analyzed via high-performance anion-exchange chromatography coupled with pulsed electrochemical detection (HPAEC-PAD) as previously described (Voiniciuc and Günl, 2016) on a 940 Professional IC Vario ONE/ChS/PP/LPG instrument

(Metrohm, Herisau, Switzerland) equipped with Metrosep Carb 2-250/4.0 guard and analytical columns.

For glycosidic linkages analysis, 1 mg of the AIR material was analyzed by gas chromatography–mass spectrometry following derivatization of partially methylated alditol acetates as described (Ciucanu and Kerek, 1984) with modifications (Ciucanu, 2006). Carbohydrates were separated using a GC-MS system consisting of a 6890N gas chromatograph (Agilent, Santa Clara, CA, USA) and a 5975 quadrupole mass spectrometer (Agilent) equipped with an SP-2380 capillary column (Supelco, Sigma Aldrich). Carbohydrate peaks were annotated based on their retention time and ion spectra relative to standards.

3 Results I - The Golgi-localized Bivalent Cation Transporter3 determines manganese allocation and glycosylation of matrix polysaccharides

3.1 BICAT3 localizes to the Golgi apparatus and is ubiquitously expressed

The genome of *A. thaliana* contains five members of the functionally conserved UPF0016 family, Bivalent Cation Transporter (BICAT) 1 to 5 (Demaegd et al., 2014). Previous phylogenetic analyses revealed that BICAT3 is the closest *A. thaliana* ortholog to human TMEM165 and yeast GDT1 (Hoecker et al., 2017). Both proteins are $\text{Ca}^{2+}/\text{Mn}^{2+}$ transporters localized in the Golgi and critical for Mn^{2+} supply for protein glycosylation (Foulquier et al., 2012; Colinet et al., 2016; Potelle et al., 2016; Dulary et al., 2018; Thines et al., 2019). To investigate the subcellular localization of BICAT3, we co-expressed *BICAT3* with organelle markers fused with different fluorescent proteins in *A. thaliana* mesophyll protoplasts. BICAT3 co-localized with sialyltransferase (ST) and partially with mannosidase I (Man I), a *trans*-Golgi and *cis*-Golgi marker, respectively (Figure 4A), but not with mitochondria and peroxisomes (Figure 5). Moreover, by employing immunogold staining and electron microscopy, we found that BICAT3-Venus was localized mainly in the *medial* and *trans* cisternae of the Golgi apparatus of *bicat3-1* leaf cells stably transformed with BICAT3-Venus under control of the native *BICAT3* promoter (Figure 4B).

To reveal the expression pattern of *BICAT3* in different tissues, its promoter activity was visualized by using the β -glucuronidase (GUS) reporter. Strong *GUS* expression was detected in embryo, roots, leaves, stems, and flowers. The *BICAT3* promoter is thus active in all plant parts throughout different growth stages (Figure 4C). The expression of *BICAT3* was not affected by Ca^{2+} or Mn^{2+} deficiency or toxicity (Figure 6).

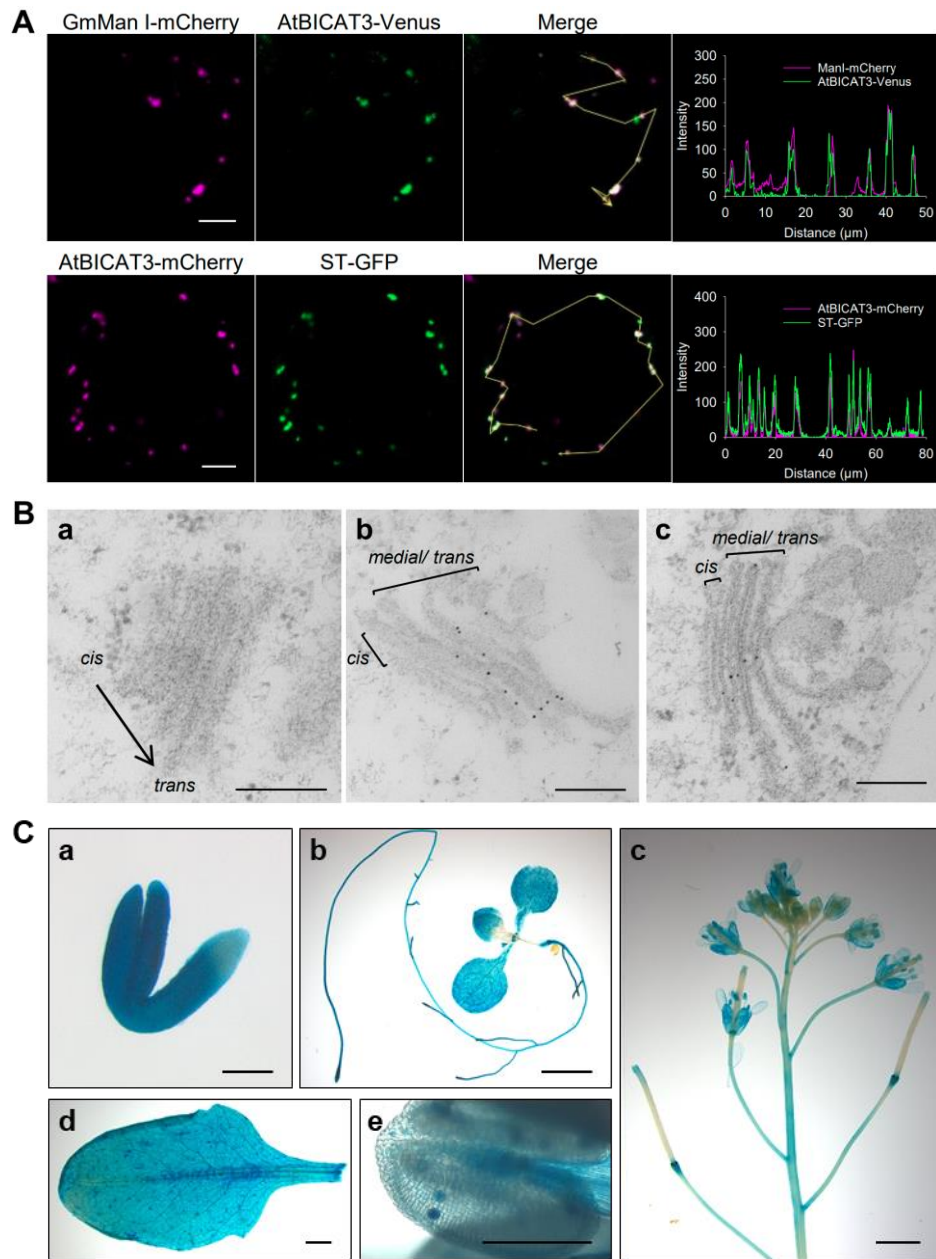


Figure 4. Golgi-localized BICAT3 has a ubiquitous expression in *A. thaliana*.

(A) Subcellular localization of BICAT3 in *A. thaliana* mesophyll protoplasts. BICAT3 fusions were co-expressed with a *cis*-Golgi marker (mannosidase I, ManI) and a *trans*-Golgi marker (sialyl transferase, ST) as indicated. Scale bars represent 5 μm.

(B) Ultrastructural localization of BICAT3-Venus. **(a)** Wild-type Golgi apparatus as a negative control. **(b)** and **(c)** BICAT3-Venus was localized mostly in the *media/trans*-Golgi apparatus of *bicat3-1* leaf cells stably producing BICAT3-Venus under control of the BICAT3 native promoter. Scale bars represent 200 nm. Experiment was conducted in collaboration with Gerd Hause.

(C) Expression of BICAT3 in different growth stages as detected by GUS staining of a *ProBICAT3-GUS* line. **(a)** Germinated seed. **(b)** 10-day-old seedling. **(c)** Inflorescence and siliques. **(d)** Mature rosette leaf. **(e)** Anther. Scale bars represent 200 μm (**a** and **e**) or 2 mm (**b**, **c**, and **d**).

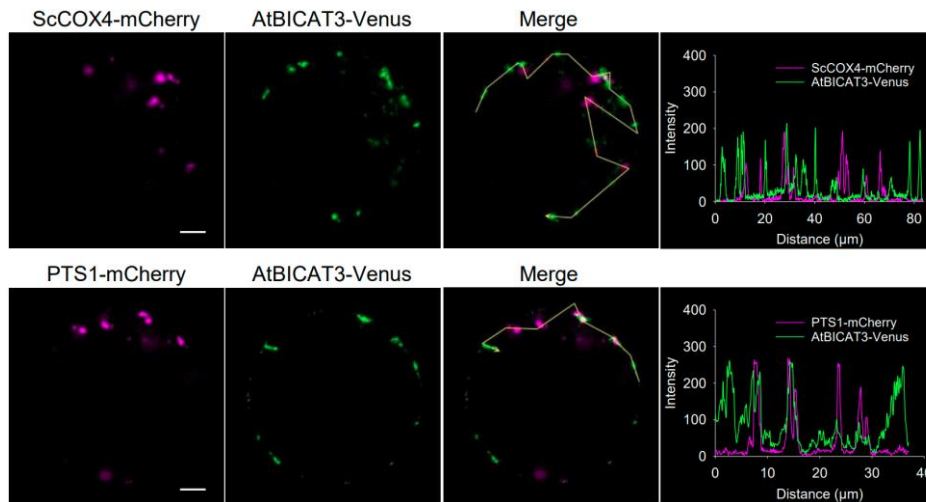


Figure 5. BICAT3 does not co-localize with mitochondria and peroxisomes.

BICAT3-Venus was co-expressed with a mitochondria marker (ScCOX4) and a peroxisome marker (PTS1) in *A. thaliana* mesophyll protoplasts. Scale bars represent 5 μm .

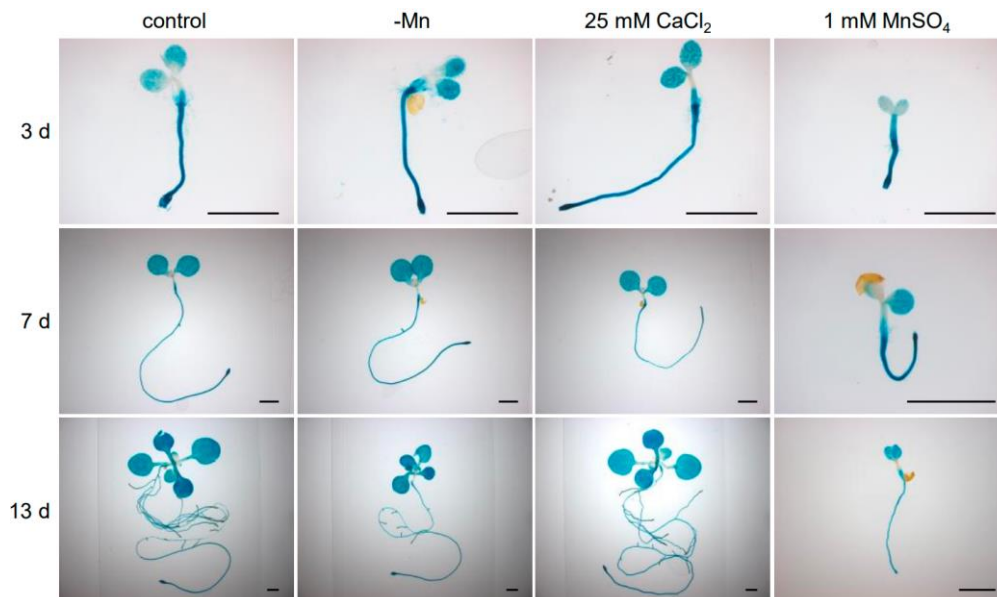


Figure 6. GUS staining of ProBICAT3-GUS seedlings grown under different Mn^{2+} and Ca^{2+} supply.

Scale bars represent 2 mm.

3.2 BICAT3 acts as Ca^{2+} and Mn^{2+} transporter in yeast

BICAT3 orthologs in yeast and humans mediate evolutionarily conserved Ca^{2+} and Mn^{2+} transport to feed compartments of the Golgi apparatus for essential

physiological processes, such as glycosylation (Colinet et al., 2016; Potelle et al., 2016; Thines et al., 2018; Stribny et al., 2020). To test if Golgi-localized BICAT3 has similar functions in cation allocation, *BICAT3* was heterologously expressed in a *pmr1Δ gdt1Δ* mutant, which displays a defect in Ca^{2+} transport into the Golgi due to the lack of the Ca^{2+} pump PMR1 and of GDT1, as well as in a *pmr1Δ* single mutant. The *pmr1Δ gdt1Δ* mutant showed strong growth retardation, while *pmr1Δ* was only slightly affected by Ca^{2+} toxicity (Figure 7A) as previously reported by Demaegd et al. (2013). The Ca^{2+} sensitivity of *pmr1Δ gdt1Δ* was complemented by the expression of *BICAT3*. The growth of *pmr1Δ gdt1Δ BICAT3* was comparable to the *pmr1Δ* single mutant under 600 mM CaCl_2 , implying a similar ability of BICAT3 and GDT1 to transport Ca^{2+} in yeast. In addition to transport Ca^{2+} , PMR1 translocates excess Mn^{2+} into the Golgi for detoxification. Heterologous expression of *BICAT3* partially complemented the Mn^{2+} sensitivity of *pmr1Δ* (Figure 7B).

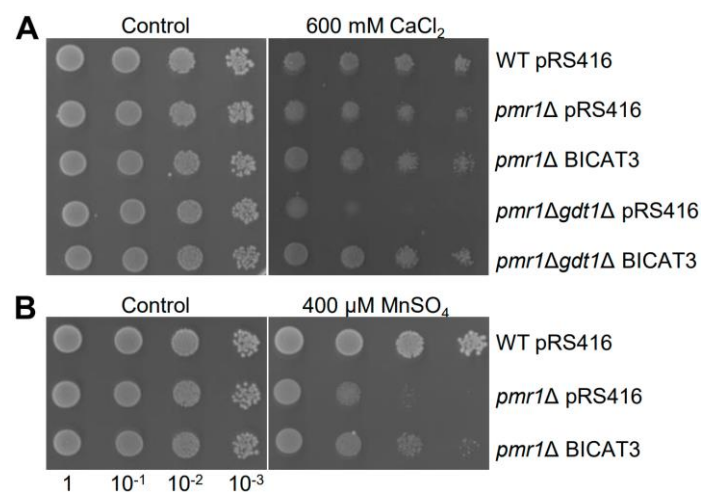


Figure 7. *BICAT3* complements Ca^{2+} - and Mn^{2+} -sensitive yeast strains.

(A) Growth of wild type, *pmr1Δ*, and *pmr1Δgdt1Δ* with and without *BICAT3* under Ca^{2+} -toxic conditions. Liquid cultures of the strains were serially diluted and dropped onto AP media.

(B) Growth of *pmr1Δ* with and without *BICAT3* under Mn^{2+} -toxic conditions. Liquid cultures of the strains were serially diluted and dropped onto AP media.

The experiment was repeated at least twice with similar results.

In contrast, BICAT3 did not complement the Zn-, Co-, Cu- and Fe-dependent growth defects in *zrc1Δ*, *cot1Δ*, *cup2Δ* and *ccc1Δ* yeast mutants, respectively (Figure 8). In conclusion, the results indicate that BICAT3 acts as a Ca^{2+} and Mn^{2+} transporter in yeast.

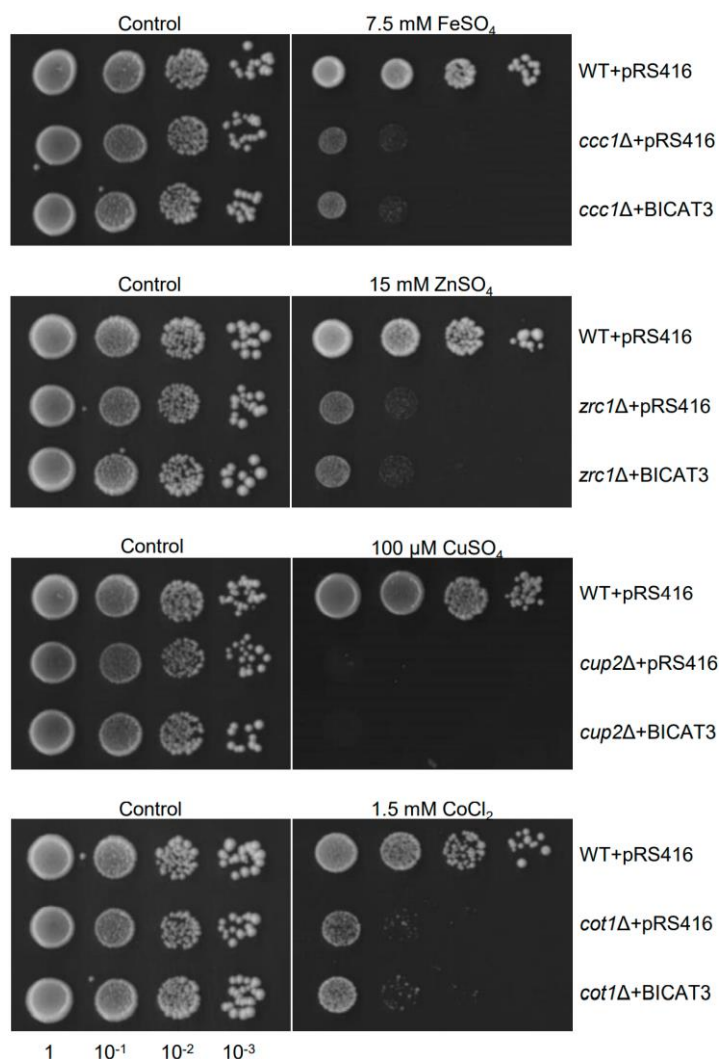


Figure 8. BICAT3 does not complement Fe-sensitive (*ccc1Δ*), Zn-sensitive (*zrc1Δ*), Cu-sensitive (*cup2Δ*) and Co-sensitive (*cot1Δ*) yeast strains.

Liquid cultures of strains were serially diluted and dropped onto SC-Ura media as indicated in the figures. The experiment was repeated at least twice with similar results.

3.3 Growth of *bicat3* mutants is differentially affected by Mn²⁺ and Ca²⁺ supply

To characterize the functions of BICAT3 in *A. thaliana*, two T-DNA insertional mutants were obtained. *bicat3-1* harbors a T-DNA in the 6th intron, and *bicat3-2* carries a T-DNA insertion in the 3'UTR region (Figure 9A).

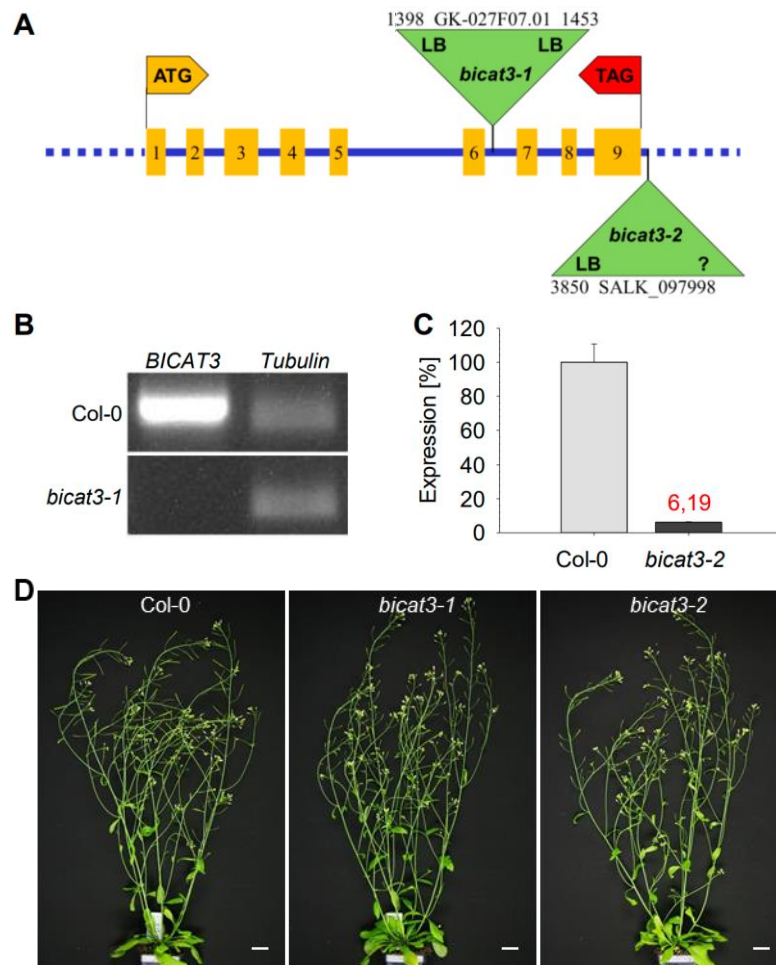


Figure 9. Genotypic characterization of *bicat3* mutants.

(A) A model of the genomic region and the T-DNA insertions in *BICAT3*. Coding regions are presented by boxes; introns are shown by a line; triangles indicate the sites of T-DNA insertions. The numbers indicate the first nucleotide after and the last nucleotide before the insertion, counting from the start codon. LB indicates the left border of the T-DNA, as determined by sequencing.

(B) Semi-quantitative RT-PCR of *BICAT3* in Col-0 and *bicat3-1* mutant. *Tubulin* was used as a housekeeping gene to ensure a similar amount of cDNA templates.

(C) Quantitative RT-PCR of *BICAT3* in Col-0 and *bicat3-2* mutant.

(D) Growth phenotypes of 6-week-old Col-0, *bicat3-1*, and *bicat3-2* grown on soil. Scale bars represent 2 cm.

While *bicat3-1* is a knock-out mutant, *bicat3-2* shows 6% of *BICAT3* transcript level compared to the wild type (Figure 9B-C). Both mutants show no obvious vegetative growth differences compared to the wild type at mature stage under non-stressed conditions (Figure 5D).

To assess the function of *BICAT3* in Ca^{2+} and Mn^{2+} homeostasis of *A. thaliana*, we first cultured *bicat3-1* and wild type seedlings on plates with different Mn^{2+} and Ca^{2+} supply. Intriguingly, young seedlings of *bicat3-1* showed a stronger growth than the wild type under Mn^{2+} - and Ca^{2+} -sufficient control conditions (Figures 10 to 12). In contrast, *bicat3-1* was more sensitive to Mn^{2+} deficiency (0 mM; Figure 10) and Ca^{2+} toxicity (50 mM; Figure 11), but more tolerant to Mn^{2+} toxicity (1 mM; Figure 12) compared to the wild type.

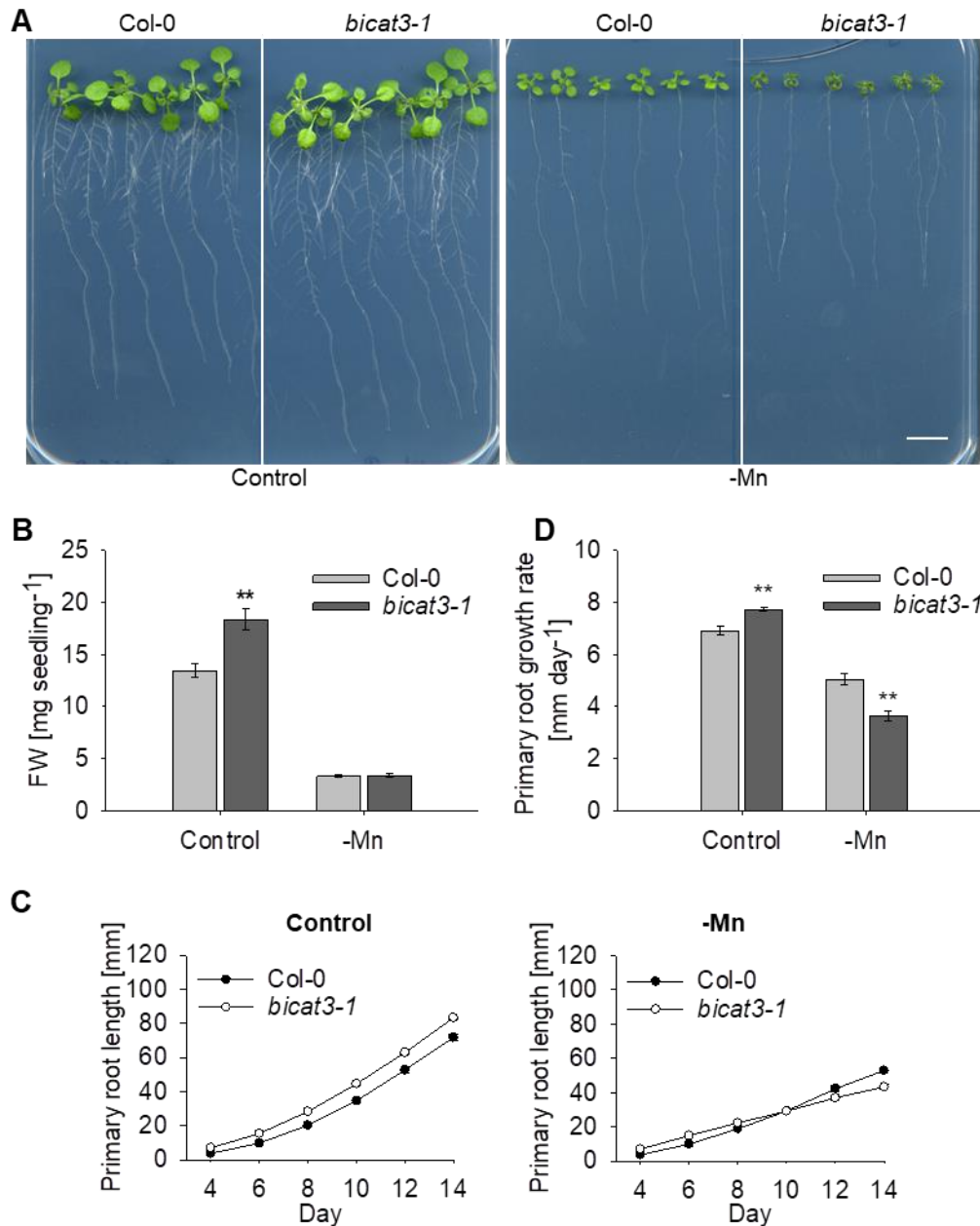


Figure 10. *bicat3-1* shows retarded growth compared to the wild type under Mn²⁺ deficiency (0 μM MnSO₄).

(A) Growth phenotypes of 2-week-old Col-0 and *bicat3-1* on control and Mn²⁺-deficient plates. Scale bar represents 1 cm.

(B) Fresh weight (FW) of Col-0 and *bicat3-1* mutant grown on control and Mn²⁺-deficient plates.

(C) Primary root length of Col-0 and *bicat3-1* grown on control and Mn²⁺-deficient plates.

(D) Primary root growth rate of Col-0 and *bicat3-1* grown on control and Mn²⁺-deficient plates.

(B) to (D) Data represents means ±SE of four plates containing six plants of each genotype. Data were analyzed by two-tailed Student's *t* test to identify significant differences between wild type and mutant (**, P < 0.01). The experiment was repeated at least twice with similar results.

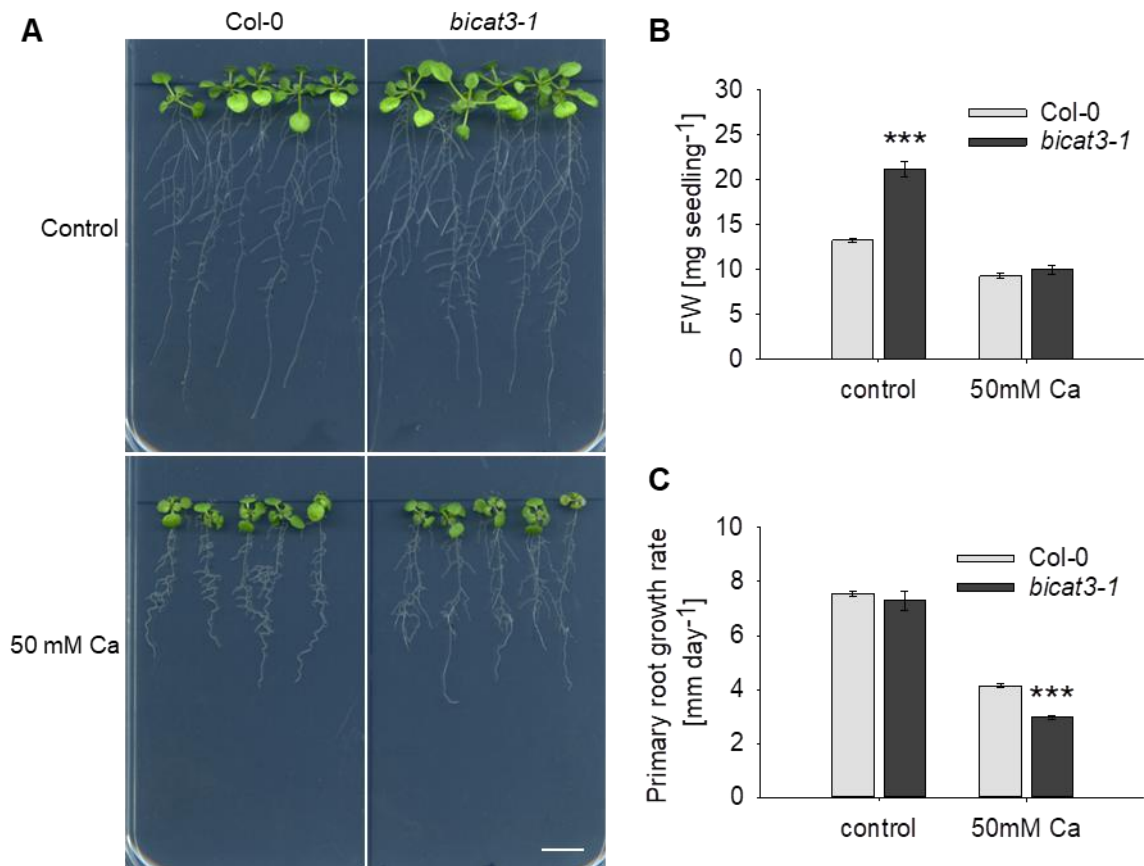


Figure 11. *bicat3-1* shows retarded root growth compared to the wild type under Ca^{2+} toxicity (50 mM CaCl_2).

(A) Growth phenotypes of 15-day-old Col-0 and *bicat3-1*. Seedlings grew for 7 d on control plates, were subsequently transferred to control and Ca^{2+} -toxic plates, and cultured for another 8 d. Scale bar represents 1 cm.

(B) Fresh weight (FW) of Col-0 and *bicat3-1* mutant grown on control and Ca^{2+} -toxic plates.

(C) Primary root growth rate of Col-0 and *bicat3-1* grown on control and Ca^{2+} -toxic plates. Data represent means \pm SE of three plates containing five plants of each genotype.

(B) and **(C)** Data were analyzed by two-tailed Student's *t* test to identify significant differences between wild type and mutant (***, $P < 0.001$). The experiment was repeated at least twice with similar results.

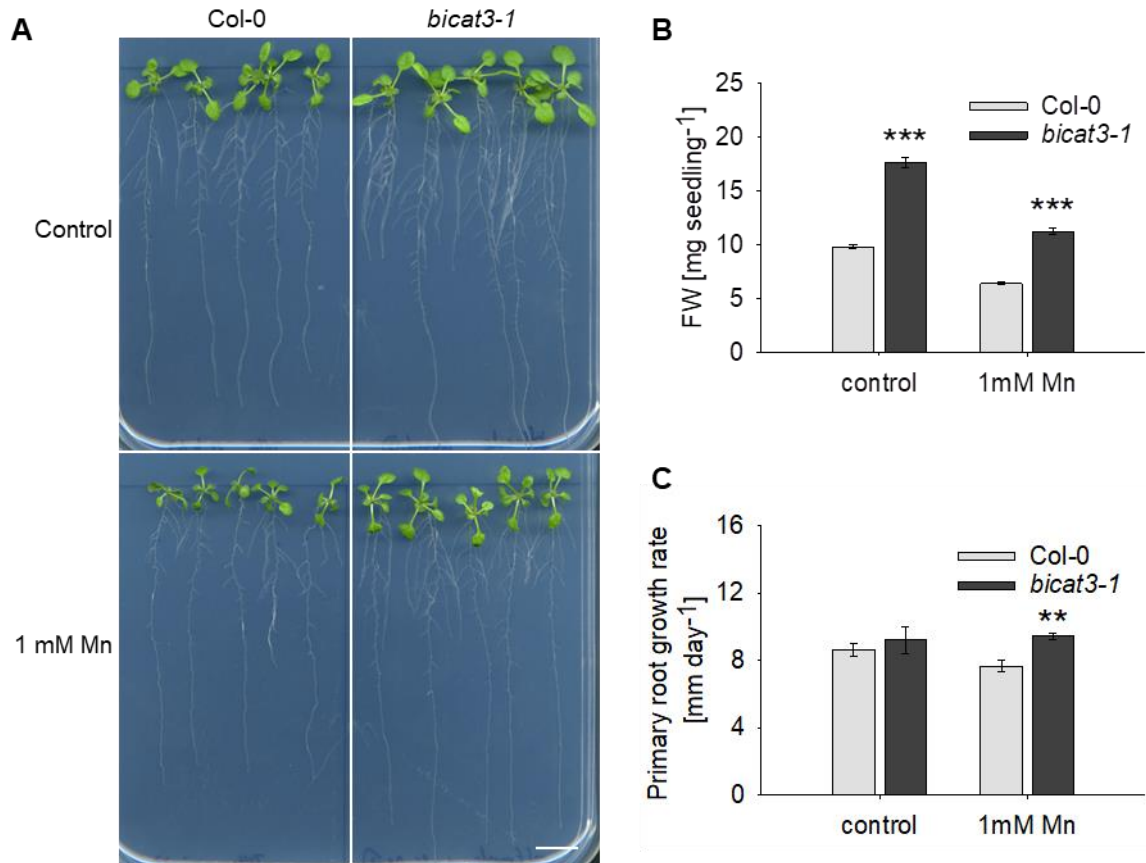


Figure 12. *bicat3-1* shows improved growth compared to the wild type under Mn²⁺ toxicity (1 mM MnSO₄).

(A) Growth phenotypes of 15-day-old Col-0 and *bicat3-1*. Seedlings grew 7 d on control plates, were subsequently transferred to control and Mn²⁺-toxic plates, and cultured for another 8 d. Scale bar represents 1 cm.

(B) Fresh weight (FW) of Col-0 and *bicat3-1* mutant grown on control and Mn²⁺-toxic plates.

(C) Primary root growth rate of Col-0 and *bicat3-1* grown on control and Mn²⁺-toxic plates.

(B) and **(C)** Data represent means ±SE of three plates containing five plants of each genotype. Data were analyzed by two-tailed Student's *t* test to identify significant differences between wild type and mutant (**, *P* < 0.01; ***, *P* < 0.001). The experiment was repeated at least twice with similar results.

To gain further insights into *bicat3* mutant phenotypes and to examine the function of BICAT3 in older plants, *bicat3-1* and wild type were cultured in hydroponics with different Mn²⁺ and Ca²⁺ supply (Figure 13).

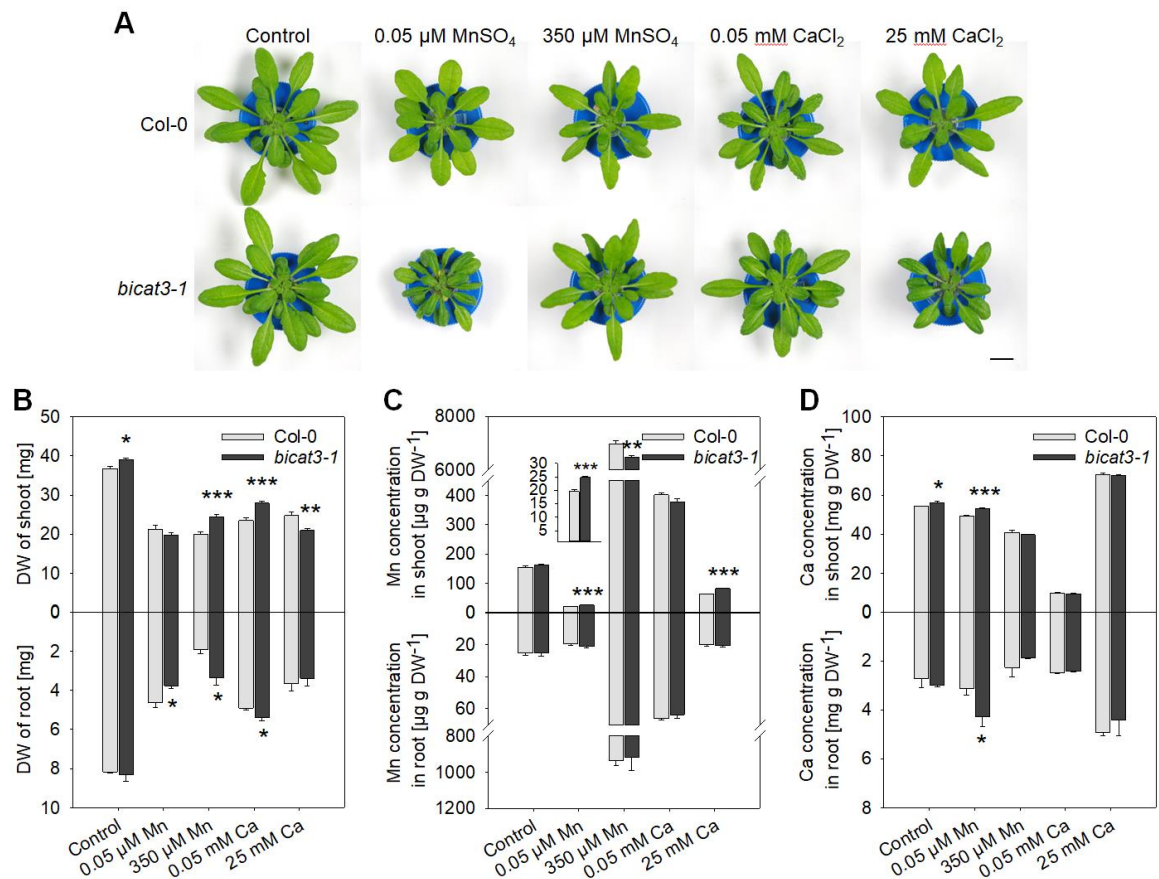


Figure 13. *bicat3-1* and wild type growth phenotype under different Ca^{2+} and Mn^{2+} supply.

(A) Growth phenotypes of Col-0 and *bicat3-1* under Mn^{2+} and Ca^{2+} treatments. Scale bar represents 1 cm.

(B) Shoot and root dry weight (DW) of Col-0 and *bicat3-1*.

(C) and (D) Mn^{2+} and Ca^{2+} concentration of Col-0 and *bicat3-1* shoots and roots. Data indicate means +SE of five independent biological replicates. Data were analyzed by two-tailed Student's *t* test to identify significant differences between wild type and mutant (*, $P < 0.05$; **, $P < 0.01$; ***, $P < 0.001$).

The experiment was repeated at least twice with similar results.

Under non-stressed conditions, *bicat3-1* shoot growth was slightly higher than that of the wild type (Figure 13A, B). Under surplus Mn^{2+} (350 μM MnSO_4) or deficient Ca^{2+} (0.05 mM CaCl_2) supply, shoot and root growth of *bicat3-1* were enhanced compared to the wild type. In contrast, shoot growth of *bicat3-1* was more sensitive to elevated Ca^{2+} (25 mM CaCl_2) than that of the wild type. The visually most striking difference was found under Mn^{2+} deficiency (0.05 μM MnSO_4). Under this condition, the size of the *bicat3-1* shoot was much smaller

than that of the wild type, and leaves of the mutant became curled (Figure 13A). However, despite this decrease in shoot size, shoot biomass was comparable to the Mn^{2+} -deficient wild type, whereas root biomass was reduced in *bicat3-1* (Figure 13B). The *bicat3-2* mutant showed the same growth phenotypes as *bicat3-1* under Mn^{2+} deficiency (Figure 14A).

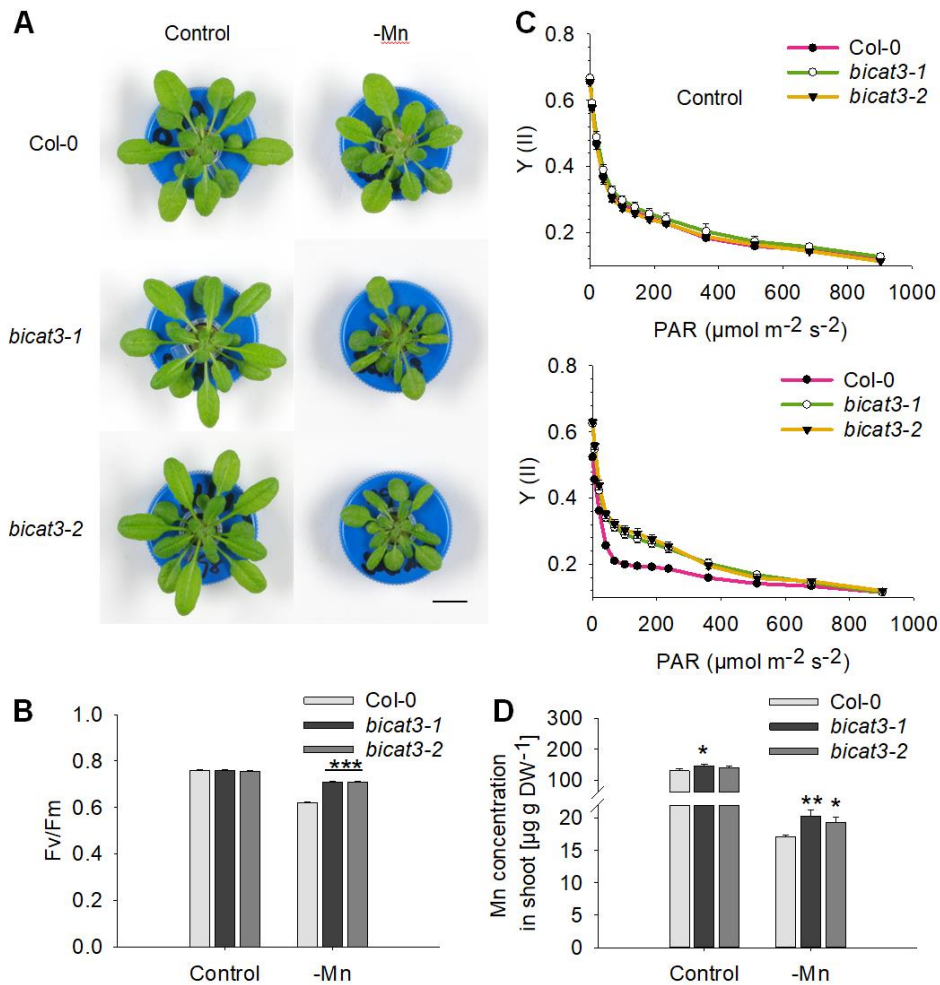


Figure 14. Phenotypes of Col-0, *bicat3-1*, and *bicat3-2* under control and Mn^{2+} deficiency (0.05 $\mu\text{M MnSO}_4$) conditions.

(A) Growth phenotypes of Col-0, *bicat3-1*, and *bicat3-2*. Scale bar represents 1 cm.

(B) Fv/Fm of Col-0, *bicat3-1*, and *bicat3-2*. Data indicate means +SE of three biological replicates.

(C) Efficiency of photosystem II [Y (II)] of Col-0, *bicat3-1*, and *bicat3-2*. Data indicate means \pm SE of three biological replicates.

(D) Mn concentrations in shoots of Col-0, *bicat3-1* and *bicat3-2*. Data indicate means +SE of five biological replicates. Data were analyzed by two-tailed Student's *t* test to identify significant differences between wild type and mutant (*, $P < 0.05$; **, $P < 0.01$; ***, $P < 0.001$).

The experiment was repeated at least twice with similar results.

To analyze the role of BICAT3 in Ca^{2+} and Mn^{2+} homeostasis, we measured Ca and Mn concentrations in shoots and roots of *bicat3-1* and wild type. Under adequate Mn^{2+} and Ca^{2+} supply, *bicat3-1* did not differ in Mn concentrations compared to the wild type, but had a higher Ca concentration in shoots (Figure 13C and 13D). However, under Mn^{2+} deficiency and Ca^{2+} toxicity, the Mn concentration in *bicat3* shoots was elevated in comparison to the wild type, while *bicat3-1* shoots accumulated less Mn than the wild type under Mn^{2+} toxicity (Figure 13C). Interestingly, the Ca concentration in Mn^{2+} -deficient *bicat3-1* shoots and roots was higher compared to the wild type (Figure 13D). Altogether, BICAT3 plays a central role in the plant's resilience to Mn^{2+} deficiency and contributes to Ca^{2+} and Mn^{2+} homeostasis in *A. thaliana*.

3.4 *bicat3* mutants accumulate a higher concentration of manganese in chloroplasts and have an improved photosynthesis under Mn^{2+} deficiency

Growth of *bicat3* mutants was severely depressed under Mn^{2+} deficiency. A decrease in photosynthetic activity is the most prominent phenotype of this nutritional disorder (Alejandro et al., 2020). We therefore determined photosynthetic efficiency by chlorophyll fluorescence analysis. Intriguingly, despite the retarded growth of *bicat3* mutants, both lines showed a significantly higher maximum quantum yield of photosystem II (Fv/Fm) and effective quantum yield of photosystem II [Y (II)] (Figures 14B-C, 15A-B).

We hypothesized that this improvement was caused by an enhanced supply of PSII with Mn. Whole-plant analysis had shown before that *bicat3* mutants accumulate more Mn in shoot compared to the wild type under Mn^{2+} deficiency (Figures 13C; 14D). To examine if the increase in photosynthetic activity of *bicat3* mutants is directly related to an increased accumulation of Mn in chloroplasts, we isolated chloroplasts and determined their Mn concentration by inductively coupled plasma - mass spectrometry (ICP-MS). Interestingly, *bicat3-1* contained a higher

Mn content in the chloroplast than the wild type under Mn^{2+} deficiency (Figure 15C), demonstrating that BICAT3 determines cellular Mn^{2+} distribution, including Mn^{2+} homeostasis in chloroplasts, which may subsequently have an effect on photosynthetic activity.

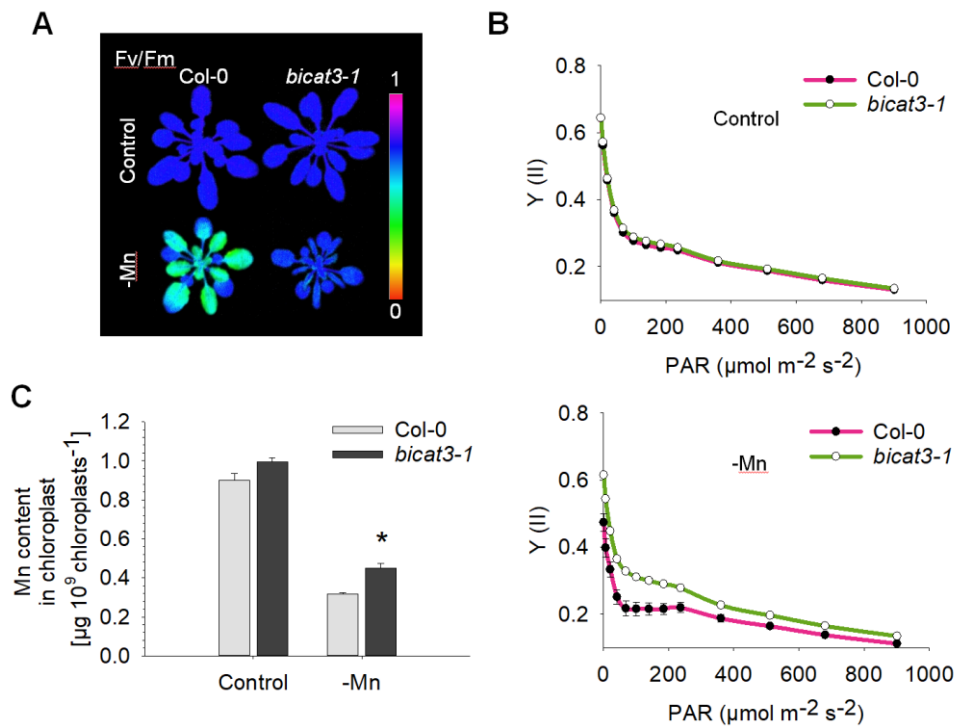


Figure 15. Absence of BICAT3 causes higher Mn content of chloroplasts and improved photosynthesis compared to the wild type under Mn^{2+} deficiency ($0.05 \mu M MnSO_4$).

(A) Fv/Fm images of Col-0 and *bicat3-1* plants under control and Mn^{2+} -deficient conditions.

(B) Efficiency of photosystem II [Y (II)] under control and Mn^{2+} deficiency. Data indicate means \pm SE of six biological replicates.

(C) Mn content of Col-0 and *bicat3-1* chloroplasts under control and Mn^{2+} -deficient conditions. Data indicate means \pm SE of four replicates. Data were analyzed by two-tailed Student's *t* test to identify significant differences between wild type and mutant (*, $P < 0.05$).

The experiment was repeated at least twice with similar results.

To determine the Mn^{2+} dependency of the improved photosynthetic activity in *bicat3* mutants, they were grown under mildly ($0.15 \mu M MnSO_4$) and severely ($0.05 \mu M MnSO_4$) deficient conditions. Both conditions led to an improved Fv/Fm in *bicat3-1* compared to the wild type (Figure 16).

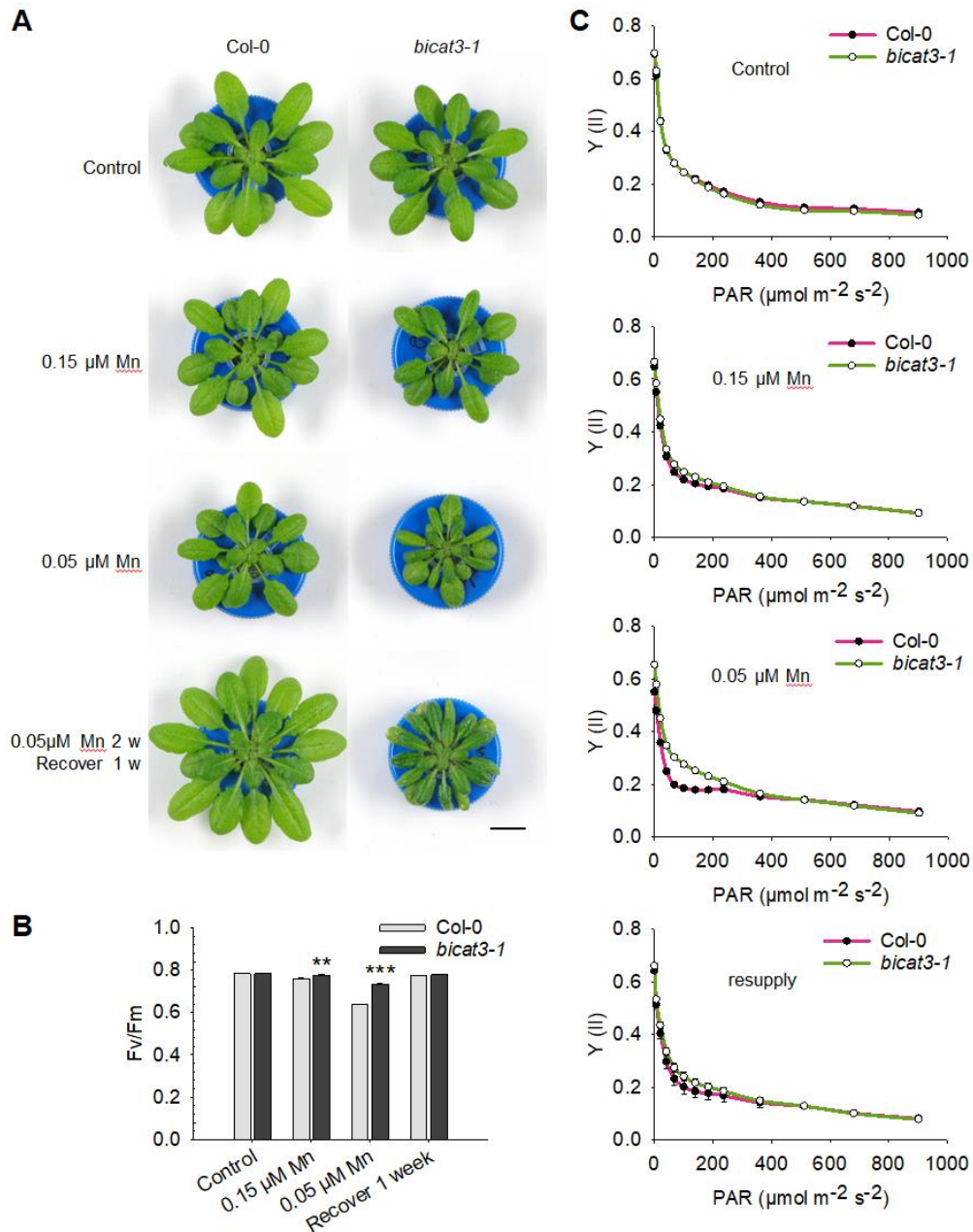


Figure 16. Phenotypes of Col-0 and *bicat3-1* under different Mn^{2+} (MnSO_4) supply levels.

(A) Growth of Col-0 and *bicat3-1* plants grown in medium containing 3.5 μM , 0.15 μM , or 0.05 μM Mn^{2+} , and following a 1-week resupply of 3.5 μM Mn^{2+} after 2 weeks in 0.05 μM Mn^{2+} . Scale bar represents 1 cm.

(B) Fv/Fm of Col-0 and *bicat3-1* under different Mn^{2+} supply and after Mn^{2+} resupply. Data indicate means \pm SE of five and four biological replicates of Col-0 and *bicat3-1*, respectively.

(C) Efficiency of photosystem II [Y (II)] of Col-0 and *bicat3-1* under different Mn^{2+} supply and after Mn^{2+} resupply. Data indicate means \pm SE of five and four biological replicates of Col-0 and *bicat3-1*, respectively. Data were analyzed by two-tailed Student's *t* test to identify significant differences between wild type and mutant (**, $P < 0.01$; ***, $P < 0.001$).

The experiment was repeated at least twice with similar results.

The differences in Fv/Fm between *bicat3-1* and wild type increased with increasing degree of Mn²⁺ deficiency and could be reversed by a resupply with Mn²⁺ for one week. Pronounced differences in Y(II) between *bicat3-1* and wild type were only obtained under severe Mn²⁺ deficiency, which was also reversible by Mn²⁺ resupply. In contrast to photosynthetic parameters, the abnormal leaf morphology of *bicat3-1* under severe Mn²⁺ deficiency did not change after Mn²⁺ resupply (Figure 16A).

To determine if the prominent shoot phenotypes of *bicat3* mutants are controlled systemically by the roots or locally in the shoot, reciprocal grafting of *bicat3-1* and wild-type seedlings was performed. Plants consisting of *bicat3-1* shoot and wild-type root (*bC*) showed identical shoot phenotypes to *bicat3-1* self-grafted plants (*bb*) (Figure 17). On the other hand, plants consisting of wild-type shoot and *bicat3-1* root (*Cb*) showed a shoot phenotype similar to wild-type self-grafted plants (*CC*). Regardless of the amount of Mn²⁺ supplied, grafted plants comprising *bicat3-1* roots (*Cb* and *bb*), accumulated higher shoot Ca concentrations (Figure 17F). Taken together, BICAT3 contributes differentially to Ca²⁺ and Mn²⁺ utilization in roots and shoots. Higher Ca concentrations in the *bicat3-1* shoots are caused by the absence of BICAT3 in roots, while improved photosynthetic activities, higher shoot Mn concentrations, and the curly-leaf phenotype of *bicat3-1* under Mn²⁺ deficiency are due to its function in the shoot.

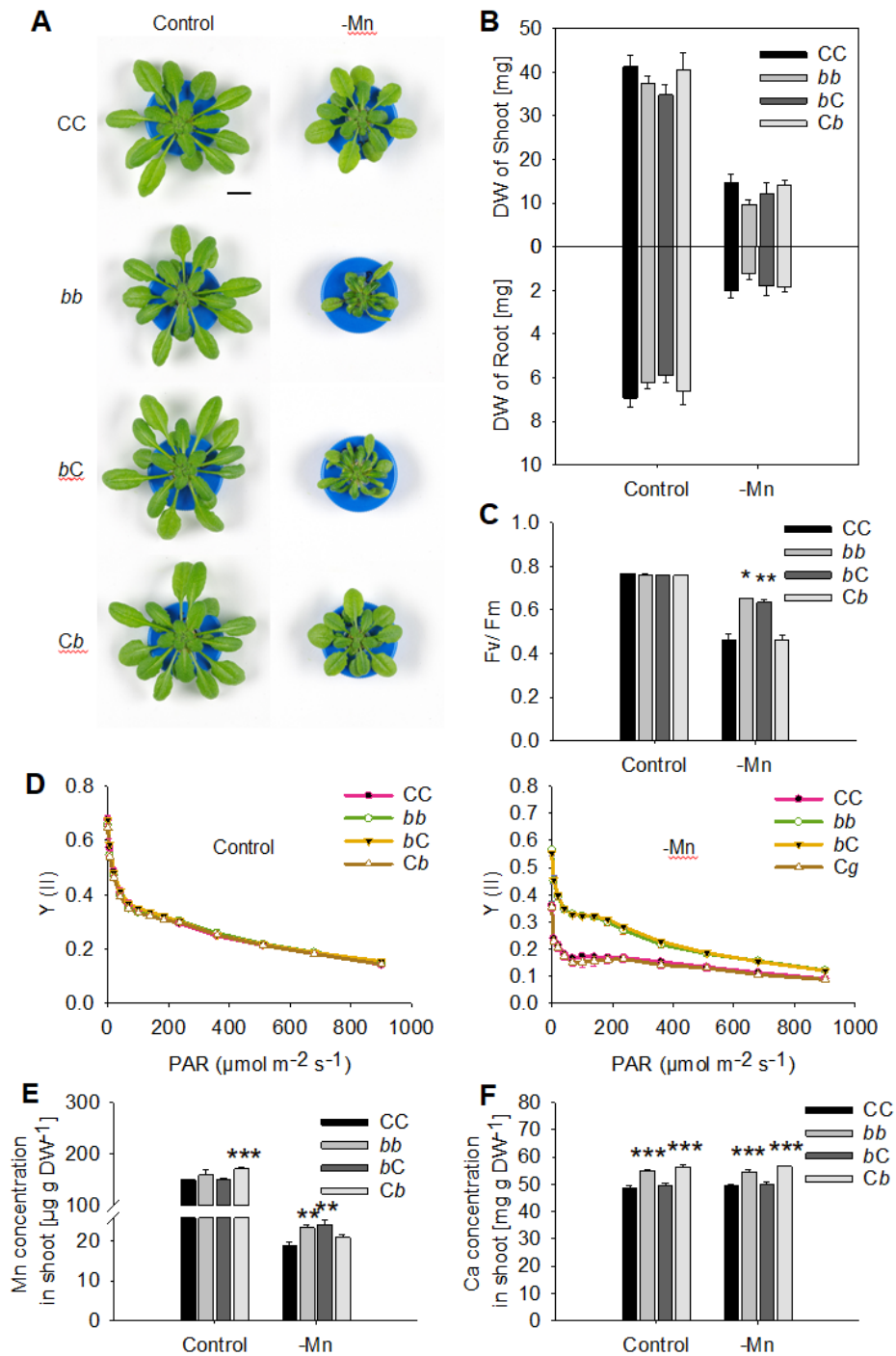


Figure 17. Phenotypes of Col-0 and *bicat3-1* reciprocally grafted plants under control and Mn^{2+} deficiency ($0.05 \mu\text{M MnSO}_4$) conditions.

(A) Growth phenotypes of grafted plants. CC, Col-0 shoot and Col-0 root; *bb*, *bicat3-1* shoot and *bicat3-1* root; *bC*, *bicat3-1* shoot and Col-0 root; *Cb*, Col-0 shoot and *bicat3-1* root. Scale bar represents 1 cm.

(B) Dry weight of shoots and roots of grafted plants.

(C) Fv/Fm of grafted plants. Data indicate means +SE of four biological replicates of *bb* and *Cb* under control and three independent biological replicates of all other grafting combinations under control and Mn²⁺ deficiency conditions.

(D) Efficiency of photosystem II [Y (II)] of grafted plants. Data indicate means ±SE of four biological replicates of *bb* and *Cb* under control and three independent biological replicates of all other grafting combinations under control and Mn²⁺ deficiency conditions.

(E) Mn concentrations in shoots of grafted plants.

(F) Ca concentrations in shoots of grafted plants.

Data in (B), (E), and (F) indicate means +SE of four biological replicates of *bb* under control and six biological replicates of all other grafting combinations under control and Mn²⁺ deficiency conditions. Data were analyzed by two-tailed Student's *t* test to identify significant differences between *bb*, *bC*, *Cb*, and CC (*, P<0.05**, P< 0.01; ***, P<0.001).

The experiment was repeated at least twice with similar results.

3.5 BICAT3 is essential for glycosylation and matrix polysaccharide biosynthesis under low Mn²⁺ availability

As mentioned before, one of the most notable changes in the morphology of the *bicat3* mutants is the curly leaf symptom under Mn²⁺ deficiency (Figures 14A, 18A). Cross-sections of *bicat3-1* leaf blades grown under Mn²⁺-deficient conditions showed extremely compacted mesophyll cells with diminished intercellular air space (Figure 18B) accompanied by smaller palisade mesophyll cells, spongy mesophyll cells, and lower epidermis cells compared to the wild type (Figure 18C, D). Moreover, the spongy mesophyll cells were more rounded than those of the wild type under Mn²⁺ deficiency (Figure 18E).

Plant cell size regulation is a highly complex process, encompassing cell growth and cell division (Marshall et al., 2012). Among those determinants, the cell wall, composed of multifarious sugars and some proteins, is a key regulator that confines the expansion of plant cells (Cosgrove, 2018). The Golgi apparatus is critical for cell wall synthesis, as it is important for post-translational modification of proteins (Strasser, 2016) and matrix polysaccharide synthesis (Driouch et al., 2012). Mn²⁺ is indispensable for the glycosylation of proteins and the synthesis of complex matrix sugars in the Golgi (Alejandro et al., 2020). Hence, we checked if the cell wall matrix sugar composition and the glycoprotein pattern were changed

in *bicat3* mutants, which showed striking differences in growth compared to the wild type under Mn^{2+} deficiency. Matrix sugar analysis was performed by Bo Yang and Catalin Voiniciuc (IPB Halle).

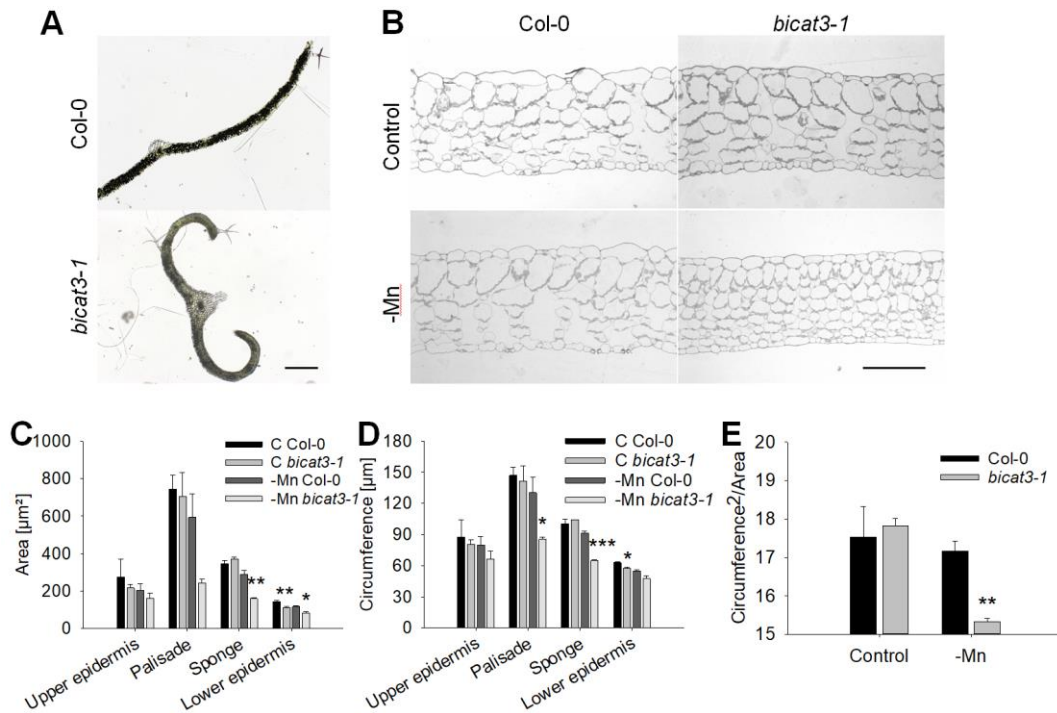


Figure 18. The cell size and shape of *bicat3-1* leaves change under Mn^{2+} deficiency (0.05 μM $MnSO_4$) compared to the wild type.

(A) Cross sections of Col-0 and *bicat3-1* leaf under Mn^{2+} deficiency. Scale bar represents 500 μm .

(B) Cross sections of Col-0 and *bicat3-1* leaf blade under control and Mn^{2+} deficiency. Scale bar represents 100 μm .

(C) Areas of different types of cells of Col-0 and *bicat3-1* leaf blade under control and Mn^{2+} deficiency.

(D) Circumferences of different types of cells of Col-0 and *bicat3-1* leaf blade under control and Mn^{2+} deficiency.

(E) Shape factor (circumference²/area) of spongy mesophyll cells under control and Mn^{2+} deficiency.

(C) to (E). Depending on the amount of cells in each sections, 10-100 cells were quantified in each section. The means of all cells from two sections of the same leaf were calculated and averaged, representing one biological replicate. Data represent the means +SE of three biological replicates. Data were analyzed by two-tailed Student's *t* test to identify significant differences between wild type and mutant (*, $P < 0.05$; **, $P < 0.01$; ***, $P < 0.001$). Experiment was conducted in collaboration with Gerd Hause.

When comparing the monosaccharide abundance in *bicat3* and wild-type cell wall fractions under Mn²⁺ deficiency, numerous alterations were detected (Figure 18A). The abundance of fucose (Fuc), galactose (Gal), xylose (Xyl), and galacturonic acid (GalA) was decreased in shoot cell walls of both Mn²⁺-deficient *bicat3* mutants as compared to the Mn²⁺-deficient wild type (Figure 19A). Conversely, the abundance of glucose (Glc), rhamnose (Rha), and mannose (Man) in shoot cell walls of Mn²⁺-deficient *bicat3* was significantly higher compared to those of wild-type plants.

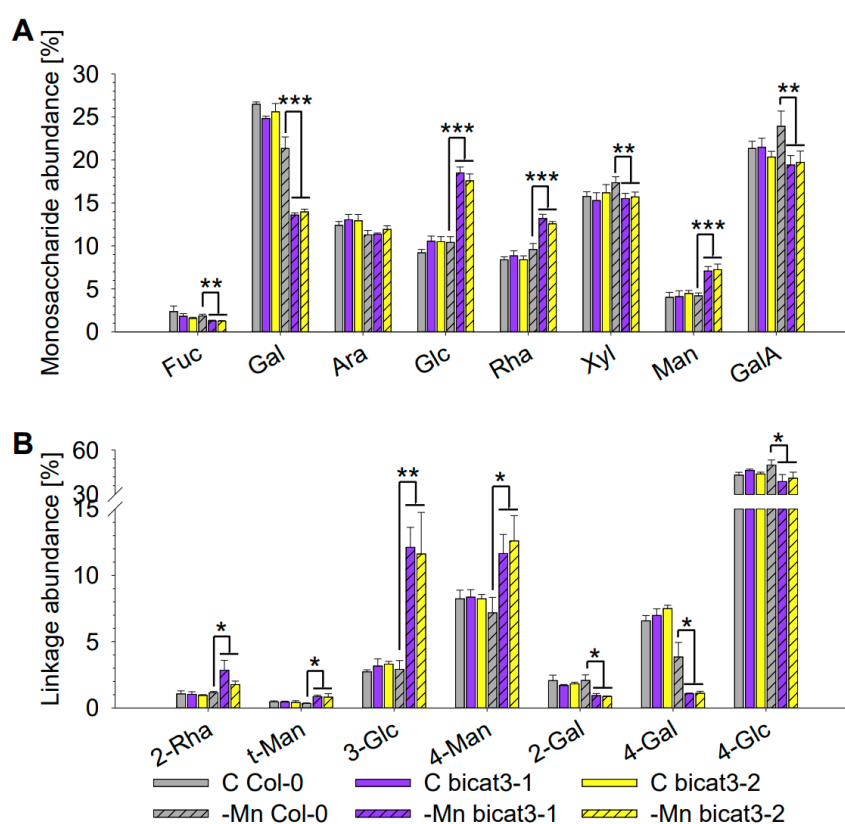


Figure 19. Cell wall matrix sugar components are affected in *bicat3* shoots compared to the wild type under Mn²⁺ deficiency (0.05 μM MnSO₄).

(A) Monosaccharide analysis of Col-0 and *bicat3* mutant shoot cell wall alcohol-insoluble residues. (B) Glycosidic linkage analysis of Col-0 and *bicat3* mutant shoot cell wall alcohol-insoluble residues. Values represent molar percentage of total carbohydrates detected.

(A) and (B). Data indicate means +SD of four independent biological replicates. Data were analyzed by two-tailed Student's *t* test to identify significant differences between wild type and mutants (*, P<0.05; **, P< 0.01; ***, P<0.001). Experiment was conducted in collaboration with Bo Yang and Catalin Voiniciuc.

To determine which polysaccharides were affected by the altered monomer composition, a linkage analysis was pursued. Linkage patterns were massively altered in Mn^{2+} -deficient *bicat3* mutants as compared to the wild type. The abundance of 2-Rha, t-Man, 3-Glc, and 4-Man linkages was significantly increased, while the abundance of 2-Gal, 4-Gal and 4-Glc linkages was severely diminished in shoot cell walls of those plants (Figure 19B). The highly elevated abundance of 3-Glc indicated an accumulation of callose in *bicat3* shoots under Mn^{2+} deficiency. This was confirmed by immunogold and aniline blue staining of callose (Figure 20).

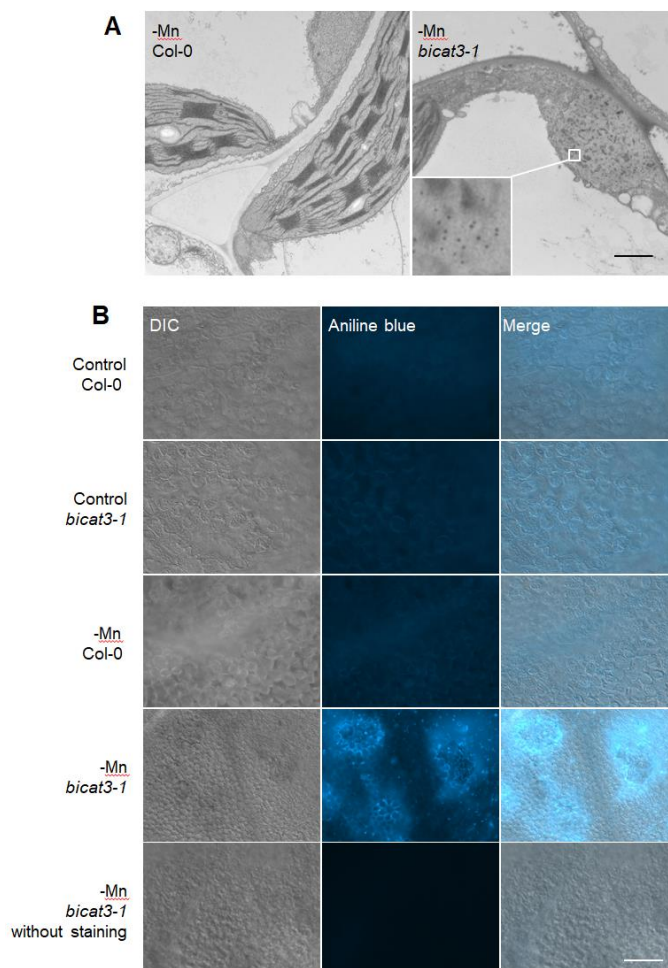


Figure 20. *bicat3-1* accumulates more callose in leaves compared to the wild type under Mn^{2+} deficiency (0.05 μM $MnSO_4$).

(A) Callose accumulation in Mn^{2+} -deficient *bicat3-1* leaf cell detected by immunogold staining. Scale bar represents 1 μm . Experiment was conducted in collaboration with Gerd Hause.

(B) Callose accumulation in Col-0 and *bicat3-1* leaf detected by aniline blue staining. Scale bar represents 100 μm . The experiment was repeated at least twice with similar results.

The glycoprotein pattern was analysed by Western blot with a Concanavalin A (ConA) antibody. With sufficient Mn^{2+} supply, the glycoprotein pattern of *bicat3* mutant shoots detected by ConA was similar to that of wild-type shoots (Figure 21). While the glycoprotein pattern remained unchanged in the wild type under Mn^{2+} deficiency, it was altered in the *bicat3* mutants. Altogether, the results demonstrate that BICAT3 is pivotal for protein glycosylation and polysaccharide synthesis under limited Mn^{2+} supply.

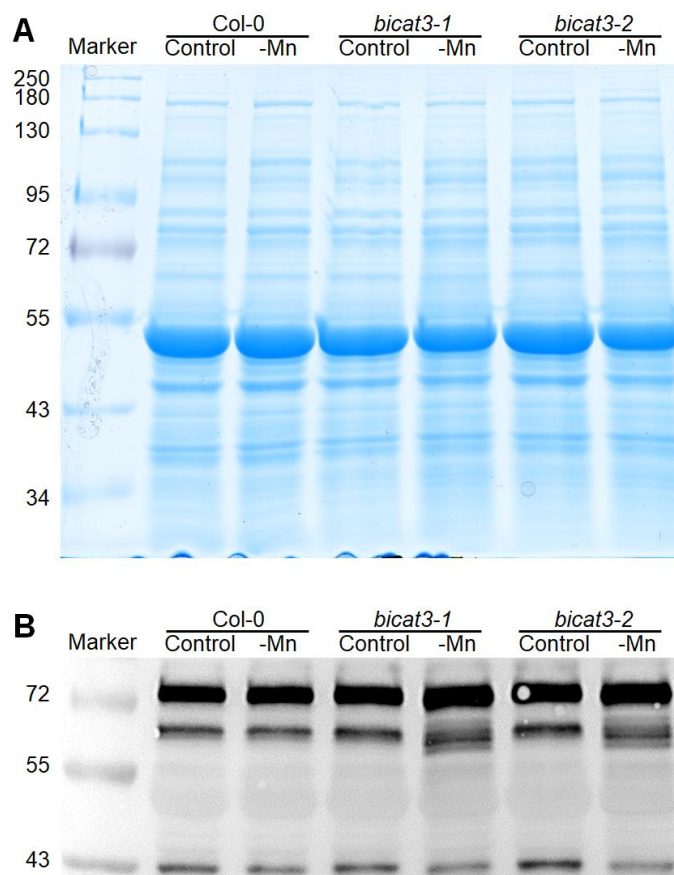


Figure 21. Glycoprotein pattern of *bicat3-1* shoots is altered by Mn^{2+} deficiency (0.05 μM $MnSO_4$) in *bicat3* mutants.

(A) Coomassie Blue-stained SDS-polyacrylamide gel.

(B) Glycoproteins detected by Concanavalin A (ConA) antibody which recognizes internal and non-reducing terminal α -D-mannosyl and α -D-glucosyl groups of glycoproteins.

The experiment was repeated at least twice with similar results.

3.6 Mutation of *BICAT3* hampers pollen tube growth and the development of siliques

Besides the vegetative growth aberrance under Mn^{2+} limitation, the *bicat3* lines displayed a severe generative growth defect: both mutants produced short siliques with an incomplete seed set (Figures 22, 23A-B). Additionally, *bicat3* mutant seeds were significantly larger, heavier, and germinated faster than wild-type seeds (Figure 24). To assess the biological basis of the short-silique phenomenon, reciprocal crosses between *bicat3-1* and wild type were performed. Siliques obtained from crosses of *bicat3-1* pollen with maternal *bicat3-1* or wild type showed a reduced length compared to those from the wild-type self-cross, whereas the siliques from *bicat3-1* flowers fertilized with wild-type pollen were comparable to those from wild-type self-cross (Figure 23C). This result indicates a male gametophyte defect to be responsible for the short-silique phenotype.

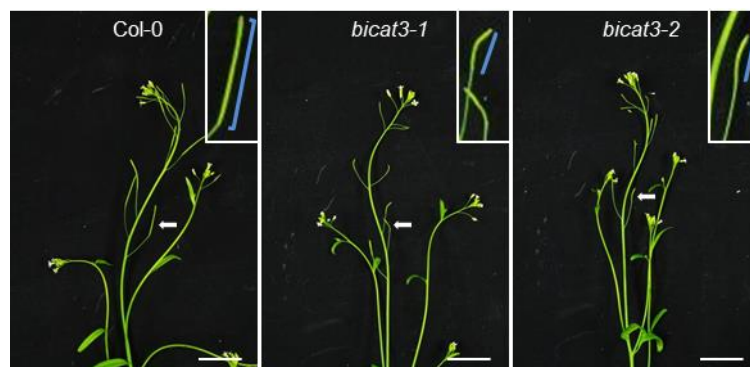


Figure 22. *bicat3-1* and *bicat3-2* mutants produce shorter siliques compared to the wild type.

Plants were grown under greenhouse conditions. Scale bars represent 2 cm.

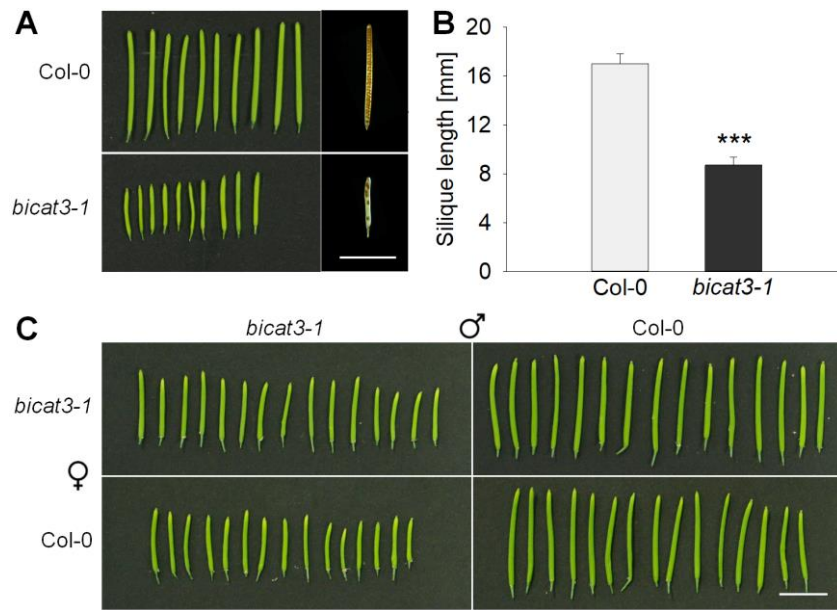


Figure 23. The *bicat3-1* mutant shows male gametophyte defects that lead to shorter siliques compared to the wild type.

(A) Siliques of Col-0 and *bicat3-1*. Scale bar represents 1 cm.

(B) Silique length of Col-0 and *bicat3-1*. Data indicate means +SE of ten siliques. Data were analyzed by two-tailed Student's *t* test to identify significant differences between wild type and mutant (***, $P < 0.001$).

(C) Reciprocal crossing of Col-0 and *bicat3-1*. Scale bar represents 1 cm.

The experiment was repeated at least twice with similar results.

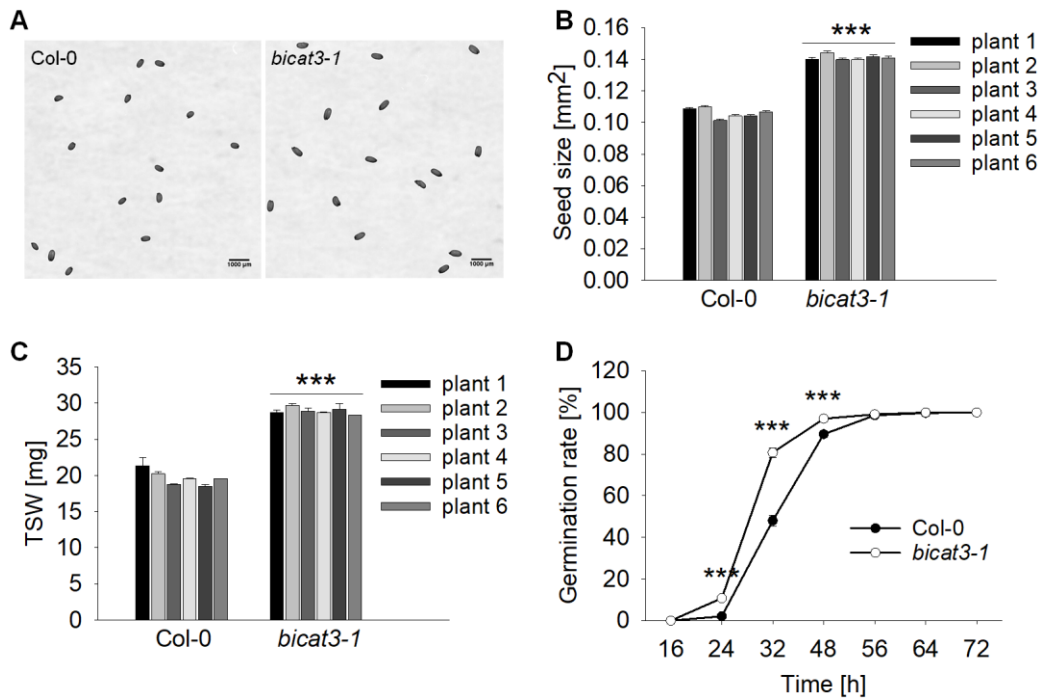


Figure 24. The *bicat3-1* mutant produces bigger seeds and germinates faster than the wild type.

(A) Col-0 seeds (left) and *bicat3-1* seeds (right). Scale bars represent 1 mm.

(B) Seed size of *bicat3-1* and Col-0. Data indicate means +SE of at least two hundred seeds per plant.

(C) Thousand seed weight of *bicat3-1* and Col-0. Data indicate means +SE of three technical replicates.

(D) Germination of *bicat3-1* and Col-0 seeds. Data indicate means +SE of seven replicates with at least sixty seeds.

(B) to (D) Data were analyzed by two-tailed Student's *t* test to identify significant differences between wild type and mutants (***, $P < 0.001$).

The experiment was repeated at least twice with similar results.

This observation provoked the question whether *BICAT3* is active in pollen. The expression of *BICAT3* in pollen grains and tubes was confirmed in both *ProBICAT3-GUS* and *ProBICAT3-BICAT3-Venus* reporter lines (Figure 25A-B), suggesting a direct role of *BICAT3* in pollen. Aniline blue staining of pollen tubes grown for 24 h *in vivo* showed that only a minor proportion of *bicat3-1* pollen tubes grew normally and reached the basal end of the transmitting tract (Figure 25C). To confirm the defect of mutant pollen tube elongation, pistils were pollinated, and the top part of pollinated pistils, including stigma and style, were excised and

subsequently cultured for 12 h. Under those *semi in vivo* conditions, only a few *bicat3-1* pollen tubes grew out of the cut *bicat3-1* and wild-type pistils after they were cultured on the medium for 12 h (Figure 25D). Contrastingly, numerous wild-type pollen tubes penetrated the stigma and style of *bicat3-1* and wild-type pistils and continued growing under the same conditions. The abnormal growth of pollen tubes was also observed in *bicat3-2* and can be complemented by the expression of *BICAT3* driven by its native promoter in *bicat3-1* background (Figure 26). Together, these results indicated that *BICAT3* is critical for pollen tube elongation and consequently seed production.

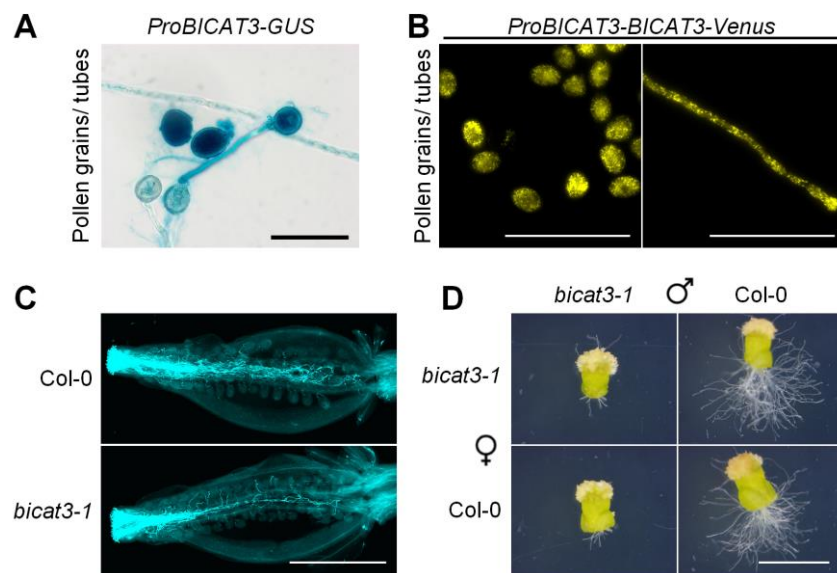


Figure 25. The absence of *BICAT3* hampers pollen tube growth.

(A) Activity of *BICAT3* promoter in pollen grains and pollen tubes as detected by GUS staining of *ProBICAT3-GUS* line. Scale bar 100 μ m.

(B) Activity of *BICAT3* promoter in pollen grains and pollen tubes of *ProBICAT3-BICAT3-Venus* line. Scale bars represent 100 μ m.

(C) Aniline blue staining of *Col-0* and *bicat3-1* pollen tubes grown *in vivo*. Scale bar represents 1 mm.

(D) *Semi in vivo* pollen tube growth assays of *Col-0* and *bicat3-1*. Pictures were taken 12 h after pollination. The whole set of figures is presented in Figure 26. Scale bar represents 1 mm.

The experiment was repeated at least twice with similar results.

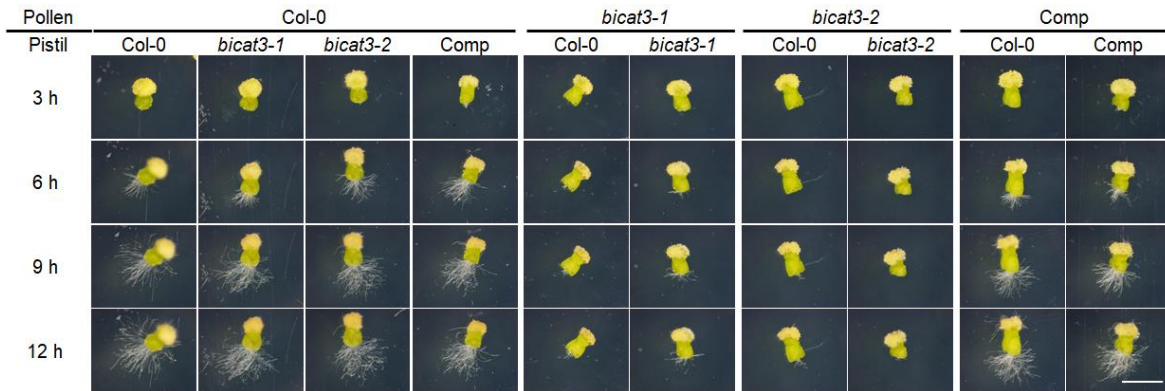


Figure 26. Semi *in vivo* pollen tube growth assays of Col-0, *bicat3-1*, *bicat3-2*, and complementation line (Comp) of *bica3-1* mutant.

Scale bar represents 1 mm. The experiment was repeated at least twice with similar results.

3.7 *bicat3* pollen tubes accumulate less low methyl-esterified homogalacturonan compared to wild-type pollen tubes

The absence of BICAT3 severely disturbed the matrix polysaccharides in vegetative tissue. Composition and distribution of cell wall polysaccharides, in particular pectin, are also crucial for pollen tube extensibility and growth (Hepler et al., 2013; Mollet et al., 2013; Dehors et al., 2019). We therefore hypothesized that the defective *bicat3* pollen tubes have an abnormal cell wall polymer composition and distribution. To examine cell wall composition, pollen was germinated *in vitro*. In addition to the retarded pollen tube growth of *bicat3* mutants observed *in vivo* and in *semi in vivo* growth assays (Figure 25C-D), *bicat3* pollen tubes showed swollen and branched phenotypes when grown *in vitro* (Figure 27). Unlike the pollen tubes of wild type and complementation line, which accumulated pectin close to the tips and showed a homogenous pectin distribution along tubes, both *bicat3* mutants showed pectin accumulation at branch points and less pectin at tips or swollen parts, as detected by ruthenium red staining (Figure 27).

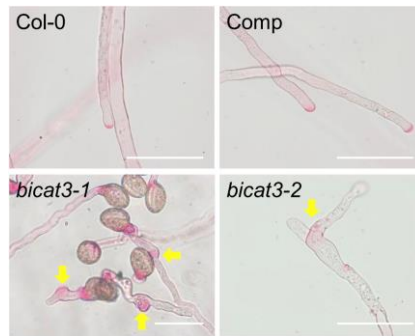


Figure 27. *bicat3* mutant pollen tubes grow aberrantly *in vitro* and show abnormal pectin distribution.

Pectin was detected by ruthenium red staining. Scale bar represents 50 μ m. The experiment was repeated at least twice with similar results.

Moreover, by immunostaining of pollen tubes grown *in vitro* with JIM5 antibody, which binds partially methyl-esterified and un-esterified homogalacturonan (PUHG), we found that both *bicat3* mutants accumulated significantly less PUHG in the apical region of most pollen tubes (Figure 28). PUHG showed a heterogeneous distribution in swollen and branched *bicat3* pollen tubes with increased accumulation at branch points or tips and much lower abundance in the other part of pollen tube tips (Figure 28A). This phenotype was abolished by complementation of *bicat3-1*, indicating that the irregular PUHG accumulation and distribution can be fully rescued by the expression of *BICAT3* in the *bicat3-1* mutant (Figure 28). In summary, the data demonstrate the requirement of *BICAT3* for pectin deposition, and consequently pollen tube elongation.

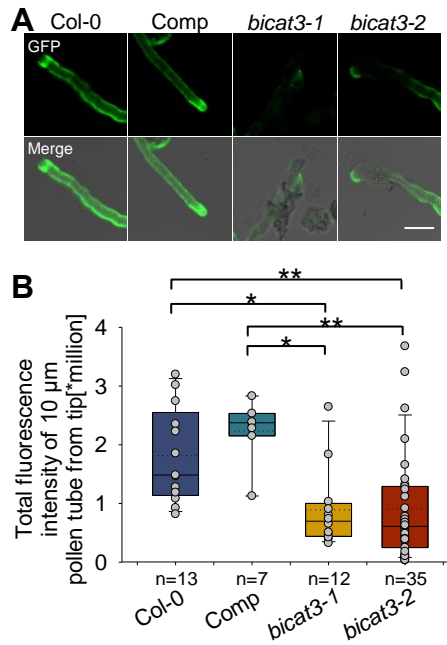


Figure 28. *bicat3* mutant pollen tubes contain less low methyl-esterified homogalacturonan compared to the wild type.

(A) *In vitro* immunofluorescence labeling of pollen tubes with anti-pectin monoclonal antibody JIM5. Scale bar represents 20 μ m. Experiment was conducted in collaboration with Gerd Hause.

(B) Total fluorescence intensity of pollen tubes (10 μ m from tip) of Col-0, *bicat3* complementation line, and *bicat3* mutants. The box plot shows the range of the value (upper and lower bar), median (black line), means (white dot line) and the lower and upper quartiles. Single data points are indicated by grey circles. Data were analyzed by Kruskal-Wallis one way analysis of variance on ranks with Dunn's method to identify significant differences between wild type and mutants or Comp and mutants (*, $P < 0.05$; **, $P < 0.01$).

The experiment was repeated at least twice with similar results.

4 Results II - Functional analysis of Golgi-localized HvBICAT3 using CRISPR/Cas9 genome editing in *H. vulgare*

4.1 BICAT proteins in *A. thaliana* and *H. vulgare*

There are five BICAT proteins that belong to the UPF0016 family in *A. thaliana*. Among these proteins, BICAT3 is localized in the Golgi apparatus and serves an essential role in supplying Mn^{2+} for biological processes in this compartment, as shown in the Results I section. To identify *H. vulgare* proteins that may serve similar functions, we used *A. thaliana* BICAT protein sequences in a blastp search of the IPK Galaxy Blast Suite and retrieved four HvBICATs. Based on the similarity to the *A. thaliana* proteins, we named HORVU.MOREX.r2.3HG0205390, HORVU.MOREX.r3.2HG0103720, HORVU.MOREX.r3.7HG0683450 and HORVU.MOREX.r3.7HG0640780 as HvBICAT1, HvBICAT2, HvBICAT3 and HvBICAT4, respectively (Figure 29A). The differences and similarities in the amino acids sequence of BICAT3 and HvBICAT3 were further analyzed by GeneDoc. The major difference between them is found in the N-terminal part, where HvBICAT3 has a shorter signal peptide compared to BICAT3 (Figure 29B). Nevertheless, they show the same sequence of conserved 'E-x-GD-(KR)-(ST)' motif and contain five transmembrane domains (TMDs) with similar in amino acids sequences (Figure 29B), indicating a potential similarity in their functions.

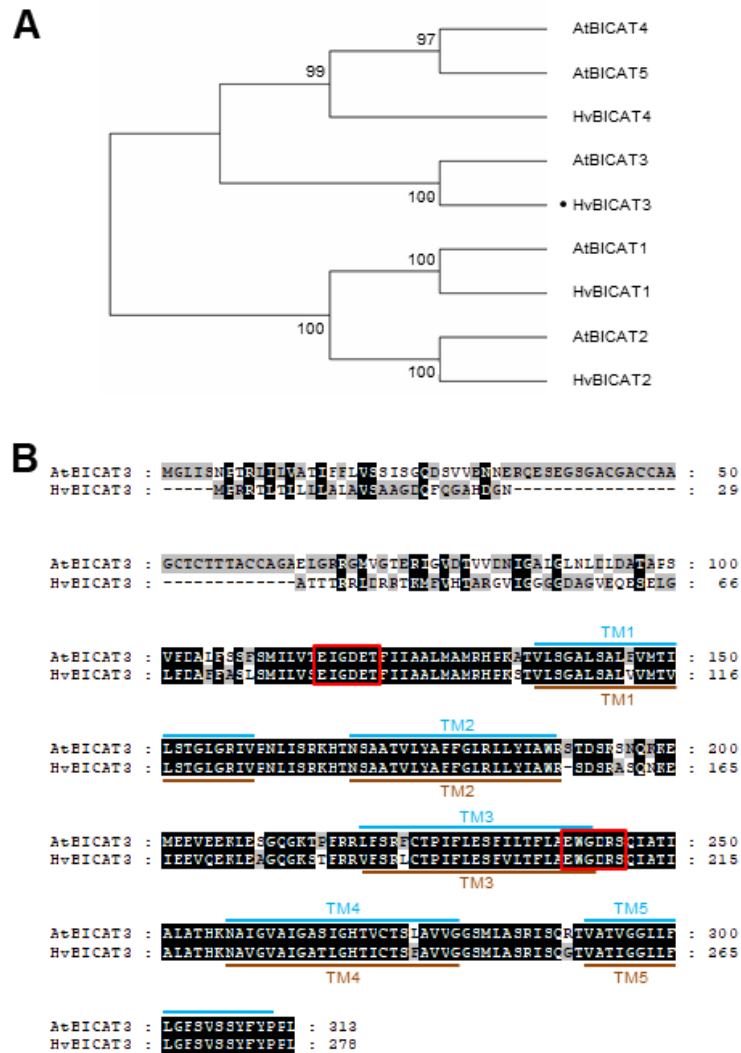


Figure 29. HvBICAT3 is similar to BICAT3.

(A) Phylogenetic tree of *A. thaliana* and *H. vulgare* BICAT proteins. The phylogenetic tree was generated by MEGA7 using the Neighbor-joining method. HvBICAT1 (HORVU.MOREX.r2.3HG0205390), HvBICAT2 (HORVU.MOREX.r3.2HG0103720), HvBICAT3 (HORVU.MOREX.r3.7HG0683450), HvBICAT4 (HORVU.MOREX.r3.7HG0640780).

(B) Sequence alignment of HvBICAT3 and BICAT3. Sequences were aligned by GeneDoc; Red rectangles indicate the consensus motif E-φ-G-D-(KR)-(TS); TMDs were predicted by TMHMM Server v.2.0. Blue lines indicate transmembrane domains (TMDs) of BICAT3; Brown lines indicate TMDs of HvBICAT3.

4.2 HvBICAT3 localizes to the Golgi apparatus

HvBICAT3 and BICAT3 differ in the N-terminal peptide, what may cause differences in their properties, in particular their localization. To investigate the subcellular localization of HvBICAT3, we co-expressed Venus-tagged HvBICAT3 in

H. vulgare mesophyll protoplasts. HvBICAT3 co-localized with a Golgi marker, mannosidase I (Man I) (Figure 30).

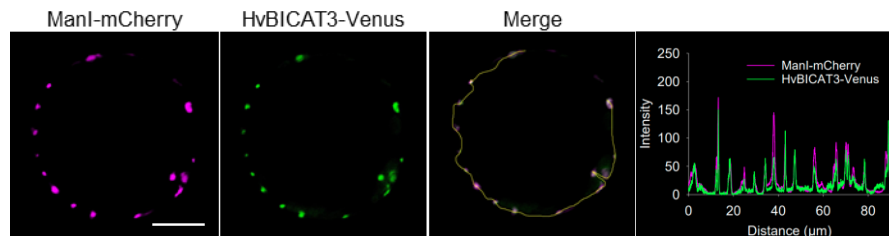


Figure 30. HvBICAT3 is localized in the Golgi apparatus.

HvBICAT3 was co-expressed with *cis*-Golgi marker (mannosidase I, ManI) in *H. vulgare* mesophyll protoplasts. Scale bar represent 10 μm .

4.3 HvBICAT3 acts as Ca^{2+} and Mn^{2+} transporter in yeast

It has been shown that BICAT3 (this work) and its orthologs in yeast and humans, Gdt1p and TMEM165 (Thines et al., 2018; Stribny et al., 2020), are critical for Ca^{2+} and Mn^{2+} homeostasis of the Golgi apparatus. To test if the Golgi-localized HvBICAT3 has similar functions, *HvBICAT3* was heterologously expressed in the *pmr1 Δ gdt1 Δ* mutant, which fails to load Ca^{2+} into the Golgi due to the absence of GDT1 and the Ca^{2+} pump PMR1. The *pmr1 Δ gdt1 Δ* mutant showed substantial growth retardation under Ca^{2+} toxicity. This defect was overcome by the expression of *HvBICAT3* (Figure 31A). Furthermore, expression of *HvBICAT3* slightly complemented the Mn^{2+} sensitivity of *pmr1 Δ* , albeit less pronounced than BICAT3 (Figure 31B). In conclusion, the results indicate that HvBICAT3 acts as a Ca^{2+} and Mn^{2+} transporter in yeast.

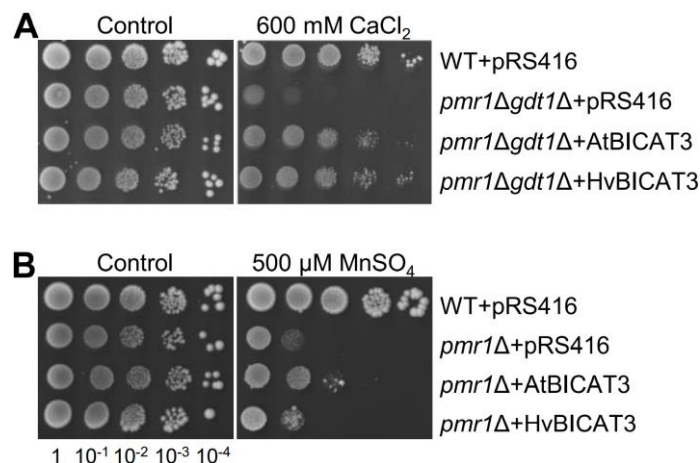


Figure 31. HvBICAT3 complements a Ca²⁺-sensitive yeast strain, and partially a Mn²⁺-sensitive yeast strain.

(A) Growth of wild type and *pmr1Δgdt1Δ* with and without *BICAT3* and *HvBICAT3* under Ca²⁺-toxic conditions. Liquid cultures of the strains were serially diluted and dropped onto AP media.

(B) Growth of wild type and *pmr1Δ* with and without *BICAT3* and *HvBICAT3* under Mn²⁺-toxic conditions. Liquid cultures of the strains were serially diluted and dropped onto SC-Ura media.

The experiment was repeated at least twice with similar results.

4.4 Design of *HvBICAT3* editing targets and constructs

To study the role of *HvBICAT3*, we retrieved its genomic sequence from the IPK Galaxy Blast Suite. *HvBICAT3* comprises 3288 bp and has nine exons. The coding sequence of two conserved 'E-x-GD-(KR)-(ST)' motives is localized in exon 4 and exon 8, respectively. To effectively knock out *HvBICAT3*, three single guide RNA (sgRNA) target sites which are upstream of one or two conserved motifs, localized in exon 3, exon 4 and exon 5, were selected (Figure 32A). The sgRNAs were cloned into the pMGE632 and pMGE634 recipient vectors (Johannes Stuttmann, unpublished). Both contain a *mVenus* fluorescent tag, and a double nuclear localization signal (2*NLS)-tagged intronized *Cas9* (*Cas9i*) under control of a *Zea mays Ubiquitin* promoter (*pZmUbi*). These vectors differ in the hygromycin resistance gene (*hpt*). pMGE634 contains an intronized *hpt* (*hpti*), while pMGE632 contains *hpt* without introns (Figure 32B-C). The intronized *hpt* was expected to increase transformation efficiency, which, however, was not observed. While 7

transformants were regenerated from 100 immature embryos transformed with pMGE632, only 3 transformants were regenerated from 100 embryos transformed with pMGE634.

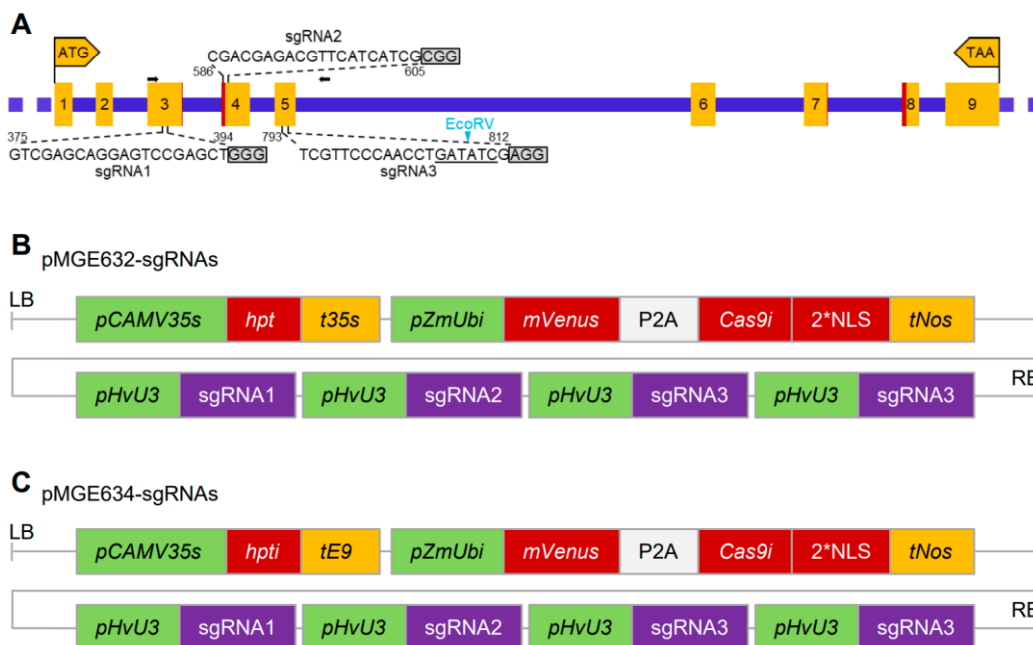


Figure 32. Targets and vectors for CRISPR/Cas9-mediated mutagenesis of *HvBICAT3*.

(A) Model of the genomic regions and target sites of the single guide RNAs (sgRNAs) in *HvBICAT3*. Coding regions are presented by yellow boxes; the red parts of the box indicate the coding region of two consensus E- ϕ -G-D-(KR)-(TS) motives; introns are shown by a purple line; numbers above sgRNAs indicate the first and the last nucleotide of sgRNAs, counting from the start codon; letters with a grey background indicate the protospacer adjacent motif (PAM). Arrows indicate the primers used for mutant screening, which have 638bp distance in between; the EcoRV restriction site is underlined; the triangle indicates the cleavage site of EcoRV.

(B) Schematic diagram of the T-DNA region of the pMGE632-sgRNAs construct for *SpCas9*-based and Agrobacterium-mediated *HvBICAT3* gene editing. Construct with CaMV 35S promoter (*pCAMV35s*), hygromycin phosphotransferase gene (*hpt*), CaMV 35S terminator (*t35s*), ubiquitin promoter of *Zea mays* (*pZmUbi*), monomeric yellow fluorescent protein-coding sequence (*mVenus*), 2A self-cleaving-peptide-coding sequence (P2A), *Streptococcus pyogenes* Cas9 with introns (*Cas9i*), two copies of nuclear localization signal (2*NLS), *nopaline synthase terminator* (*tNos*), *H. vulgare* U3 promoter (*pHvU3*), and synthetic single guide RNA (sgRNA); LB and RB represent left and right border sequences of the T-DNA.

(C) Schematic diagram of the T-DNA region of the pMGE634-sgRNAs construct for *SpCas9*-based and Agrobacterium-mediated *HvBICAT3* gene-editing. Construct with same units as the pMGE632-sgRNAs construct, except hygromycin phosphotransferase gene with introns (*hpti*) and *Pisum sativum* rbcS E9 terminator (*tE9*).

One copy of sgRNA1 and sgRNA2, and two copies of sgRNA3 under control of the *H. vulgare* U3 promoter (*pHvU3*) were cloned into each recipient vector as indicated in Figure 32B-C. Vectors were provided by Johannes Stuttmann, who also advised on the genome editing strategy.

4.5 Generation of CRISPR/Cas9-mediated *hvbicat3* mutants

By *Agrobacterium*-mediated transformation of *H. vulgare*, we regenerated a total of 17 plantlets. Seven transgene-free plantlets were identified by PCR of *Cas9* (Figure 33A). PCR-amplified *HvBICAT3* fragments containing the three target sites, obtained with primers residing up- and downstream of these sites, were used to identify mutagenesis in T0 plants (Figure 33B). The amplicons were cloned into a pGEMTeasy vector, and around six clones for each mutant line were sequenced to further examine the mutations. T0 mutants harbored different mutations as presented in Figure 33C. The mutation sites were located from 3 to 18 bp upstream of PAM. Intriguingly, in *hvbicat3_10*, *hvbicat3_13*, *hvbicat3_14*, and *hvbicat3_16* mutants even the PAM was mutated (Figure 33C). The most frequently observed mutation type were deletions, followed by insertions. Base substitutions were detected only in the sgRNA2 target site. While the fragment deletion size at a single target site was up to 25 bp, insertion was only present in one base pair. Fragment deletions of more than 200 bp, created by simultaneous DSBs at two target sites, were also observed in the mutants *hvbicat3_13*, *hvbicat3_14*, and *hvbicat3_16* (Figure 33).

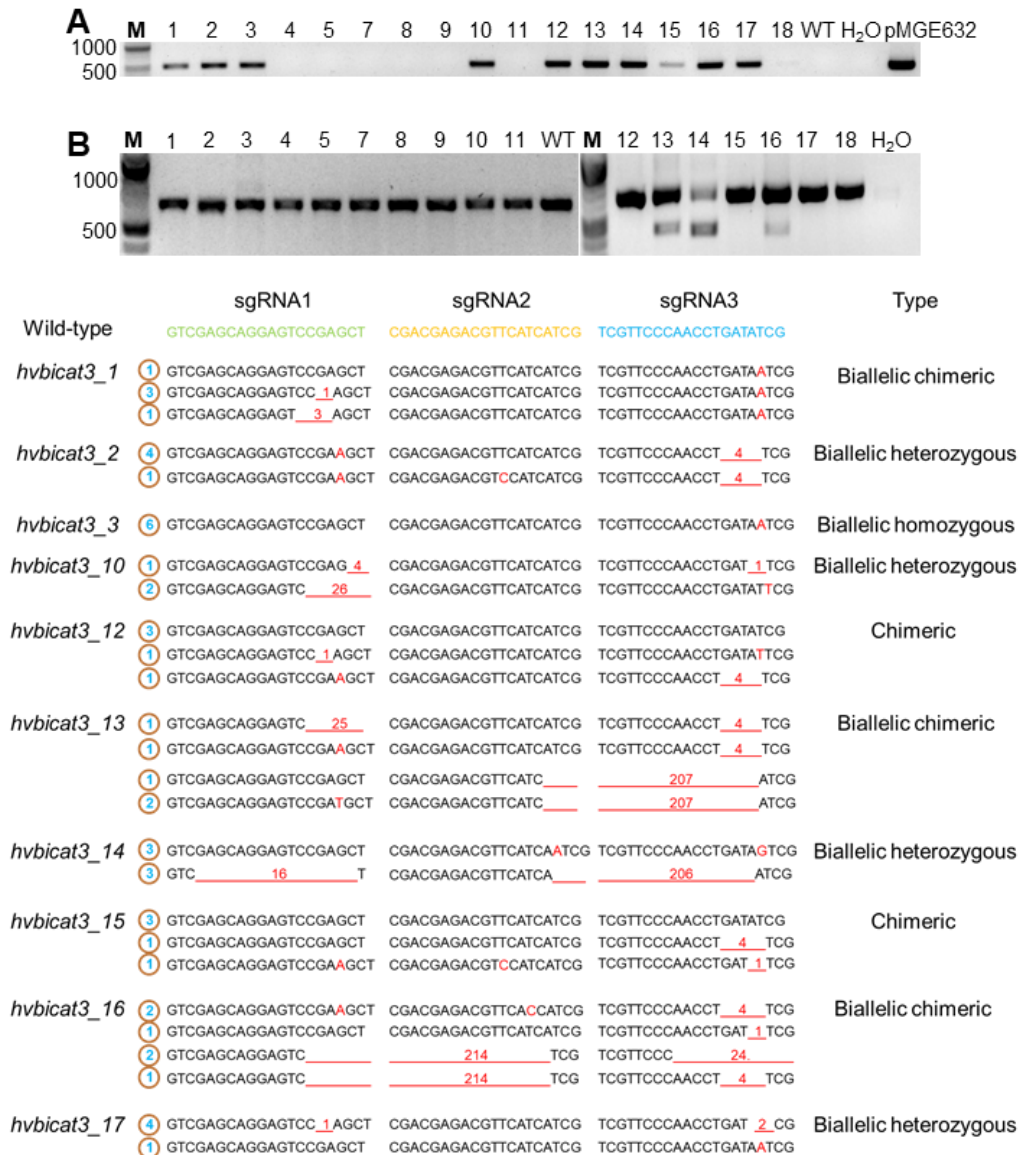


Figure 33. Screening of T0 generation mutants of *HvBICAT3*.

(A) PCR analysis of *Cas9* in T0 plantlets.

(B) PCR analysis of the genomic *HvBICAT3* fragment containing all target regions in T0 plantlets.

(C) Mutation types detected in leaves of T0 mutants revealed by sequencing. Underlined numbers in red indicate the number of nucleotides deleted; red letters indicate small indels; blue numbers in a brown circle indicate the frequencies of the mutation appearing in a single plant.

Altogether, the mutagenic efficiency in T0 generation was 80%, including 20% chimeric mutants (a WT fragment and two mutant fragments), 30% biallelic chimeric mutants (no WT band but more than two mutant fragments), 40% biallelic heterozygous mutants (no WT band but two different mutant fragments) and 10% biallelic homozygous mutants (only one mutant fragment) (Table 1).

Table 1. Frequency of types of T0 generation mutants of *HvBICAT3*.

Type	Lines	Frequency(%)	
Chimeric	Line 12 and 15	20	
Biallic	Biallic chimeric	Line 1, 13 and 16	30
	Biallelic heterozygous	Line 2, 10, 14 and 17	40
	Biallelic homozygous	Line 3	10

The mutation rate at sgRNA2 (50%) was much lower compared to sgRNA1 (90%) and sgRNA3 (100%) among the 12 *hvbicat3* mutants, implying diverse mutagenic efficiency of different target sequences (Table 2).

Table 2. Mutation rate of targets in T0 generation plants.

Target	Lines	Mutation rate(%)
sgRNA1	Line 1, 2, 10, 12, 13, 14, 15, 16 and 17	90
sgRNA2	Line 2, 13, 14, 15 and 16	50
sgRNA3	Line 1, 2, 3, 10, 12, 13, 14, 15, 16 and 17	100

4.6 Selection of transgene-free homozygous *hvbicat3* mutants

T0 mutants were self-pollinated to generate T1 progenies. Seven to eight T1 progenies per T0 line were randomly selected and screened by PCR to generate homozygous *hvbicat3* mutants. Considering that the EcoRV restriction site comprised in sgRNA3 was mutated in all T0 mutants, we harnessed restriction fragment length polymorphism (RFLP) assays by digesting the PCR amplicons of T1 progenies with EcoRV to facilitate screening of biallelic mutants. *hvbicat3_15-6* was detected as WT, *hvbicat3_15-2*, *hvbicat3_15-3* and *hvbicat3_15-4* mutants were confirmed to be chimeric, and all the other T1 progenies were confirmed to be biallelic mutants (Figure 34 and 35).

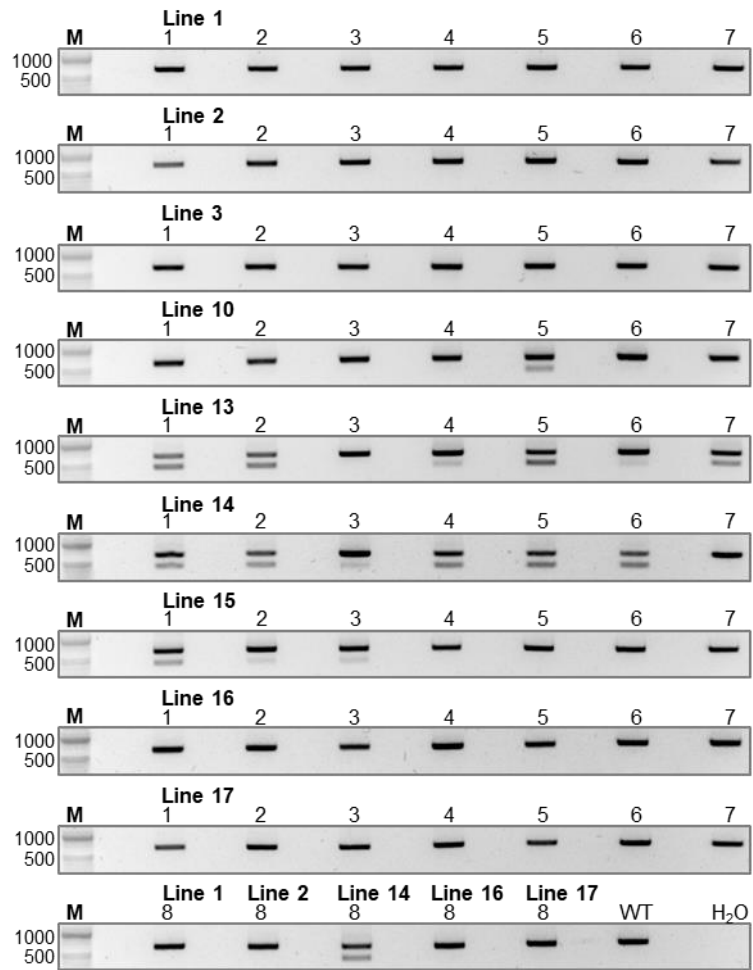


Figure 34. Screening of T1 generation mutants of *HvBICAT3* for large deletions by PCR.

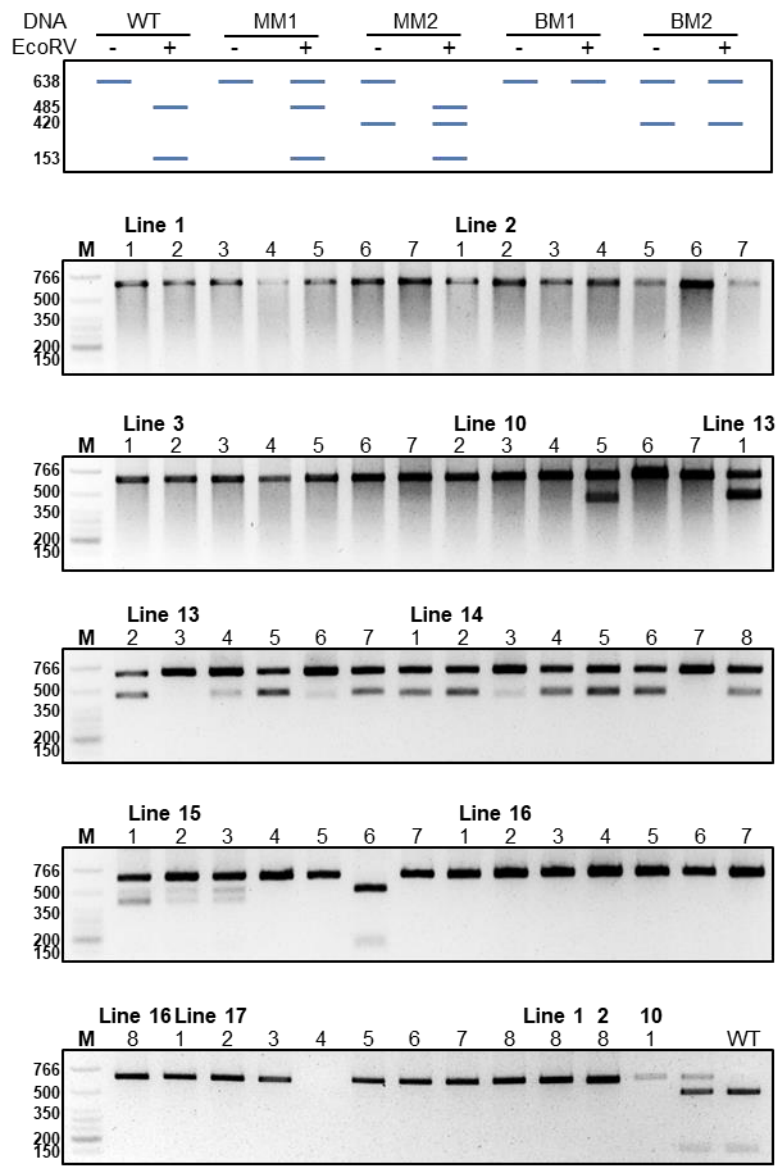


Figure 35. Verification of T1 generation mutants of *HvBICAT3* by EcoRV restriction.

WT, wild type; MM, mono-allelic mutant; BM, biallelic mutant.

Nine out of 68 T1 mutants were tested to be transgene-free by PCR using Cas9 primers (Figure 36).

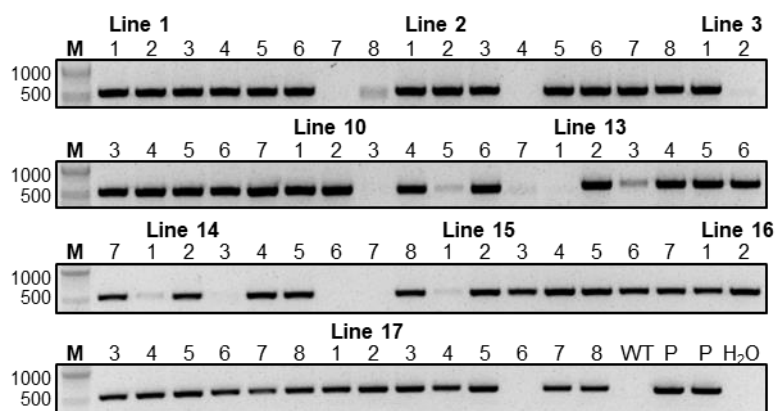


Figure 36. PCR amplification of a Cas9 fragment to screen for transgene-free progenies of T1 generation mutants of *HvBICAT3*.

Similar to T0 mutant screening, PCR amplicons of T1 mutants were cloned into a pGEMTeasy vector, and three clones per mutant line were sequenced. Mutations were heritable in T1 mutants, while novel mutations were also detected in the T1 generation, e.g. in *hvbicat3_13-3* (Figure 37). Some of the T1 progenies derived from different T0 mutant lines showed the same mutation type, e.g. *hvbicat3_1-1* and *hvbicat3_3-4*.

hvbicat3_10-3 and *hvbicat3_14-7* were identified as transgene-free homozygous mutants (Figure 36; Figure 37). *hvbicat3_10-3* harbors a small indel in target 3; *hvbicat3_14-7* carries indels in target 2 and target 3 (Figure 37), both of which resulted in a frame shift mutation (Figure 38).

Wild-type	sgRNA1	sgRNA2	sgRNA3
<i>hvbicat3_1-1</i>	GTCGAGCAGGAGTCCGAGCT	CGACGAGACGTTTCATCATCG	TCGTTCCCAACCTGATAATCG
<i>hvbicat3_3-4</i>	GTCGAGCAGGAGTCCGAGCT	CGACGAGACGTTTCATCATCG	TCGTTCCCAACCTGATAATCG
<i>hvbicat3_3-7</i>	GTCGAGCAGGAGTCCGAGCT	CGACGAGACGTTTCATCATCG	TCGTTCCCAACCTGATAATCG
<i>hvbicat3_2-3</i>	GTCGAGCAGGAGTCCGAAGCT	CGACGAGACGTTTCATCATCG	TCGTTCCCAACCT_4_TCG
<i>hvbicat3_16-8</i>	GTCGAGCAGGAGTCCGAAGCT	CGACGAGACGTTTCATCATCG	TCGTTCCCAACCT_4_TCG
<i>hvbicat3_16-6</i>	GTCGAGCAGGAGTCCGAAGCT	CGACGAGACGTTTCATCATCG	TCGTTCCCAACCT_4_TCG
★ <i>hvbicat3_13-1</i>	GTCGAGCAGGAGTCCGAGCT GTCGAGCAGGAGTCC_2_GCT	CGACGAGACGTTTCATCAATCG CGACGAGACGTTTCATC	TCGTTCCCAACCTGATAATCG 207
<i>hvbicat3_13-5</i>	GTCGAGCAGGAGTCCGAGCT GTCGAGCAGGAGTCC_2_GCT	CGACGAGACGTTTCATCATCG CGACGAGACGTTTCATC	TCGTTCCCAACCTGATAATCG 207
<i>hvbicat3_13-2</i>	GTCGAGCAGGAGTCCGAAGCT GTCGAGCAGGAGTCC_2_GCT	CGACGAGACGTTTCATCAATCG CGACGAGACGTTTCATC	TCGTTCCCAACCT_4_TCG 207
★ <i>hvbicat3_14-5</i>	GTCGAGCAGGAGTCCGAGCT GTC_16_T	CGACGAGACGTTTCATCAATCG CGACGAGACGTTTCATCA	TCGTTCCCAACCTGATAATCG 206
★ <i>hvbicat3_14-6</i>	GTCGAGCAGGAGTCCGAGCT GTC_16_T	CGACGAGACGTTTCATCAATCG CGACGAGACGTTTCATCA	TCGTTCCCAACCTGATAATCG 206
★ <i>hvbicat3_10-1</i>	GTCGAGCAGGAGTCCGAGCT	CGACGAGACGTTTCATCATCG	TCGTTCCCAACCTGATATCG
★ <i>hvbicat3_10-3</i>	GTCGAGCAGGAGTCCGAGCT	CGACGAGACGTTTCATCATCG	TCGTTCCCAACCTGATATCG
<i>hvbicat3_15-5</i>	GTCGAGCAGGAGTCCGAGCT	CGACGAGACGTTTCATCATCG	TCGTTCCCAACCTGATATCG
<i>hvbicat3_15-7</i>	GTCGAGCAGGAGTCCGAGCT	CGACGAGACGTTTCATCATCG	TCGTTCCCAACCTGATATCG
<i>hvbicat3_3-6</i>	GTCGAGCAGGAGTCCGAGCT	CGACGAGACGTTTCATCATCG	TCGTTCCCAACCTGAT_1_TCG
<i>hvbicat3_13-3</i>	GTCGAGCAGGAGTCCGAGCT	CGACGAGACGTTTCATCATCG	TCGTTCCCAACCTGATAATCG
★ <i>hvbicat3_14-7</i>	GTCGAGCAGGAGTCCGAGCT	CGACGAGACGTTTCATCAATCG	TCGTTCCCAACCTGATAATCG
<i>hvbicat3_17-3</i>	GTCGAGCAGGAGTCCGAGCT	CGACGAGACGTTTCATCATCG	TCGTTCCCAACCTGAT_2_CG

Figure 37. Mutations detected in DNA from leaves of some T1 generation *hvbicat3* mutants.

Stars denote transgene-free progenies.

HvBICAT3
Met PRRTLTL LLLALAVSAAGDQFQGAHDGNATTTRRLDRRT
K Met FVHTARGVIGGGDAGVEQESELGLFD AFFASLS Met IL
VSEIGDETFIIAAL Met A Met RHPKSTVLSGALSALVV Met TVLST
GLGRIVPNLISRKHTNSAATVLYAFFGLRLLYIAWRSDSRAS
QNKEIEEVQEKLEAGQGKSTFRRVFSRLCTPIFLESFVTLFL
AEWGDRSQIATIALATHKNAVGV AIGATLGHTICTSFAVVGG
S Met LASRISQGT VATIGLLFLGFSVSSYFYPPL Stop

hvbicat3_10-3
Met PRRTLTL LLLALAVSAAGDQFQGAHDGNATTTRRLDRRT
K Met FVHTARGVIGGGDAGVEQESELGLFD AFFASLS Met IL
VSEIGDETFIIAAL Met A Met RHPKSTVLSGALSALVV Met TVLST
GLGRIVPNLIFEEAH Stop QRSHCP LCILWTP TALHCL EIR
F Stop SITEQGNRRSTGKAGSR SREINI Stop TCFLKV Met YSYFL
GVICVDLPG Stop VG Stop SKSDSHNCAGYAQECCRCCHWSNL
GAHDLHVIRSGGRQHAGVEDIARHC SHHRRPPLRLLCIIIL
LPTIV

hvbicat3_14-7
Met PRRTLTL LLLALAVSAAGDQFQGAHDGNATTTRRLDRRT
K Met FVHTARGVIGGGDAGVEQESELGLFD AFFASLS Met IL
VSEIGDETFINRGSHGDAAPQVDGALRCSVGVGCHDGTINW
AWQDRSQPDSRGSTLTAQPLSF Met HSLDSDCFTLLGDQILE
HHRTRK Stop KKYRKS WKQVKGNQHLDFV SQGYVLLFSWSH
LC Stop PSWLSGVIEVR Stop PQLRWLRTR Met L Stop VLPLEQPW
GTRSARHSQWWAAACWRRGYRKAL Stop PPSEASSS Stop AS
LYHHTSTHHC

Figure 38. SpCas9-induced frame-shift mutations in *HvBICAT3* lead to premature STOP codons and mutated protein sequences.

Letters with red background indicate the predicted *HvBICAT3* open reading frames using the Translate tool (<http://web.expasy.org/translate/>). Blue arrows indicate the modifications of the *HvBICAT3* amino acid sequence.

To further verify their homozygosity, ten T2 progenies from self-pollination were examined by PCR and Sanger sequencing (Figure 39).

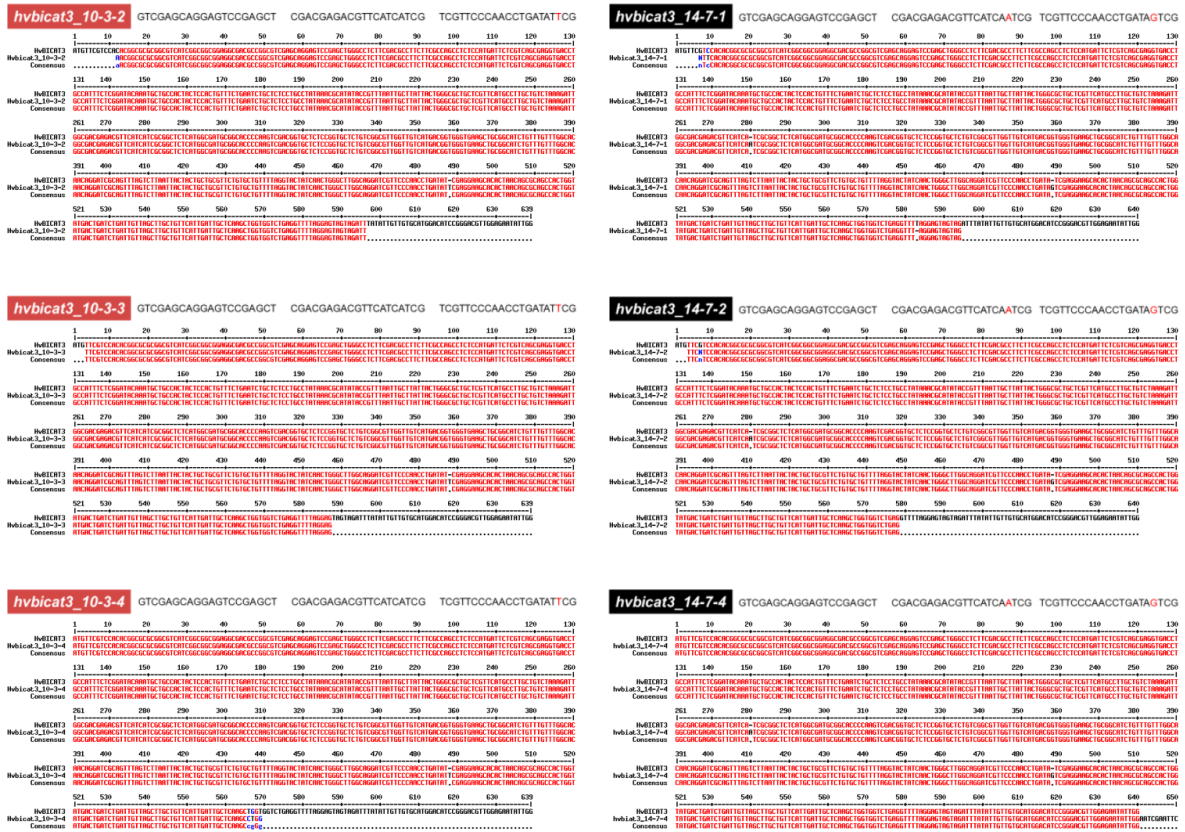


Figure 39. Exemplary sequence alignments of T2 progenies of *hvbicat3_10-3* and *hvbicat3_14-7* mutants.

4.7 The growth of *H. vulgare* is affected by mutation of *HvBICAT3*

The progenies of two homozygous mutants, *hvbicat3_10-3* and *hvbicat3_14-7*, obtained by Cas9-mediated CRISPR, were employed to characterize the roles of *HvBICAT3* in *H. vulgare*. Seed set of both *hvbicat3_10-3* and *hvbicat3_14-7* mutants was not visually different from that of their wild type (Figure 40).



Figure 40. Ears of wild type (WT) and *hvbicat3* mutants.

Scale bar represents 5cm.

The growth of both mutants was retarded compared to wild type under control and Mn^{2+} deficiency conditions (Figure 41A-B). The shoot growth of the *hvbicat3* mutants was suppressed similarly to that of the wild type by the Mn^{2+} deficiency treatment.

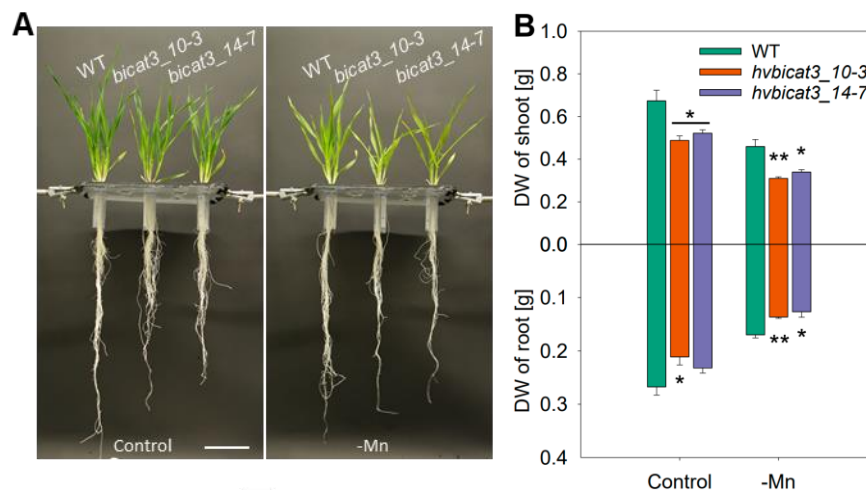


Figure 41. Growth phenotypes of *hvbicat3* mutants and wild type (WT) under control and Mn^{2+} deficiency conditions.

(A) Growth phenotypes of shoot and root of *hvbicat3* mutants. Scale bar represents 10 cm.

(B) Shoot and root dry weight (DW) of *hvbicat3* mutants and wild type. Data indicate means +SE of four biological replicates of wild type and *hvbicat3* mutants. Data were analyzed by two-tailed Student's *t* test to identify significant differences between wild type and mutants (*, $P < 0.05$; **, $P < 0.01$). The experiment was repeated at least twice with similar results.

Leaf shapes of *hvbicat3* mutants and wild type were similar under control conditions (Figure 42). Under Mn^{2+} deficiency, wild-type leaves remained flat, while the young leaves of *hvbicat3* mutants were curled (Figure 42). Newly produced leaves of *hvbicat3* mutants were either surrounded by the older leaves or were not released from the sheaths of older leaves.

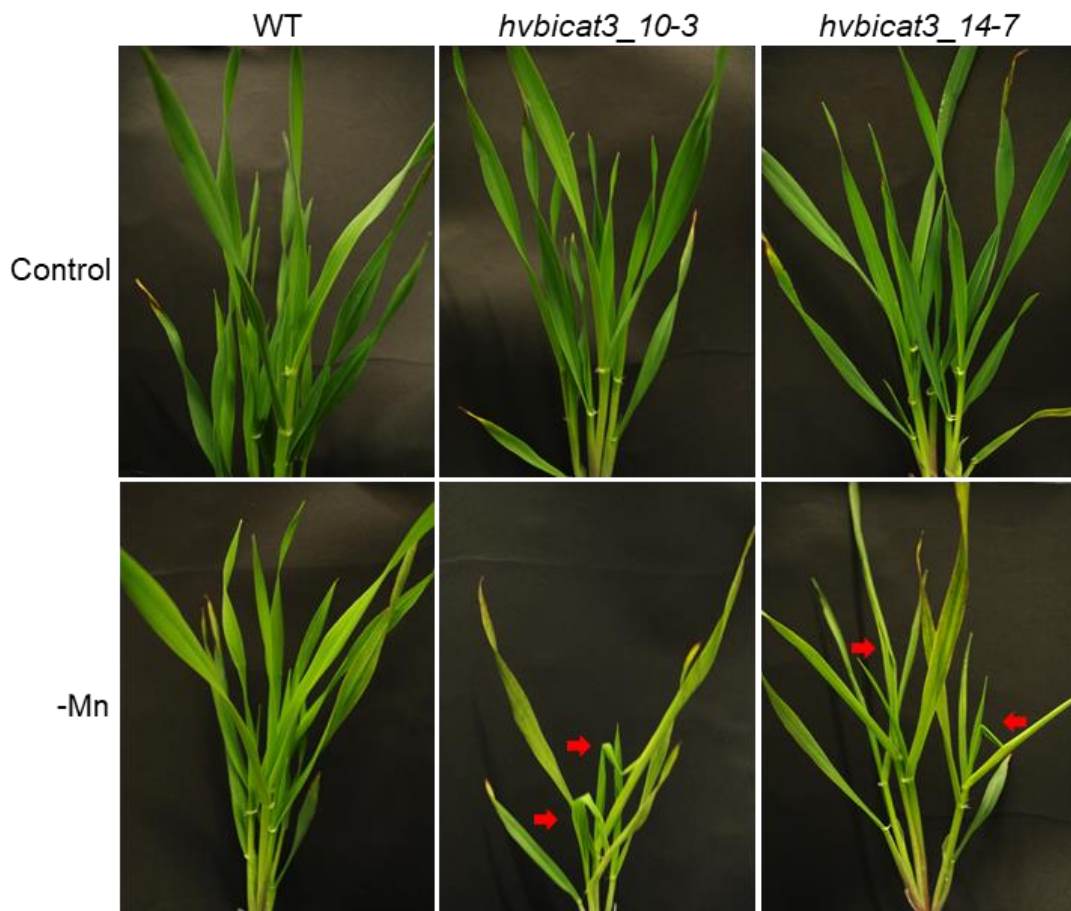


Figure 42. *hvbicat3* mutants produce curly leaves under Mn deficiency.

Interestingly, despite the retarded growth of *hvbicat3* mutants, both lines showed a higher maximum quantum yield of photosystem II (Fv/Fm) and effective quantum yield of photosystem II [Y (II)] in the 2nd youngest leaf (Figure 43A-D). Mn concentrations of the 2nd youngest leaves of *hvbicat3* mutants were slightly higher than that of the wild type under Mn^{2+} deficiency, which was indistinguishable under control conditions (Figure 43E).

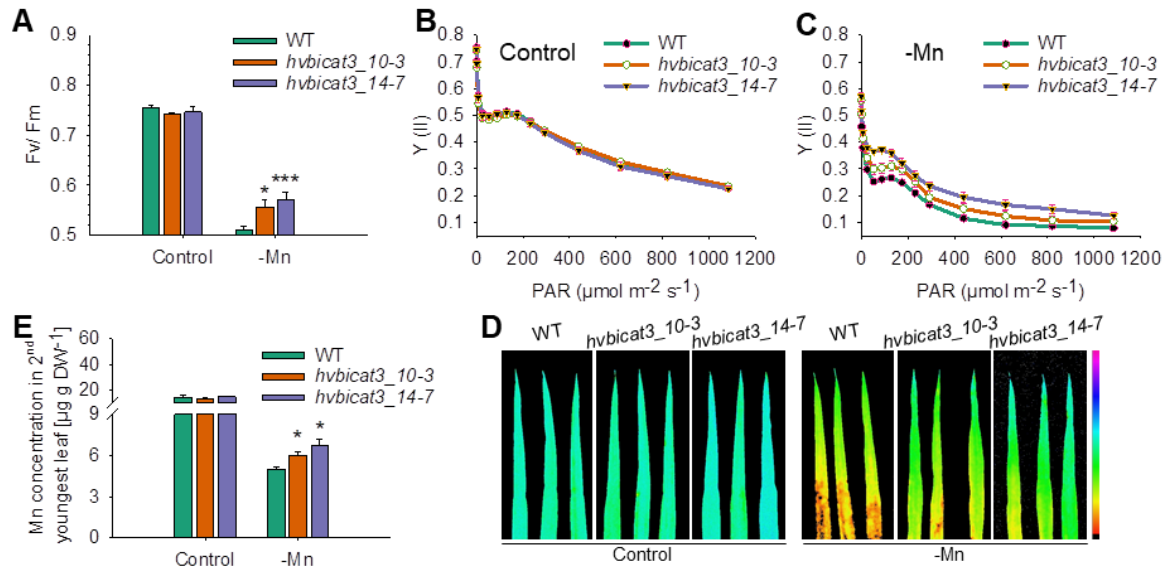


Figure 43. Second youngest leaves of *hvbicat3* mutants contain more Mn and have better photosynthesis compared to wild type (WT) under Mn^{2+} deficiency.

(A) Fv/Fm values of the 2nd youngest leaves of *hvbicat3* mutants and wild type under control and Mn^{2+} deficiency conditions. Data indicate mean +SE of six biological replicates of wild type and *hvbicat3* mutants.

(B) and **(C)** Efficiency of photosystem II (Y (II)) under control and Mn^{2+} deficiency conditions. Data indicate mean \pm SE of six biological replicates of wild type and *hvbicat3* mutants.

(D) Fluorescence images of Y (II) (photosynthetic active radiation, PAR= $175 \mu\text{mol m}^{-2} \text{s}^{-2}$) of the 2nd youngest leaves *hvbicat3* mutants and wild type under control and Mn^{2+} deficiency conditions.

(E) Mn concentration of the 2nd youngest leaves of *hvbicat3* mutants and wild type under control and Mn^{2+} deficiency conditions. Data indicate mean +SE of four biological replicates of wild type and *hvbicat3* mutants.

(A) and **(E)** Data were analyzed by two-tailed Student's *t* test to identify significant differences between wild type and mutants (*, $P < 0.05$; ***, $P < 0.001$).

The experiment was repeated at least twice with similar results.

5 Discussion

Manganese is an indispensable metal for a diversity of processes in plants. One of the essential roles of Mn is as a cofactor of enzymes in the Golgi apparatus that mediate protein glycosylation and polysaccharide biosynthesis (He et al., 2021). Despite the crucial role of Mn in the plant Golgi, little is known about the transport proteins responsible for the Mn supply of Golgi functions. In this work, we found that the ubiquitously expressed *trans*-Golgi-localized BICAT3 protein transports Mn^{2+} and Ca^{2+} in yeast as a heterologous expression system. In the absence of *BICAT3*, *A. thaliana* and *H. vulgare* plants showed numerous aberrances under Mn deficiency, such as growth retardation, changes in leaf morphology, and defects in glycan synthesis, albeit a strikingly better photosynthetic activity was observed. Besides, *A. thaliana bicat3* mutants have a defective pollen tube growth with aberrant pectin accumulation and, ensuing from this, produce shorter siliques with fewer seeds. Thus, BICAT3 plays a vital role in maintaining Golgi functions for both vegetative and reproductive growth of the plant. The biochemical phenotypes of BICAT3 revealed in this work point to a direct involvement in Mn^{2+} homeostasis, whereby additional roles for Ca^{2+} -dependent processes cannot be excluded and may also underlie some macroscopic phenotypes.

5.1 Functions of *BICAT3* and *HvBICAT3* in yeast

Heterologous expression of *BICAT3* in yeast mutants that are sensitive to different metals showed that BICAT3 restored the Ca^{2+} and Mn^{2+} tolerance of *pmr1Δ gdt1Δ* and *pmr1Δ* yeast mutants, respectively (Figures 7, 8). Interestingly, *pmr1Δ gdt1Δ-BICAT3* grew comparably to the *pmr1Δ* single mutant under 600 mM $CaCl_2$, indicating the functional conservation of BICAT3 and GDT1. These data suggest that BICAT3 is specifically involved in Ca^{2+} and Mn^{2+} transport when heterologously expressed in yeast.

Heterologous expression of *HvBICAT3* fully counteracted the growth defects of the *pmr1Δ gdt1Δ* under Ca^{2+} toxicity and slightly restored the growth of the *pmr1Δ* yeast mutant under Mn^{2+} toxicity (Figure 31), indicating a similar role of *HvBICAT3* in Ca^{2+} and Mn^{2+} transport when heterologously expressed in yeast. Although *BICAT3* and *HvBICAT3* are highly conserved in their TMDs, they are different in the N-terminal peptide region (Figure 29B). Whether this leads to a different subcellular localization and regulation of their activities in yeast, which in turn affects the recovery of the *pmr1Δ* yeast mutant growth under Mn^{2+} toxicity by the expression of *BICAT3* and *HvBICAT3* remains to be tested. Studying the subcellular localization and testing the growth phenotype of yeast mutants expressing N-terminus-truncated versions of *BICAT3* and *HvBICAT3* would help to address this question.

Incomplete selectivity between Ca^{2+} and Mn^{2+} is characteristic for transport proteins belonging to numerous families. In plants, these include ER-type Ca^{2+} -ATPases [e.g., *ECA1* (Wu et al., 2002) and *ECA3* (Li et al., 2008; Mills et al., 2008)], Calcium Exchangers [e.g., *CAX2* (Shigaki et al., 2003)], as well as *BICAT* proteins, for which transport of Ca^{2+} and Mn^{2+} has directly been demonstrated in *BICAT1* and *2* (Schneider et al., 2016; Wang et al., 2016; Frank et al., 2019). The physiological relevance of the dual functionality is largely unresolved, and it is unclear how homeostasis of both elements is regulated independently by non-discriminating transporters (He et al., 2021). In this respect, it is interesting to note that the ability of the animal Mitochondrial Ca^{2+} Uniporter (MCU) to discriminate between Ca^{2+} and Mn^{2+} is conferred by a Ca^{2+} -sensing accessory subunit, *MICU1* (Kamer et al., 2018). Whether a similar mechanism exists to tune their Ca^{2+} -vs.- Mn^{2+} selectivity operates in *BICAT* proteins remains to be tested.

5.2 BICAT3 is essential for Ca²⁺/Mn²⁺ homeostasis in plants, especially the resistance to Mn²⁺ deficiency

Both young (2-week-old) and older (6-week-old) plants of *bicat3* loss-of-function *A. thaliana* mutants showed altered responses to different Ca²⁺ and Mn²⁺ supply levels compared to the wild type. In conditions of Mn²⁺ deficiency and Ca²⁺ toxicity, *bicat3* mutants performed worse than the wild type, while they responded superiorly to Mn²⁺ toxicity and Ca²⁺ deficiency (Figures 10 to 13). The most striking growth difference between *bicat3* mutants and the wild type was found under Mn²⁺ starvation. Collectively, these results indicate a role of BICAT3 in Mn²⁺ and Ca²⁺ homeostasis of Arabidopsis, in particular during low Mn²⁺ availability. It remains to be clarified if the altered response of *bicat3* mutants to extreme Ca²⁺ supply is due to a Ca²⁺ transport activity of the transporter, or due to the Mn²⁺-vs.-Ca²⁺ selectivity of the processes that back up BICAT3. In mammalian cells, Mn²⁺-mediated rescue of glycosylation defects inflicted by deletion of the BICAT3 homolog, TMEM165, is likely dependent on ER-resident SERCA-type ATPases, indicating the ER potentially contributes to the supply of Mn²⁺ to the Golgi (Houdou et al., 2019). In contrast, the Golgi-localized SPCA1 Ca/Mn-ATPase did apparently not contribute to the rescue of Mn²⁺-dependent glycosylation in *tmem165* mutants (Houdou et al., 2019). It is unresolved whether the normal vegetative growth and glycosylation pattern of *bicat3* mutants under control conditions are due to other Golgi-localized Mn²⁺ transport proteins or a supply via vesicular trafficking from the ER. In this respect, it is interesting to note that knockout mutants of MTP11, a Mn²⁺ transporter that also localizes to the *trans*-Golgi, show a phenotype that is opposite to that of *bicat3* mutants: They are hypersensitive to Mn²⁺ toxicity and hypertolerant to Mn²⁺ deficiency (Peiter et al., 2007). It remains to be established how both transporters, believed to accumulate Mn²⁺ into the same compartment, apparently take in opposite roles. Explanations may lie in different expression patterns, as evident from *in silico* analyses of transcriptome data

(www.genevestigator.com), or in different subcompartmental localizations, as discussed below.

bicat3 mutants were more tolerant to Mn^{2+} toxicity in both plate and hydroponic cultures under long-day and short-day conditions, represented by a higher shoot and root biomass than that of the wild type (Figures 12 and 13). Interestingly, *bicat3* shoots accumulated less Mn^{2+} compared to those of the wild type under elevated Mn^{2+} conditions, which likely explains the better growth of *bicat3* under Mn^{2+} toxicity. In contrast to our results, Yang et al. (2021) reported a *higher* sensitivity of *bicat3* (*pml3*) mutants to Mn^{2+} toxicity compared to the wild type. These findings are difficult to reconcile with our study and might be due to different media (nutrient composition and concentration), growth conditions (light cycle and light intensity) or plant age.

5.3 BICAT3 restricts manganese bioavailability for chloroplasts

Intriguingly, although growth of *bicat3* mutants suffered substantially under Mn^{2+} deficiency, photosynthetic activities of the mutants were superior to those of the wild type (Figure 15). This coincided with moderately higher Mn concentrations in shoots of the mutants than in those of the wild type (Figure 13). Grafting experiments revealed that improved photosynthesis and the morphological phenotype of *bicat3-1* were both caused by the loss of BICAT3 in the shoot (Figure 17). Since the photosynthetic light reaction is highly sensitive to Mn^{2+} deficiency (Alejandro et al., 2020), we assumed that the intracellular allocation of Mn^{2+} to chloroplasts may be altered in *bicat3* mutants. Indeed, under Mn^{2+} deficiency *bicat3* chloroplasts accumulated more Mn^{2+} than those of the wild type, rendering the Mn^{2+} limitation less severe (Figure 15). This indicates that BICAT3 is able to govern the competition of different cellular compartments for Mn^{2+} . It currently cannot be discerned whether Mn^{2+} supply of other organelles is also improved in the absence of BICAT3.

Interestingly, the TGN-localized transporter NRAMP2, in conjunction with the vacuolar transporters NRAMP3 and 4, has previously been proposed to have a role in inter-organellar Mn²⁺ distribution towards chloroplasts under Mn²⁺-limiting conditions. This appears to be supported by decreased or increased chloroplast Mn concentrations in *NRAMP2* knockdown and overexpression plants, respectively (Alejandro et al., 2017). However, since expression of *NRAMP2*, 3, and 4 in leaves is strictly confined to the vascular system (Thomine et al., 2003; Alejandro et al., 2017), the operation of an NRAMP2-driven Mn²⁺ supply chain of chloroplasts and a possible interference of BICAT3 with this process demands further scrutiny.

5.4 BICAT3 determines matrix polysaccharide biosynthesis

BICAT3 operates as a Golgi-localized Mn²⁺ transporter, and the biosynthesis of the cell wall matrix polysaccharides, pectin and hemicellulose, is mediated by Golgi-localized glycosyl transferases, many of which require Mn²⁺ (He et al., 2021). We therefore hypothesized that the prominent aberrations in leaf shape and cell size and morphology of Mn²⁺-deficient *bicat3* mutants (Figures 13 and 18) are related to an altered cell wall matrix. This notion was strongly supported by a combined analysis of monosaccharide and linkage abundance (Figure 19). The abundance of xyloglucan was decreased in the shoot cell wall of both *bicat3* mutant lines, as evident from a declined proportion of Xyl and 4-Glc. Xyloglucans are the most abundant hemicellulose in the primary cell wall of eudicots and essential for maintaining cell wall extensibility (Park and Cosgrove, 2015; Gigli-Bisceglia et al., 2020). Immunolocalization analyses indicate the first appearance of xyloglucans in *trans* cisternae (Zhang and Staehelin, 1992), which corresponds to the localization of BICAT3 (Figure 4). Xyloglucan biosynthesis in the Golgi is mediated by two xyloglucan xylosyltransferases, XXT1 and XXT2, that are coordinated with Mn²⁺ (Culbertson et al., 2016; Culbertson et al., 2018). Cell

extension induced by α -expansins is diminished in *xxt1xxt2* double mutant walls which lack detectable xyloglucans, indicating an essential role of xyloglucans in cell wall loosening (Park and Cosgrove, 2012), that may underlie the reduced cell size, circumference, and perimetric inequality in *bicat3* mutants (Figure 18). This notion is supported by the smaller size of *xxt1xxt2* shoots (Park and Cosgrove, 2012).

A reduction in the abundance of GalA indicated that the overall pectin content was also lower in shoot cell walls of Mn^{2+} -deficient *bicat3* mutants as compared to those of the wild type (Figure 19). Additionally, the abundance of Rha and the 2-Rha linkage was increased, while that of Gal and the 4-Gal linkage was severely decreased. These aberrances indicate that the galactan side chain substitution of Rhamnogalacturonan I (RG I) was affected in *bicat3* shoot cell walls [Figure 1; He et al. (2021)], a reaction that also occurs in the *trans* cisternae of the Golgi (Zhang and Staehelin, 1992). In Arabidopsis, this addition of galactose from UDP- α -D-Gal to growing β -1,4-galactan chains is catalyzed by the highly Mn^{2+} -dependent galactan synthases (GALS1 to 3) (Ebert et al., 2018; Laursen et al., 2018). Along with xyloglucans, galactan domains of RG I interact with cellulose microfibrils, hence maintaining cell wall structure (Zykwinska et al., 2007). A truncation of galactan side chains also interferes with porosity and thus water-binding capability of the plant cell walls (Klaassen and Trindade, 2020). However, a mutant lacking all *GALS* genes did not display a macroscopic phenotype (Ebert et al., 2018), which suggests that diminished RG I side chains did not cause the growth reduction in Mn^{2+} -deficient *bicat3* mutants.

By association with Receptor-Like Proteins (RLP) or Wall-Associated Kinases (WAK), pectins not only modulate the extensibility, flexibility, and rigidity of the cell wall, but are also involved in feedback regulation to control cell wall homeostasis during cell expansion (Kohorn and Kohorn, 2012; Franck et al., 2018). RLP44 is critical for transmission of information about changes in pectin by interacting with the Brassinosteroid Insensitive 1 (BRI1) Associated receptor

Kinase 1 (BAK1) through brassinosteroid (BR) signaling. The association between RLP44 and BRI1 is also involved in procambial cell fate controlling (Holzwardt et al., 2020).

The plasma membrane-localized CrRLK1L (Catharanthus roseus Receptor Like Kinase 1-Like, also known as malectin-like receptor kinases) protein FERONIA (FER) plays an essential role in many aspects of plant growth and development, e.g. cell wall integrity maintenance, cellular growth, plant reproduction, plant immunity, hormone signaling, and abiotic stress tolerance (Franck et al., 2018; Duan et al., 2020; Gigli-Bisceglia et al., 2020). Feng et al. (2018) proposed that FER senses the salt stress-induced interruption of pectin cross-linking and subsequently induces Ca^{2+} signaling to trigger cell wall repair mechanisms. Although FER directly interacts with pectin *in vitro* (Feng et al., 2018), this interaction has not been shown *in vivo* yet. Instead of direct links between FER and cell wall sugars, the interaction between FER and Leucine-rich repeat extensins (LRXs) might function as a bridge between the cell wall and plasma membrane to facilitate cell wall sensing, to convert the extracellular signal to intracellular signaling, and in turn, to modulate the expansion of the vacuole and cellular expansion (Dünser et al., 2019).

WAKs are essential for cell expansion and pathogen resistance (Kohorn and Kohorn, 2012). WAK2 binds to pectin in the cell wall, and *WAK2* antisense plants show small and curly-bent leaf phenotypes, with smaller cell size (Wagner and Kohorn, 2001). The curled-leaf phenotype of *bicat3* might thus be related to signalling pathways induced by the defects in pectin biosynthesis under Mn^{2+} deficiency.

The abundance of callose was drastically increased in cell wall of *bicat3* mutants (Figure 20), which coincided with a higher abundance of Glc and 3-Glc linkage (Figure 19). Callose is not synthesized in the Golgi, but by callose synthases at the plasma membrane. Hence, callose deposition in *bicat3* mutants likely is a response to the aberrations inflicted by the absence of BICAT3. Callose

deposits play multiple roles in plants, in particular in the regulation of plasmodesmata and in responses to biotic and abiotic stresses (De Storme and Geelen, 2014; Rissel et al., 2017; Hunter et al., 2019; Wang et al., 2021). Recently, callose synthesis was reported to be induced by Ca^{2+} deficiency, preventing cell death (Shikanai et al., 2020). Due to its function in cross-linking pectins, Ca^{2+} deficiency is believed to induce cell wall damage that is counteracted by callose depositions. In support of this, expression of a cell wall damage-induced transcription factor, OsWRKY42, in Arabidopsis leads to intensified callose accumulation (Pillai et al., 2018). We therefore hypothesize that the abnormal accumulation of callose in *bicat3* mutants is a result of cell wall defect-induced signalling pathways under Mn^{2+} deficiency.

Apart from the specific changes in cell wall polymers, we observed an altered *N*-glycosylation pattern in Mn^{2+} -deficient *bicat3* by ConA-staining of total protein (Figure 21). The appearance of additional bands suspiciously resembles mutants in the Golgi-localized ER- and Golgi- α -mannosidase I (MNS1/2/3) (Liebminger et al., 2009), which are Mn^{2+} -dependent deglycosidases essential in the synthesis of complex *N*-glycan structures (Figure 1). These mutants display severe growth defects (Liebminger et al., 2009), and a defect in the function of those Mn^{2+} -dependent proteins may also underlie the phenotype of *bicat3*. It remains to be analyzed which steps in *N*-glycosylation and which glycoproteins are affected in the *bicat3* mutant.

Taken together, under limited Mn^{2+} supply, the loss of *BICAT3* causes multiple direct and indirect changes in cell wall polysaccharide and glycoprotein biosynthesis. It remains to be determined whether the observed macroscopic phenotypes are a direct result of those alterations.

5.5 BICAT3 determines pollen tube growth and seed set in Arabidopsis

Apart from their drastic vegetative phenotype under Mn^{2+} deficiency, *bicat3* mutants were severely affected in reproduction, producing fewer but larger seeds in shorter siliques (Figures 23 and 24). As evident from reciprocal crossing, this reduced fertility was caused by a defect in the male gametophyte. Pollen tubes of *bicat3* mutants showed highly heterogeneous morphologies and were often branched or swollen (Figures 27 and 28).

We hypothesized that the defective pollen tube growth was caused by a Mn^{2+} -dependent function of the Golgi. Elongation of the pollen tube requires the deposition of cell wall material at the tip. The most abundant pectin, homogalacturonan (HG) is synthesized in the Golgi by HG synthetases of the GAUT family (Atmodjo et al., 2011). These proteins contain a Mn^{2+} -binding DXD motif, and for the GAUT1:GAUT7 enzyme complex an absolute dependence on Mn^{2+} has been experimentally shown (Amos et al., 2018). Numerous GAUT genes are expressed in pollen, most prominently *GAUT13* and *14*. Pollen tubes of the *gaut13gaut14* mutant are swollen and defective in tube growth (Wang et al., 2013), similar, but more severely, as observed in *bicat3* mutants. Also mutants of the functionally redundant *GAUT5*, *6*, and *7*, that are more weakly expressed in pollen, were defective in tube elongation (Lund et al., 2020). In those GAUT mutants, HGs are unconventionally distributed, with weakly esterified HG, detected by the JIM5 antibody, being severely reduced in the *gaut13gaut14* mutant (Wang et al., 2013). This defect closely resembles our observations in *bicat3* mutants. The abundance of weakly esterified HG in sub-apical regions was severely diminished in *bicat3*, which most likely led to a loss in rigidity and hence in a swelling of the otherwise perfectly cylindrical tube. The pattern of pectin deposition and the tube morphology showed substantial variability in the *bicat3* mutant, which may be related to varying Mn^{2+} resources in the pollen population, affecting Mn^{2+} -dependent processes to different degrees. This is also evident from *in vivo* and *semi in vitro* assays, where some pollen tubes extended sufficiently to reach an ovule. However, the abnormal

swelling was always associated with a decreased HG abundance. In some instances, *bicat3* pollen formed cylindrical, less severely affected, tubes with higher abundance of weakly esterified HG. In agreement with previous analysis, the deposition of weakly esterified HG was weaker at the very tip of the wild type tube, which enables a higher expandability of this region (Chebli et al., 2012). However, this pattern was rather variable, which has also been described before, likely reflecting variation in growth velocity (Stepka et al., 2000). The pattern of HG deposition in *bicat3* is in disagreement with a recent report by Zhang et al. (2021), who claim an *increased* deposition of weakly methylesterified HG at the tip of *bicat3*, with no change in sub-apical regions. This pattern is difficult to reconcile with the morphological changes, and it does not reflect or correspond with the morphological variability of *bicat3* pollen tubes.

Despite the close match of aberrant HG deposition and growth defects, a contribution of other Mn^{2+} -dependent processes to the phenotype cannot be excluded. Golgi-localized enzymes involved in the synthesis of further cell wall polysaccharides and glycoproteins may also be affected. For example, MGP4, involved in RG-II biosynthesis (Liu et al., 2011), GALT2-6 and HPGT1-3 involved in AGP biosynthesis (Basu et al., 2015; Basu et al., 2015; Ogawa-Ohnishi and Matsubayashi, 2015), and HPAT1-3 involved in extensin biosynthesis (Ogawa-Ohnishi et al., 2013), all show pollen tube growth defects, and any contribution of these proteins to the *bicat3* phenotypes remains to be demonstrated.

5.6 Functional similarities and diversities of BICAT3 and HvBICAT3

To analyze whether the roles BICAT3 are conserved across the plant kingdom, a functional characterization of its homolog in *H. vulgare* was initiated. Although BICAT3 and HvBICAT3 are diverse in their N-terminal peptide region, they were both localized in the Golgi apparatus (Figure 4 and 30). Under Mn^{2+} deficiency, both *bicat3* and *hvbicat3* mutants show retarded growth and curly-leaf

phenotypes, but better photosynthetic activities compared to wild type plants (Figures 13-15, 40-42), indicating a similar Mn^{2+} transport activity of BICAT3 and HvBICAT3. Whether a similar subcellular Mn^{2+} translocation strategy under Mn^{2+} deficiency exists in *A. thaliana* and *H. vulgare* when BICAT3 and HvBICAT3 are mutated, must be tested by measuring the Mn content of *H. vulgare* chloroplasts.

On the other hand, *hvbicat3* mutants showed repressed growth under control conditions compared to the wild type, while *bicat3* mutants grew similarly to Col-0 (Figure 14 and 40), implying the mutation of BICAT3 and HvBICAT3 influences the growth of *A. thaliana* and *H. vulgare* to a different extent. The diverse development of *bicat3* and *hvbicat3* mutants might be due to at least two reasons. First, the cell wall composition of dicots (*A. thaliana*), and monocots (*H. vulgare*) is quite different (Mohnen, 2008). For instance, pectin contents are lower, and heteroxylan contents higher, in the primary wall of monocots. Perhaps the enzymes for synthesizing major components of the *H. vulgare* cell wall matrix have higher Mn^{2+} requirements, rendering *H. vulgare* more sensitive to changes in Golgi Mn^{2+} homeostasis resulting from the mutation of HvBICAT3. Another possibility is that HvBICAT3 has a more prominent role in regulating Golgi Mn^{2+} homeostasis than BICAT3 due to a different set of transporters involved. For example, possible ECA3 homologs have not been investigated in barley yet. Hence, our understanding of the role of Golgi-localized Mn^{2+} transporters and the functional interaction of their activity is rather rudimentary in Arabidopsis and even more so in barley. Decrypting the function and interaction of BICAT3s and the other Golgi-localized Mn^{2+} transporters in different species will help us to better understand the machinery that regulates Mn^{2+} homeostasis in the Golgi.

A. thaliana bicat3 mutants displayed a strongly diminished seed production compared to Col-0, which was due to a defective pollen tube growth (Figure 23, 25, 26). In contrast, no noticeable difference was observed in ears of *hvbicat3* mutants compared to wild type (Figure 40), albeit a quantification of yield parameters still needs to be performed. Diverging cell wall composition of

monocotyledonous and dicotyledonous pollen tubes might account for the different impact of *bicat3/hvbicat3* mutation on fertility and seed set in *A. thaliana* and *H. vulgare*. In addition, the pistil architecture of *A. thaliana* and *H. vulgare* is quite different, as shown in Johnson et al. (2019). The *A. thaliana* pistil has a dry stigma with multicellular papillae and multiple ovules, while *H. vulgare* has a dry plumose stigma and single ovules. It is conceivable that the fertilization procedure in *A. thaliana* and *H. vulgare* might be different. Moreover, the expression of transporters in *A. thaliana* and *H. vulgare* gametophytes might be different, and other Mn^{2+} transporters operating alongside HvBICAT3 may be sufficient to supply the Golgi with Mn^{2+} for barley pollen tube growth.

To better understand the role and relevance of *HvBICAT3* in barley, its expression pattern needs to be analyzed, as well as agronomic traits (e.g., tiller number, grain yield, spike number, seed weight) and the cell wall sugar composition and linkage of *hvbicat3* mutants under control and Mn^{2+} -deficient conditions.

5.7 Efficient targeted mutagenesis of the *HvBICAT3* gene in *H. vulgare* via CRISPR/Cas9-mediated genome editing

CRISPR/Cas9-mediated genome editing of *H. vulgare* has been employed in numerous reports with primary editing efficiencies ranging from 4.7% to 78% (Lawrenson et al., 2015; Holme et al., 2017; Kapusi et al., 2017; Gasparis et al., 2018; Kumar et al., 2018; Garcia-Gimenez et al., 2020; Gerasimova et al., 2020; Vlcko and Ohnoutkova, 2020; Yang et al., 2020; Zeng et al., 2020; Lee et al., 2021). In our study, the mutagenesis efficiency of Cas9-carrying T0 plantlets was 100% (Table 1), which is much higher than that reported in most former studies. The probability that the sgRNA is effective was enhanced by duplicating an sgRNA and by employing three sgRNAs targeting different sites of the gene, which has not been pursued before. Biallelic mutations were detected already in the T0

generation, accounting for 80% (8 out of 10) of the T0 mutants. This biallelic mutation rate is also higher than that reported in former studies, i.e. 57% (4 out of 7 T0 mutants) in Vlcko and Ohnoutkova (2020). T1 progenies generated by self-pollination of biallelic T0 mutants were 100% biallelic mutants (Figure 35), which indicates that the mutations are heritable. However, some of the mutations were not transmitted to the T1 generation (Figures 33, 37). It is possible that these types of mutations occurred only in somatic cells, but not in germline cells. Similar activities have been shown by Zeng et al. (2020) and Kapusi et al. (2017). On the other hand, new mutagenesis events were detectable in the T1 generation (Figure 39). These may be either generated by new genome editing events due to the presence of Cas9 or by the limitation of screening mutants by a single leaf, whereby mutations in chimeric plants may go unnoticed, as discussed in Zeng et al. (2020). The inheritance of mutations in chimeric lines may follow unpredictable patterns, which was exemplified in *hvbicat3_15*, a chimeric mutant carrying a *HvBICAT3* wild-type allele (Figure 33). Both biallelic mutations and the wild-type allele were again detected in the T1 progenies of this line (Figure 35). Interestingly, some T1 offsprings of *hvbicat3_15* were still chimeric, which might be due to the existence of Cas9 and still active genetic modification in the somatic cells.

Three sgRNAs were utilized in parallel in our study to increase the genetic modification rate and to achieve chromosomal fragment deletion in order to simplify the screening procedure by amplified fragment length polymorphism (AMP-FLP) assays. Although feasible, this approach was not very successful in our hands (Figure 33 and 37). The three target sites differed in mutation efficiency (Table 2), which might relate to different properties of them. The higher mutation rate of the sgRNA3 target may have also been caused by a stronger expression of sgRNA3 due to its duplication in the genetic modification constructs.

Since the segregation of the T-DNA insertion and the mutations generated by CRISPR/Cas9-mediated genome editing are independent, it is possible to obtain T-DNA-free homozygous mutants in offspring of CRISPR/Cas9-generated

mutants. In this work, we successfully generated two transgene-free mutants carrying small indels in the T1 generation. Taken together, this work demonstrates the high efficiency of CRISPR-Cas9-mediated genome editing to generate targeted mutations that allow the functional characterization of genes in *H. vulgare*.

6 Conclusions

- BICAT3 localizes to the *trans*-Golgi and is ubiquitously expressed in most tissues.
- BICAT3 complements the growth defects of *pmr1Δ gdt1Δ* and *pmr1Δ* under Ca^{2+} toxicity and Mn^{2+} toxicity, respectively, indicating that it acts as a Ca^{2+} and Mn^{2+} transporter in yeast.
- BICAT3 plays a pivotal role in Mn^{2+} and Ca^{2+} homeostasis of Arabidopsis, in particular during low Mn^{2+} availability, and it determines the responses of plants to varying Mn^{2+} and Ca^{2+} supply.
- BICAT3 determines the subcellular allocation of Mn^{2+} between Golgi and chloroplast. The improved photosynthesis and morphological phenotype of *bicat3-1* under Mn^{2+} deficiency are both caused by the loss of BICAT3 in the shoot, while the moderately higher Ca^{2+} concentration of *bicat3-1* is determined by the root.
- BICAT3 impacts on matrix polysaccharide (i.e., xyloglucan and pectin) biosynthesis and protein *N*-glycosylation pattern under Mn^{2+} -insufficient conditions.
- BICAT3 modifies the accumulation and deposition of low methyl-esterified homogalacturonan in pollen tubes, which in turn affects the pollen tube growth and seed set.
- HvBICAT3 is the closest ortholog of BICAT3 in barley, localizes to the Golgi, and acts as transporter for Ca^{2+} and possibly Mn^{2+} in yeast.
- HvBICAT3 is functionally similar to BICAT3 in affecting Mn concentrations of the plant. *hvbicat3* shows similarly improved photosynthesis and morphological changes in leaves.
- BICAT3 and HvBICAT3 may have different physiological roles in plant development, as indicated in the differences in the growth of mutants under control conditions and in seed production.

7 Summary

Manganese is an indispensable metal for a diversity of processes in plants. One of the most essential roles of Mn^{2+} is as a cofactor of enzymes in the Golgi apparatus which mediate protein glycosylation and polysaccharide biosynthesis. Despite the crucial role of Mn^{2+} in the plant Golgi, little is known about the transport proteins responsible for the Mn^{2+} supply to the Golgi to date.

In this work, it was found that the ubiquitously expressed *trans*-Golgi-localized BICAT3 protein transports Mn^{2+} and Ca^{2+} in a heterologous expression system. In the absence of *BICAT3*, plants showed numerous aberrances under Mn^{2+} deficiency, such as growth retardation, changes in rosette leaf morphology, and defects in glycan synthesis, albeit a strikingly better photosynthetic activity was observed, which correlated with an increased chloroplastic Mn^{2+} concentration. BICAT3 functions are specific to roots and shoots, as determined in reciprocal grafting experiments. Besides, *bicat3* mutants have a defective pollen tube growth with aberrant pectin accumulation and, ensuing from this, produce shorter siliques with fewer seeds. Thus, BICAT3 plays a vital role in maintaining Golgi functions for both vegetative and reproductive growth of the plant.

Similarly, HvBICAT3, a close ortholog of BICAT3 in *H. vulgare*, is also localized in the Golgi apparatus and transports Mn^{2+} and Ca^{2+} in a heterologous expression system. Transgene-free barley mutants of *HvBICAT3* generated by taking advantage of a CRISPR/Cas9-mediated genome editing system showed retarded growth. In addition, *hvbicat3* mutants change in leaf morphology under Mn^{2+} deficiency, albeit a remarkably better photosynthetic activity was observed. A strong reduction in seed set was not apparent in *hvbicat3* mutants. The findings suggest that HvBICAT3 is similar to BICAT3 in supporting Golgi functions for the growth of plants under Mn^{2+} limitation. Nevertheless, BICAT3 and HvBICAT3 may have different physiological roles during plant development, as indicated in the differences in the growth of mutants under control conditions and in reproduction.

8 Appendix

8.1 List of primers

All primers were obtained from Eurofins Genomics, Ebersberg, Germany. The design of the primers was performed with the help of the online tools NetPrimer (premierbiosoft.com/netprimer/) and AMUSER 1.0 (<http://www.cbs.dtu.dk/services/AMUSER/>).

Table 3. List of primers used in this study.

Number	Name	Sequence 5'- 3'	Purpose
PEO1453	T-DNA <i>bicat3-1_F</i>	TTGATATCGAGGAAGCACACC	Screening
PEO1454	T-DNA <i>bicat3-1_R</i>	CTCCTATGGCGTTCTTGTGAG	Screening
PEO1645	T-DNA <i>bicat3-2_F</i>	TGAAGTTGGCGACTCACAAG	Screening
PEO1646	T-DNA <i>bicat3-2_R</i>	CATCATCACGGGTATCCACA	Screening
PEO54	GABI_pAC161-8409	ATATTGACCATCATACTCATTGC	Screening
PEO17	SALK_LB	TGGTTCACGTAGTGGGCCATCG	Screening
PEO474	<i>TUB6_F</i>	AATCGACACTTTCAGTTCATCAGC	Screening
PEO475	<i>TUB6_R</i>	ATCCTCGTCTTCTCATACTCGCC	Screening
PEO1423	<i>BICAT3_F1</i>	<u>acc</u> cgggatccATGGGTTTGATTTCAAACCCTAC	Screening
PEO1424	<i>BICAT3_R1</i>	<u>aaagt</u> cgacCTACAATGGAGGATAGAAATAGGAGG	Screening
PEO1487	qRT <i>BICAT3_F</i>	TCGCCACCATCTTCTTCCTC	Screening (qRT-PCR)
PEO1488	qRT <i>BICAT3_R</i>	AACCATTCCACGACGACCAA	Screening (qRT-PCR)
PEO045	<i>Actin2_F</i>	TCCCTCAGCACATTCCAGCAGAT	Screening (qRT-PCR)
PEO046	<i>Actin2_R</i>	AACGATTCCCTGGACCTGCCTCATC	Screening (qRT-PCR)
PEO1613	Loc <i>BICAT3_F2</i>	<u>aa</u> cccggaATGGGTTTGATTTCAAACCCTAC	colocalization
PEO1425	Loc <i>BICAT3_R2</i>	<u>acc</u> cgggCAATGGAGGATAGAAATAGGAGGA	colocalization
PEO1642	Pro <i>BICAT3_F</i>	<u>aa</u> cccggaGCCCTGTTCGTTTGCCTGT	Promoter
PEO1474	Pro <i>BICAT3_R</i>	<u>tt</u> cccggaGAGTGATCTGAGAGTTTTGCAGAT	Promoter
PEO1473	Comp <i>BICAT3_F</i>	<u>aa</u> cccggaATAACAAATGTTTACTTTGCTGTG	Complementation
PEO1610	Comp <i>BICAT3_R</i>	<u>aa</u> cccggaCACGACATCTCTCATCTCTC	Complementation
PEO2330	User Pro <i>BICAT3_F</i>	<u>GGCTTAAU</u> GCCTGTTCGTTTGCCTGTGCG	Complementation
PEO2331	User Pro <i>BICAT3_R</i>	<u>AGCCTCCTU</u> AGCAGCTGCCTCTGCGAGTGATCTGAGAGTTTTGCAGAT	Complementation
PEO2332	User <i>BICAT3-Venus_F</i>	<u>AAGGAGGCU</u> GCAGCTAAGGCTATGGGTTTGATTTCAAACCCTAC	Complementation
PEO2333	User <i>BICAT3-Venus_R</i>	<u>ATTTAGGUT</u> CAGGAGCTGGTTTTATCCCTGTACAGCT	Complementation
PEO2149	User Nos_F	<u>ACCTAAAU</u> GCACCTCCAATCCCGATCGTTCAAAC	Complementation
PEO2150	User Nos_R	<u>GGTTTAAU</u> UCCCGATCTAGTAACATAGAT	Complementation
PEO2031	<i>HvBICAT3_F1</i>	ATGCCTCGGCGCACCCCT	Cloning
PEO2034	<i>HvBICAT3_R2</i>	TTACAATGGTGGGTAGAAGTATGATGATAC	Cloning
PEO2062	USER <i>HvBICAT3_F</i>	<u>GGCTTAAU</u> ATGCCTCGGCGCACCCCT	User cloning
PEO2064	USER <i>HvBICAT3_R</i> nost	<u>GGTTTAAU</u> CAATGGTGGGTAGAAGTATGATG	User cloning
PEO2067	<i>HvBICAT3_sgRNA1_F</i>	<u>agca</u> GTCGAGCAGGAGTCCGAGCT	Target mutagenesis
PEO2068	<i>HvBICAT3_sgRNA1_R</i>	<u>aaac</u> AGCTCGGACTCCTGCTCGAC	Target mutagenesis
PEO2069	<i>HvBICAT3_sgRNA2_F</i>	<u>agca</u> CGACGAGACGTTTCATCATCG	Target mutagenesis
PEO2070	<i>HvBICAT3_sgRNA2_R</i>	<u>aaac</u> CGATGATGAACGTCCTCGTCG	Target mutagenesis
PEO2071	<i>HvBICAT3_sgRNA3_F</i>	<u>agca</u> TCGTTCCAACCTGATATCG	Target mutagenesis
PEO2072	<i>HvBICAT3_sgRNA3_R</i>	<u>aaac</u> CGATATCAGTTGGGAACGA	Target mutagenesis
PEO2094	JS1558	CAAGATCTGGCCCTTAAGGC	Screening
PEO2095	JS1132	AACGCTCTTTCTCTTAGGT	Screening
PEO2099	M13_F	GTTTTCCCAGTCACGAC	Screening
PEO2032	<i>HvBICAT3_F2</i>	ATGTTTCGTCCACACGGCG	CRISPR mutant screening
PEO2182	<i>HvBICAT3_CRISPR_R2</i>	CCAATATTCTCCAACGTCCTCCG	CRISPR mutant screening
PEO2228	zCas9-F	GCGATCAGATTCTCAAGCCG	T-DNA free mutant screening
PEO2229	zCas9-R	TTTTGCAGGTTGACGACTCG	T-DNA free mutant screening
PEO2250	<i>HvBICAT3_Bamh1_F1</i>	<u>CGGGATCC</u> ATGCCTCGGCGCACCCCT	Cloning
PEO2251	<i>HvBICAT3_EcoR1_R1</i>	<u>CGGAATTC</u> TACAATGGTGGGTAGAAGTATGATG	Cloning

8.2 List of constructs

Table 4. List of constructs used in this study.

Constructs	Plasmids	Usages	Notes
pGreenII0229-gBICAT3	pGreenII0229	Complementation of <i>bicat3-1</i> mutant	
pB1101-PrBICAT3	pB1101	<i>BICAT3</i> expression pattern analysis by GUS staining	
pLIFE5-PrBICAT3-BICAT3-Venus-tNos	pLIFE5	Pollen tube and immunogold localization experiments	
pART7-BICAT3-Venus	pART7-Venus	Sucellular localization of BICAT3	
pART7-BICAT3-mCherry	pART7-mCherry	Sucellular localization of BICAT3	
pRS416-BICAT3	pRS416	Yeast complementation	
pRS416-HvBICAT3	pRS417	Yeast complementation	
pART7-HvBICAT3-Venus	pART7-Venus user	Sucellular localization of HvBICAT3	
pMGE625 M1-sgRNA1	pMGE625 M1	Targeted mutation of HvBICAT3 in barley	Bsal-ACTA-link(M13)-pHvU3-AGCA-Bpil_ccdB-CmR_Bpil-GTTT-sgRNA scaff.impr.-GGGA-Bsal
pMGE624 M2-sgRNA2	pMGE624 M2	Targeted mutation of HvBICAT3 in barley	Bsal-CGGT-pHvU3-AGCA-Bpil_ccdB-CmR_Bpil-GTTT-sgRNA scaff.impr.-GCAC-Bsal
pMGE626 M3-sgRNA3	pMGE626 M3	Targeted mutation of HvBICAT3 in barley	Bsal-GCAC-link(JS838)-pHvU3-AGCA-Bpil_ccdB-CmR_Bpil-GTTT-sgRNA scaff.impr.-AGCG-Bsal
pMGE627 M4E-sgRNA3	pMGE627 M4E	Targeted mutation of HvBICAT3 in barley	Bsal-AGCG-pHvU3-AGCA-Bpil_ccdB-CmR_Bpil-GTTT-sgRNA scaff.impr.-GGGA-Bsal
pMGE632-sgRNAs	pMGE632	Targeted mutation of HvBICAT3 in barley	LB-35S:hpt-t35s-pZmUbi:YFP-P2A-Cas9(introns,2xNLS)-tocs-ACTA-Bsal_ccdB-CmR_Bsal-GGGA_RB
pMGE634-sgRNAs	pMGE634	Targeted mutation of HvBICAT3 in barley	pVM_YFP-Cas9(introns,2xNLS)-tocs-ACTA-Bsal_ccdB-CmR_Bsal-GGGA_RB

8.3 Media composition

Table 5. Media for *H. vulgare* tissue culture.

Compound	Callus Induction Medium (C-)	Callus Induction Medium (C+)	Shoot Induction Medium (T)	Shoot Induction Medium	Root Induction Medium (R)
	mg/L	mg/L	mg/L	(NH ₄ NO ₃ -free)	mg/L (NH ₄ NO ₃ -free)
MS Stock (Duchefa M0221)	4300	4300	2700		2700
CuSO ₄ *5H ₂ O	1.2 (5 μM)	1.2 (5 μM)	1.2 (5 μM)		0.6 (2.5 μM)
Maltose	30000	30000	62000/20000		15000/20000
Thiamine-HCl	1	1	0.4		0.4
Myo-Inositol	250	250	100		125
Caseinhydrolysate	1000	1000			500
L-proline	690	690			345
Dicamba (synthetic auxin)	2.5	2.5			
NH ₄ NO ₃			165		165
Glutamine			150/750		750
2,4-dichlorophenoxy acetic acid (2,4-D)			2.5		
6-benzylaminopurine (BAP)			1/0.1		
pH	5.9	5.9	5.6		5.9
Phytoagar	6	6	6		6
	autoclave 121°C, 2 bar, 30min				
Hygromycin		25/50	50		50
Ticarcillin + Clavulanic acid		150	150		150

Table 6. Media for *E. coli*, *A. tumefaciens*, and *S. cerevisiae* culture.

Media	Compound	Concentration
LB	Yeast extract	5 g/L
	Bactotryptone	10 g/L
	NaCl	5 g/L
	Agar-Agar Kobe I (for solid medium)	20 g/L
SOC	Trypton	20 g/L
	Yeast extract	5 g/L
	NaCl	0.58 g/L
	KCl	0.18 g/L
	add after autoclaving:	
	MgSO ₄ *7H ₂ O	20 mM
Glucose	20 mM	
YEB	Beef extract	5 g/L
	Yeast extract	1 g/L
	Casein hydrolysate	5 g/L
	Sucrose	5 g/L
	MgSO ₄ *7H ₂ O	0.49 g/L
	Agar-Agar Kobe I (for solid medium)	20 g/L
YPD	Yeast extract	10 g/L
	(Bacto) Peptone	20 g/L
	Glucose	20 g/L
	Agar-Agar Kobe I	20 g/L
SC-Uracil	(NH ₄) ₂ SO ₄	5 g/L
	Complete Supplement Mixture (CSM-URA)	0.77 g/L
	Yeast Nitrogen Base Without Amino Acids & (NH ₄) ₂ SO ₄	1.9 g/L
	Glucose	20 g/L
	Agar-Agar Kobe I (for solid medium)	20 g/L
AP medium	Glucose	2% (m/v)
	Complete supplm. mixture	0.079% (m/v)
	L-arginine	10 mM
	Agar	1.8% (m/v)
	KCl	10 mM
	H ₃ PO ₄	8 mM
	CaCl ₂ .2H ₂ O	0.2 mM
	MgSO ₄ .7H ₂ O	2 mM
	CuSO ₄ .5H ₂ O	0.16 μM
	MnSO ₄ .H ₂ O	2.4 μM
	ZnSO ₄ .7H ₂ O	1.4 μM
	KI	0.6 μM
	Na ₂ MoO ₄ .2H ₂ O	0.8 μM
	H ₃ BO ₃	81 μM
	FeCl ₃	1.2 μM
	Biotin	0.002 mg/L
	Na-pantothenate	0.4 mg/L
	Folic acid	0.002 mg/L
	Inositol	2 mg/L
	Niacine	0.4 mg/L
	p-aminobenzoic acid	0.2 mg/L
	Pyridoxine hydrochloride	0.4 mg/L
	Riboflavin	0.2 mg/L
	Thiamin hydrochloride	0.4 mg/L

Table 7. Media for *A. thaliana* and *H. vulgare* culture.

Media	Compound	Concentration
½ MS	Sucrose	2.5 g/L
	Phyto-Agar (P1003, Duchefa Biochemie)	8 g/L
	⅓ MS (M0231, Duchefa Biochemie) adjust pH to 5.8 with KOH	2.2 g/L
Self-made ½ MS	Sucrose	2.5 g/L
	Difco Agar (No.2266.1, Carl Roth)	8 g/L
	MgSO ₄ *7H ₂ O	0.75 mM
	KH ₂ PO ₄	0.62 mM
	NH ₄ NO ₃	10.31 mM
	KNO ₃	9.4 mM
	MES-NaOH (pH 5.8)	10 mM
	CoCl ₂ *6H ₂ O	0.05 µM
	CuSO ₄ *5H ₂ O	0.05 µM
	H ₃ BO ₃	50.14 µM
	KI	2.5 µM
	Na ₂ MoSO ₄ *2H ₂ O	0.52 µM
	ZnSO ₄ *4H ₂ O	18.42 µM
	Fe-EDTA	50 µM
MnSO ₄ *H ₂ O	37.88 µM	
CaCl ₂ *2H ₂ O	1.5 mM	
Hydroponic media for Arabidopsis	(NH ₄) ₂ SO ₄	0.5 mM
	KNO ₃	2 mM
	MgSO ₄ *7H ₂ O	0.5 mM
	KH ₂ PO ₄	0.3125 mM
	Fe-EDTA	42.5 µM
	CuSO ₄ *5H ₂ O	0.125 µM
	ZnSO ₄ *4H ₂ O	0.25 µM
	H ₃ BO ₃	17.5 µM
	NaMoO ₄ *2H ₂ O	0.05 µM
	CoCl ₂ *6H ₂ O	0.0025 µM
	MnSO ₄ *H ₂ O	3.5 µM
CaCl ₂ *2H ₂ O	2 mM	
	adjust pH to 5.8 with KOH	
Hydroponic media for barley	KH ₂ PO ₄	0.2 mM
	K ₂ SO ₄	0.3 mM
	MgSO ₄ *7H ₂ O	0.3 mM
	Mg(NO ₃) ₂ *6H ₂ O	0.9 mM
	Ca(NO ₃) ₂ *4H ₂ O	0.6 mM
	KNO ₃	50 µM
	Fe-Na-EDTA	50 µM
	NaMoO ₄ *2H ₂ O	0.8 µM
	ZnCl ₂	0.7 µM
	CuSO ₄ *5H ₂ O	0.8 µM
	H ₃ BO ₃	2 µM
	MnSO ₄ *H ₂ O	0.1 µM
		adjust pH to 5.8 with KOH

8.4 List of chemicals

Table 8. List of chemicals used in this study.

Substance	Structure	Company	Cat. No.
2-mercaptoethanol	C_2H_6SO	Merck	15433
2-propanol	C_3H_8O	Carl Roth	T910.1
3',5'-Dimethoxy-4'-hydroxyaceto-phenon (Acetosyringon)	$C_{10}H_{12}O_4$	Sigma-Aldrich	D134406
5-Brom-4-chlor-3-indolyl- β -D-glucuronic acid (x-Gluc)	$C_{14}H_{13}BrClNO_7$	xGluc direct	P5264044
Agar-Agar, Kobe I	---	Carl Roth	5210.2
Ammonium sulfate	$(NH_4)_2SO_4$	Fluka	9980
Ampicillin sodium	$C_{16}H_{18}N_3O_4SNa$	Duchefa	A0104.0005
Aniline blue	$C_{37}H_{27}N_3Na_2O_9S_3$	Carl Roth	4002.1
BASTA	---	Bayer Crop science	---
Beaf extract	---	Carl Roth	X975.1
Biozym LE Agarose	---	Biozym Scientific	840004
Biozym Plaque agarose	---	Biozym Scientific	840101
Boric acid	H_3BO_3	Carl Roth	6943.1
Bovine serum albumin (BSA)	---	Carl Roth	T844.2
Calcium chloride dihydrate	$CaCl_2 \times 2H_2O$	Sigma-Aldrich	31307
Casein hydrolysate	---	Carl Roth	AE41.1
Chloroform	$CHCl_3$	Carl Roth	4432.1
Cobalt chloride	$CoCl_2 \times 6H_2O$	Riedel deHaen	12914
Coomassie Brilliant Blue G 250	$C_{47}H_{48}N_3NaO_7S_2$	Sigma-Aldrich	1.15444
Complete Supplement Mixture (CSM) Drop-Out: -URA	---	Formedium TM	DCS0169
Copper sulfate pentahydrate	$CuSO_4 \times 5H_2O$	Riedel deHaen	31293
Dimethylsulfoxide (DMSO)	C_2H_6OS	Carl Roth	7029.1
Dithiothreitol (DTT)	$C_4H_{10}O_2S_2$	Carl Roth	6908.3
DL-Phosphinothricin	$C_5H_{15}N_2O_4P$	Duchefa	P0159.0250
D-Sorbit	$C_6H_{14}O_6$	Carl Roth	6213.1
Ethanol	C_2H_6O	Carl Roth	9065.2
Ethylene glycol tetraacetic acid (EGTA)	$C_{14}H_{24}N_2O_{10}$	Carl Roth	3054.2
Ethylenediamintetraacetic acid (EDTA)	$C_{10}H_{16}N_2O_8$	Fluka	3680
Ferric chloride	$FeCl_3 \times 6H_2O$	Merck	3943
Gentamycin sulphate	---	Duchefa	G0124.0001
Glucose	$C_6H_{12}O_6$	Carl Roth	HN06.2
Glycerol	$C_3H_8O_3$	Carl Roth	3783.2
Glutaraldehyde	$C_5H_8O_2$	Sigma-Aldrich	G5882
Hydrochloric acid	HCl	Merck	K34997717
Hydrogen peroxide	H_2O_2	Carl Roth	8070.1
Iron-sodium EDTA	FeNaEDTA	Duchefa	E0509.1000
Iva-Val-Val-Sta-Ala-Sta (Pepstatin A)	$C_{34}H_{63}N_5O_9$	Carl Roth	2936.1
Kanamycin monosulfate	$C_{18}H_{36}N_4O_{11} \times H_2SO_4$	Carl Roth	T832.1
Leupeptin	$C_{20}H_{38}N_6O_4$	Carl Roth	CN33.2
Luminol	$C_8H_7N_3O_2$	Sigma-Aldrich	123072
Magnesium ATP	$C_{10}H_{16}N_5O_{13}P_3 \cdot xMg^{z+}$	Sigma-Aldrich	20-113
Magnesium chloride	$MgCl_2$	Merck	5833.1
Magnesium sulfate heptahydrate	$MgSO_4 \times 7H_2O$	Sigma-Aldrich	63140
Manganese sulfate	$MnSO_4 \times H_2O$	Fluka	M7634
Mannitol	$C_6H_{14}O_6$	Sigma-Aldrich	M1902
MES	$C_6H_{13}NO_4S$	Sigma-Aldrich	M2933
Murashige & Skoog salts + vitamins (MS+Vit)	---	Duchefa	M0231.0025
N-acetyl-L-Leucyl-L-leucyl-arginal (Leupeptin Hemisulfate)	$C_{20}H_{38}N_6O_4 \times 0,5H_2SO_4$	Carl Roth	CN33.1
Natriummolybdat dihydrate	$NaMoO_4 \times 2H_2O$	Carl Roth	274.1
Nitric acid	HNO_3	Carl Roth	X943.1
Nitro blue tetrazolium chloride (NBT)	$C_{40}H_{30}Cl_2N_{10}O_6$	Carl Roth	4421.3
Octoxinol 9 (Triton X-100)	$C_{14}H_{22}O(C_2H_4O)_n$ (n=9-10)	Fluka	93426
Osmium tetroxide	OsO_4	Carl Roth	8371.1
Paraformaldehyde	$(CH_2O)_n$	Carl Roth	No. 0335.1
Para-coumaric acid	$C_9H_8O_3$	Sigma-Aldrich	C9008
PBS tablet	---	Sigma-Aldrich	P4417

Phenylmethylsulfonyl fluoride (PMSF)	$C_7H_7FO_2S$	Sigma-Aldrich	78830
Phyto-agar	---	Duchefa	P1003.1000
PIPES	$C_8H_{18}N_2O_6S_2$	Sigma-Aldrich	P6757
Poly(ethylene glycol)4000 (PEG4000)	$H(OCH_2CH_2)_n OH$	Sigma-Aldrich	95904
Potassium chloride	KCl	Duchefa	P0515.1000
Potassium dihydrogen phosphate	KH_2PO_4	Fluka	60220
Potassium hexacyanoferrate	$K_3[Fe_2(CN)_6]$ (III)	Fluka	60300
Potassium hexacyanoferrate-II-Trihydrat	$K_4[Fe_2(CN)_6]$ (II) x 3 H_2O	neoLab	9570.05
Potassium hydroxide	KOH	Fluka	60375
Potassium nitrate	KNO_3	Sigma-Aldrich	P8291
Ruthenium red	$Cl_6H_{42}N_{14}O_2Ru_3 \cdot 4H_2O$	Sigma -Aldrich	R2751
Silwet L-77	---	Lehle Seeds	Vis-O2
Sodium chloride	NaCl	Carl Roth	3957.1
Sodium Dodecyl sulfate (SDS)	$NaC_{12}H_{25}SO_4$	Carl Roth	CN30.2
Sodium Hypo chlorite	NaClO	Carl Roth	9062.4
Spectinomycin dihydrochloride Pentahydrate	$C_{14}H_{24}N_2O_7 \cdot x HCl \cdot 5H_2O$	Duchefa	S0188:0005
Sucrose	$C_{12}H_{22}O_{11}$	Carl Roth	4621.1
Tris(hydroxymethyl)aminomethane (Tris)	$C_4H_{11}NO_3$	Carl Roth	AE15.2
Triton™ X-100	t-Oct- C_6H_4 -(OCH_2CH_2) _x OH, x= 9-10	Fluka	93426
Tryptone	---	Formedium™	TRP02
Uranyl acetate	$C_4H_6O_6U$	Chemapol	---
YeastExtract	---	Formedium™	YEM02
Yeast Nitrogen Base without Amino Acids & Calcium Chloride	---	Formedium™	CYN2501
Zinc sulfate heptahydrate	$ZnSO_4 \cdot 7H_2O$	Riedel deHaen	31665

8.5 List of enzymes

Table 9. List of enzymes used in this study.

Enzymes	Cut side	overhangs	Company	Cat. No.
α-amylase	---	---	Sigma Aldrich	A3403-500KU
BamHI	GGATCC	5' - GATC	New England Biolabs	R0136S
Bpil (BbsI)	GAAGAC(N) ₂	---	New England Biolabs	R3539
Bsal	GGTCTC(N) ₁	---	New England Biolabs	R3733
Cellulase Onozuka R-10	---	---	Duchefa Biochemie	C8001.0010
Cellulase Onozuka RS	---	---	Duchefa Biochemie	C8003.0001
DNase I	---	---	Omega bio-tek, USA	E1091-02
EcoRI	GAATTC	5'AATT	New England Biolabs	R3101S
ExTaq DNA polymerase	---	---	Takara	RR001
GoTaq G2 DNA Polymerase	---	---	Promega	M784B
Macerozyme R-10	---	---	Duchefa Biochemie	M8002.0010
M-MuLV reverse Transcriptase	---	---	New England Biolabs	M0253S
NotI	GCGGCCGC	5' - GGCC	New England Biolabs	R0189S
Pectolyase Y-23	---	---	Duchefa Biochemie	P8004.0001
Phusion HF DNA Polymerase	---	---	Thermo Fisher	M0530S
Phusion U Hot Start DNA Polymerase	---	---	Thermo Fisher	F555S
Protoscript II	---	---	New England Biolabs	M0368
SmaI	CCCGGG	blunt	New England Biolabs	R0141S
SuperScript ®II reverse Transcriptase	---	---	Life Technologies	18064014
Shrimp Alkaline Phosphatase	---	---	New England Biolabs	M0371S
Shrimp alkaline phosphatase (SAP)	---	---	NEB	M0371S
T4 DNA Ligase	---	---	New England Biolabs	M0202S
XmaI	CCCGGG	5' - CCGG	New England Biolabs	R0180S

9 References

Afgan E, Baker D, Batut B, van den Beek M, Bouvier D, Cech M, Chilton J, Clements D, Coraor N, Gruning BA, Guerler A, Hillman-Jackson J, Hiltemann S, Jalili V, Rasche H, Soranzo N, Goecks J, Taylor J, Nekrutenko A, Blankenberg D (2018) The Galaxy platform for accessible, reproducible and collaborative biomedical analyses: 2018 update. *Nucl Acid Res* **46**: W537-W544

Alejandro S, Cailliatte R, Alcon C, Dirick L, Domergue F, Correia D, Castaings L, Briat J-F, Mari S, Curie C (2017) Intracellular distribution of manganese by the *trans*-Golgi network transporter NRAMP2 is critical for photosynthesis and cellular redox homeostasis. *Plant Cell* **29**: 3068-3084

Alejandro S, Höller S, Meier B, Peiter E (2020) Manganese in plants: From acquisition to subcellular allocation. *Front Plant Sci* **11**: 300

Altartouri B, Bidhendi AJ, Tani T, Suzuki J, Conrad C, Chebli Y, Liu N, Karunakaran C, Scarcelli G, Geitmann A (2019) Pectin chemistry and cellulose crystallinity govern pavement cell morphogenesis in a multi-step mechanism. *Plant Physiol* **181**: 127-141

Amos RA, Pattathil S, Yang J-Y, Atmodjo MA, Urbanowicz BR, Moremen KW, Mohnen D (2018) A two-phase model for the non-processive biosynthesis of homogalacturonan polysaccharides by the GAUT1:GAUT7 complex. *J Biol Chem* **293**: 19047-19063

Amsbury S, Hunt L, Elhaddad N, Baillie A, Lundgren M, Verhertbruggen Y, Scheller HV, Knox JP, Fleming AJ, Gray JE (2016) Stomatal function requires pectin de-methyl-esterification of the guard cell wall. *Curr Biol* **26**: 2899-2906

Andresen E, Peiter E, Küpper H (2018) Trace metal metabolism in plants. *J Exp Bot* **69**: 909-954

Atmodjo MA, Hao Z, Mohnen D (2013) Evolving views of pectin biosynthesis. *Annu Rev Plant Biol* **64**: 747-779

Atmodjo MA, Sakuragi Y, Zhu X, Burrell AJ, Mohanty SS, Atwood JA, Orlando R, Scheller HV, Mohnen D (2011) Galacturonosyltransferase (GAUT)1 and GAUT7 are the core of a plant cell wall pectin biosynthetic homogalacturonan:galacturonosyltransferase complex. *Proc Natl Acad Sci USA* **108**: 20225-20230

Bacete L, Mélida H, Miedes E, Molina A (2018) Plant cell wall-mediated immunity: cell wall changes trigger disease resistance responses. *Plant J* **93**: 614-636

Basu D, Tian L, Wang W, Bobbs S, Herock H, Travers A, Showalter AM (2015) A small multigene hydroxyproline-O-galactosyltransferase family functions in arabinogalactan-protein glycosylation, growth and development in Arabidopsis. *BMC Plant Biol* **15**: 295

Basu D, Wang W, Ma S, DeBrosse T, Poirier E, Emch K, Soukup E, Tian L, Showalter AM (2015) Two hydroxyproline galactosyltransferases, GALT5 and GALT2, function in arabinogalactan-protein glycosylation, growth and development in Arabidopsis. *PLOS ONE* **10**: e0125624

Bencúr P, Steinkellner H, Svoboda B, Mucha J, Strasser R, Kolarich D, Hann S, Köllensperger G, Glössl J, Altmann F, Mach L (2005) *Arabidopsis thaliana* b1,2-xylosyltransferase: an unusual glycosyltransferase with the potential to act at multiple stages of the plant N-glycosylation pathway. *Biochem J* **388**: 515-525

Bian B, Kageshima S, Yano K, Fujiwara T, Kamiya T (2018) Screening *Arabidopsis thaliana* mutants for low sensitivity to manganese identifies novel alleles of *NRAMP1* and *PGSIP6*. *J Exp Bot* **69**: 1795-1803

Bisson C, Britton KL, Sedelnikova SE, Rodgers HF, Eadsforth TC, Viner RC, Hawkes TR, Baker PJ, Rice DW (2015) Crystal structures reveal that the reaction mechanism of imidazoleglycerol-phosphate dehydratase is controlled by switching Mn(II) coordination. *Structure* **23**: 1236-1245

Bossi JG, Kumar K, Barberini ML, Dominguez GD, Guerrero YDR, Marino-Buslje C, Obertello M, Muschietti JP, Estevez JM (2020) The role of P-type IIA and P-type IIB Ca²⁺-ATPases in plant development and growth. *J Exp Bot* **71**: 1239-1248

Both P, Sobczak L, Breton C, Hann S, Nöbauer K, Paschinger K, Kozmon S, Mucha J, Wilson IB (2011) Distantly related plant and nematode core a1,3-fucosyltransferases display similar trends in structure-function relationships. *Glycobiology* **21**: 1401-1415

Bouton S, Leboeuf E, Mouille G, Leydecker M-T, Talbotec J, Granier F, Lahaye M, Höfte H, Truong H-N (2002) *QUASIMODO1* encodes a putative membrane-bound glycosyltransferase required for normal pectin synthesis and cell adhesion in Arabidopsis. *Plant Cell* **14**: 2577-2590

Breton C, Snajdrová L, Jeanneau C, Koca J, Imberty A (2006) Structures and mechanisms of glycosyltransferases. *Glycobiology* **16**: 29R-37R

Burton RA, Gidley MJ, Fincher GB (2010) Heterogeneity in the chemistry, structure and function of plant cell walls. *Nature Chem Biol* **6**: 724-732

- Cao F-Q, Werner AK, Dahncke K, Romeis T, Liu L-H, Witte C-P** (2010) Identification and characterization of proteins involved in rice urea and arginine catabolism. *Plant Physiol* **154**: 98-108
- Carmona A, Devès G, Roudeau S, Cloetens P, Bohic S, Ortega R** (2010) Manganese accumulates within Golgi apparatus in dopaminergic cells as revealed by synchrotron X-ray fluorescence nanoimaging. *ACS Chem Neurosci* **1**: 194-203
- Chebli Y, Kaneda M, Zerzour R, Geitmann A** (2012) The cell wall of the Arabidopsis pollen tube-spatial distribution, recycling, and network formation of polysaccharides. *Plant Physiol* **160**: 1940-1955
- Chen K, Wang Y, Zhang R, Zhang H, Gao C** (2019) CRISPR/Cas genome editing and precision plant breeding in agriculture. *Annu Rev Plant Biol* **70**: 667-697
- Cheng N-H, Pittman JK, Barkla BJ, Shigaki T, Hirschi KD** (2003) The Arabidopsis *cax1* mutant exhibits impaired ion homeostasis, development, and hormonal responses and reveals interplay among vacuolar transporters. *Plant Cell* **15**: 347-364
- Cheng N-H, Pittman JK, Shigaki T, Hirschi KD** (2002) Characterization of CAX4, an Arabidopsis H⁺/cation antiporter. *Plant Physiol* **128**: 1245-1254
- Chu H-H, Car S, Socha AL, Hindt MN, Punshon T, Guerinot ML** (2017) The Arabidopsis MTP8 transporter determines the localization of manganese and iron in seeds. *Sci Rep* **7**: 11024
- Ciucanu I** (2006) Per-O-methylation reaction for structural analysis of carbohydrates by mass spectrometry. *Anal Chim Acta* **576**: 147-155
- Ciucanu I, Kerek F** (1984) A simple and rapid method for the permethylation of carbohydrates. *Carbohydr Res* **131**: 209-217
- Clough SJ, Bent AF** (1998) Floral dip: a simplified method for *Agrobacterium*-mediated transformation of *Arabidopsis thaliana*. *Plant J* **16**: 735-743
- Colinet A-S, Sengottaiyan P, Deschamps A, Colsoul M-L, Thines L, Demaegd D, Duchene M-C, Foulquier F, Hols P, Morsomme P** (2016) Yeast Gdt1 is a Golgi-localized calcium transporter required for stress-induced calcium signaling and protein glycosylation. *Sci Rep* **6**: 24282
- Connorton JM, Webster RE, Cheng N, Pittman JK** (2012) Knockout of multiple *Arabidopsis* cation/H⁺ exchangers suggests isoform-specific roles in metal stress response, germination and seed mineral nutrition. *PLOS ONE* **7**: e47455

- Cosgrove DJ** (2018) Diffuse growth of plant cell walls. *Plant Physiol* **176**: 16-27
- Culbertson AT, Ehrlich JJ, Choe J-Y, Honzatko RB, Zabolina OA** (2018) Structure of xyloglucan xylosyltransferase 1 reveals simple steric rules that define biological patterns of xyloglucan polymers. *Proc Natl Acad Sci USA* **115**: 6064-6069
- Culbertson AT, Tietze AA, Tietze D, Chou Y-H, Smith AL, Young ZT, Zabolina OA** (2016) A homology model of Xyloglucan Xylosyltransferase 2 reveals critical amino acids involved in substrate binding. *Glycobiology* **26**: 961-972
- Das S, Carmona A, Khatua K, Porcaro F, Somogyi A, Ortega R, Datta A** (2019) Manganese mapping using a fluorescent Mn²⁺ sensor and nanosynchrotron X-ray fluorescence reveals the role of the Golgi apparatus as a manganese storage site. *Inorganic Chemistry* **58**: 13724-13732
- De Lorenzo G, Ferrari S, Giovannoni M, Mattei B, Cervone F** (2019) Cell wall traits that influence plant development, immunity, and bioconversion. *Plant J* **97**: 134-147
- De Storme N, Geelen D** (2014) Callose homeostasis at plasmodesmata: molecular regulators and developmental relevance. *Front Plant Sci* **5**: 138
- Dehors J, Mareck A, Kiefer-Meyer M-C, Menu-Bouaouiche L, Lehner A, Mollet J-C** (2019) Evolution of cell wall polymers in tip-growing land plant gametophytes: composition, distribution, functional aspects and their remodeling. *Front Plant Sci* **10**: 441
- Delhaize E, Gruber BD, Pittman JK, White RG, Leung H, Miao Y, Jiang L, Ryan PR, Richardson AE** (2007) A role for the *AtMTP11* gene of *Arabidopsis* in manganese transport and tolerance. *Plant J* **51**: 198-210
- Demaegd D, Colinet A-S, Deschamps A, Morsomme P** (2014) Molecular evolution of a novel family of putative calcium transporters. *PLOS ONE* **9**: e100851
- Demaegd D, Foulquier F, Colinet AS, Gremillon L, Legrand D, Mariot P, Peiter E, Van Schaftingen E, Matthijs G, Morsomme P** (2013) Newly characterized Golgi-localized family of proteins is involved in calcium and pH homeostasis in yeast and human cells. *Proc Natl Acad Sci USA* **110**: 6859-6864
- Dickinson H, Rodriguez-Enriquez J, Grant-Downton R** (2018) Pollen germination and pollen tube growth of *Arabidopsis thaliana*: *In vitro* and semi *in vivo* methods. *Bio-protocol* **8**: e2977

Dindas J, Scherzer S, Roelfsema MRG, von Meyer K, Müller HM, Al-Rasheid KAS, Palme K, Dietrich P, Becker D, Bennett MJ, Hedrich R (2018) AUX1-mediated root hair auxin influx governs SCF^{TIR1/AFB}-type Ca²⁺ signaling. *Nat Communications* **9**: 1174

Dodd AN, Kudla J, Sanders D (2010) The language of calcium signaling. *Annu Rev Plant Biol* **61**: 593-620

Dogbo O, Laferrière A, D'Harlingue A, Camara B (1988) Carotenoid biosynthesis: isolation and characterization of a bifunctional enzyme catalyzing the synthesis of phytoene. *Proc Natl Acad Sci USA* **85**: 7054-7058

Driouich A, Follet-Gueye M-L, Bernard S, Kousar S, Chevalier L, Vitré-Gibouin M, Lerouxel O (2012) Golgi-mediated synthesis and secretion of matrix polysaccharides of the primary cell wall of higher plants. *Front Plant Sci* **3**: 79

Duan Q, Liu M-CJ, Kita D, Jordan SS, Yeh F-LJ, Yvon R, Carpenter H, Federico AN, Garcia-Valencia LE, Eyles SJ, Wang C-S, Wu H-M, Cheung AY (2020) FERONIA controls pectin- and nitric oxide-mediated male-female interaction. *Nature* **579**: 561-566

Dulary E, Yu S-Y, Houdo M, de Bettignies G, Decool V, Potelle S, Duvet S, Krzewinski-Recchi M-A, Garat A, Matthijs G, Guerardel Y, Foulquier F (2018) Investigating the function of Gdt1p in yeast Golgi glycosylation. *Biochim Biophys Act* **1862**: 394-402

Dunphy WG, Rothman JE (1985) Compartmental organization of the Golgi stack. *Cell* **42**: 13-21

Dünser K, Gupta S, Herger A, Feraru MI, Ringli C, Kleine-Vehn J (2019) Extracellular matrix sensing by FERONIA and Leucine-Rich Repeat Extensins controls vacuolar expansion during cellular elongation in *Arabidopsis thaliana*. *EMBO J* **38**: e100353

Dürr G, Strayle J, Plemper R, Elbs S, Klee SK, Catty P, Wolf DH, Rudolph HK (1998) The *medial*-Golgi ion pump Pmr1 supplies the yeast secretory pathway with Ca²⁺ and Mn²⁺ required for glycosylation, sorting, and endoplasmic reticulum-associated protein degradation. *Mol Biol Cell* **9**: 1149-1162

Ebert B, Birdseye D, Liwanag AJM, Laursen T, Rennie EA, Guo XY, Catena M, Rautengarten C, Stonebloom SH, Gluza P, Pidatala VR, Andersen MCF, Cheetamun R, Mortimer JC, Heazlewood JL, Bacic A, Clausen MH, Willats WGT, Scheller HV (2018) The three members of the Arabidopsis glycosyltransferase family 92 are functional b-1,4-galactan synthases. *Plant Cell Physiol* **59**: 2624-2636

Edmond C, Shigaki T, Ewert S, Nelson MD, Connorton JM, Chalova V, Noordally Z, Pittman JK (2009) Comparative analysis of CAX2-like cation transporters indicates functional and regulatory diversity. *Biochem J* **418**: 145-154

Egelund J, Petersen BL, Motawia MS, Damager I, Faik A, Olsen C-E, Ishii T, Clausen H, Ulvskov P, Geshi N (2006) *Arabidopsis thaliana* *RGXT1* and *RGXT2* encode Golgi-localized (1,3)- α -D-xylosyltransferases involved in the synthesis of pectic rhamnogalacturonan-II. *Plant Cell* **18**: 2593-2607

Eisenhut M, Hoecker N, Schmidt SB, Basgaran RM, Flachbart S, Jahns P, Eser T, Geimer S, Husted S, Webers APM, Leister D, Schneider A (2018) The plastid envelope CHLOROPLAST MANGANESE TRANSPORTER1 is essential for manganese homeostasis in *Arabidopsis*. *Mol Plant* **11**: 955-969

Entus R, Poling M, Herrmann KM (2002) Redox regulation of *Arabidopsis* 3-deoxy-D-*arabino*-heptulosonate 7-phosphate synthase. *Plant Physiol* **129**: 1866-1871

Eroglu S, Giehl RFH, Meier B, Takahashi M, Terada Y, Ignatyev K, Andresen E, Küpper H, Peiter E, von Wirén N (2017) Metal Tolerance Protein 8 mediates manganese homeostasis and iron re-allocation during seed development and germination. *Plant Physiol* **174**: 1633-1647

Eroglu S, Meier B, von Wirén N, Peiter E (2016) The vacuolar manganese transporter MTP8 determines tolerance to iron deficiency-induced chlorosis in *Arabidopsis*. *Plant Physiol* **170**: 1030-1045

Feng W, Kita D, Peaucelle A, Cartwright HN, Doan V, Duan Q, Liu M-C, Maman J, Steinhorst L, Schmitz-Thom I, Yvon R, Kudla J, Wu H-M, Cheung AY, Dinneny JR (2018) The FERONIA receptor kinase maintains cell wall integrity during salt stress through Ca^{2+} signaling. *Curr Biol* **28**: 666-675

Foulquier F, Amyere M, Jaeken J, Zeevaert R, Schollen E, Race V, Bammens R, Morelle W, Rosnoblet C, Legrand D, Demaegd D, Buist N, Cheillan D, Guffon N, Morsomme P, Annaert W, Freeze HH, Van Schaftingen E, Vikkula M, Matthijs G (2012) TMEM165 deficiency causes a congenital disorder of glycosylation. *The American Journal of Human Genetics* **91**: 15-26

Foulquier F, Legrand D (2020) Biometals and glycosylation in humans: Congenital disorders of glycosylation shed lights into the crucial role of Golgi manganese homeostasis. *Biochim Biophys Acta* **1864**: 129674

Franck CM, Westermann J, Boisson-Dernier A (2018) Plant malectin-like receptor kinases: from cell wall integrity to immunity and beyond. *Annu Rev Plant Biol* **69**: 301-328

Frank J, Happeck R, Meier B, Hoang MTT, Stribny J, Hause G, Ding H, Morsomme P, Baginsky S, Peiter E (2019) Chloroplast-localized BICAT proteins shape stromal calcium signals and are required for efficient photosynthesis. *New Phytol* **221**: 866-880

Gaillochet C, Develtere W, Jacobs TB (2021) CRISPR screens in plants: approaches, guidelines, and future prospects. *Plant Cell* **33**: 794-813

Gao H, Xie W, Yang C, Xu J, Li J, Wang H, Chen X, Huang C-F (2018) NRAMP2, a trans-Golgi network-localized manganese transporter, is required for *Arabidopsis* root growth under manganese deficiency. *New Phytol* **217**: 179-193

Garcia-Gimenez G, Barakate A, Smith P, Stephens J, Khor SF, Doblin MS, Hao P, Bacic A, Fincher GB, Burton RA, Waugh R, Tucker MR, Houston K (2020) Targeted mutation of barley (1,3;1,4)-b-glucan synthases reveals complex relationships between the storage and cell wall polysaccharide content. *Plant J* **104**: 1009-1022

Garcia-Rodriguez N, Manzano-Lopez J, Munoz-Bravo M, Fernandez-Garcia E, Muniz M, Wellinger RE (2015) Manganese redistribution by calcium-stimulated vesicle trafficking bypasses the need for P-type ATPase function. *J Biol Chem* **290**: 9335-9347

Gasparis S, Kala M, Przyborowski M, Lyznik LA, Orczyk W, Nadolska-Orczyk A (2018) A simple and efficient CRISPR/Cas9 platform for induction of single and multiple, heritable mutations in barley (*Hordeum vulgare* L.). *Plant Methods* **14**: 111

Gerasimova SV, Hertig C, Korotkova AM, Kolosovskaya EV, Otto I, Hiekel S, Kochetov AV, Khlestkina EK, Kumlehn J (2020) Conversion of hulled into naked barley by Cas endonuclease-mediated knockout of the *NUD* gene. *BMC Plant Biol* **20**

Gigli-Bisceglia N, Engelsdorf T, Hamann T (2020) Plant cell wall integrity maintenance in model plants and crop species-relevant cell wall components and underlying guiding principles. *Cell Mol Life Sci* **77**: 2049-2077

Gigli-Bisceglia N, Van Zelm E, Huo W, Lamers J, Testerink C (2020) Salinity stress-induced modification of pectin activates stress signaling pathways and requires HERK/THE and FER to attenuate the response. *bioRxiv*: 2020.2012.2018.423458

Gustin JL, Zanis MJ, Salt DE (2011) Structure and evolution of the plant cation diffusion facilitator family of ion transporters. *BMC Evol Biol* **11**: 76

Haas KT, Wightman R, Meyerowitz EM, Peaucelle A (2020) Pectin homogalacturonan nanofilament expansion drives morphogenesis in plant epidermal cells. *Science* **367**: 1003-1007

Hawes C, Satiat-Jeunemaitre B (2005) The plant Golgi apparatus - going with the flow. *Biochim Biophys Acta* **1744**: 93-107

He J, Rössner N, Hoang MTT, Alejandro S, Peiter E (2021) Transport, functions, and interaction of calcium and manganese in plant organellar compartments. *Plant Physiol* DOI: [10.1093/plphys/kiab122](https://doi.org/10.1093/plphys/kiab122)

Hellens RP, Edwards EA, Leyland NR, Bean S, Mullineaux PM (2000) pGreen: a versatile and flexible binary Ti vector for *Agrobacterium*-mediated plant transformation. *Plant Mol Biol* **42**: 819-832

Hepler PK, Rounds CM, Winship LJ (2013) Control of cell wall extensibility during pollen tube growth. *Mol Plant* **6**: 998-1017

Herridge RP, Day RC, Baldwin S, Macknight RC (2011) Rapid analysis of seed size in *Arabidopsis* for mutant and QTL discovery. *Plant Methods* **7**: 3

Hirschi KD, Korenkov VD, Wilganowski NL, Wagner GJ (2000) Expression of *Arabidopsis* CAX2 in tobacco. Altered metal accumulation and increased manganese tolerance. *Plant Physiol* **124**: 125-133

Hoecker N, Leister D, Schneider A (2017) Plants contain small families of UPF0016 proteins including the PHOTOSYNTHESIS AFFECTED MUTANT71 transporter. *Plant Signal Behav* **12**: e1278101

Holme IB, Wendt T, Gil-Humanes J, Deleuran LC, Starker CG, Voytas DF, Brinch-Pedersen H (2017) Evaluation of the mature grain phytase candidate *HvPAPhy_a* gene in barley (*Hordeum vulgare* L.) using CRISPR/Cas9 and TALENs. *Plant Mol Biol* **95**: 111-121

Holzwardt E, Wanke F, Glöckner N, Höfte H, Harter K, Wolf S (2020) A mutant allele uncouples the brassinosteroid-dependent and independent functions of BRASSINOSTEROID INSENSITIVE 1. *Plant Physiol* **182**: 669-678

Houdou M, Lebretonchel E, Garat A, Duvet S, Legrand D, Decool V, Klein A, Ouzzine M, Gasnier B, Potelle S, Foulquier F (2019) Involvement of thapsigargin- and cyclopiazonic acid-sensitive pumps in the rescue of TMEM165-associated glycosylation defects by Mn²⁺. *FASEB J* **33**: 2669-2679

Huby E, Napier JA, Baillieul F, Michaelson LV, Dhondt-Cordelier S (2020) Sphingolipids: towards an integrated view of metabolism during the plant stress response. *New Phytol* **225**: 659-670

Hunter K, Kimura S, Rokka A, Tran HC, Toyota M, Kukkonen JP, Wrzaczek M (2019) CRK2 enhances salt tolerance by regulating callose deposition in connection with PLDa1. *Plant Physiol* **180**: 2004-2021

Ischebeck T, Stenzel I, Heilmann I (2008) Type B phosphatidylinositol-4-phosphate 5-kinases mediate *Arabidopsis* and *Nicotiana tabacum* pollen tube growth by regulating apical pectin secretion. *Plant Cell* **20**: 3312-3330

Jefferson RA, Kavanagh TA, Bevan MV (1987) GUS fusions: beta-glucuronidase as a sensitive and versatile gene fusion marker in higher plants. *EMBO J* **6**: 3901-3907

Jiang Z, Zhou X, Tao M, Yuan F, Liu L, Wu F, Wu X, Xiang Y, Niu Y, Liu F, Li C, Ye R, Byeon B, Xue Y, Zhao H, Wang H-N, Crawford BM, Johnson DM, Hu C, Pei C, Zhou W, Swift GB, Zhang H, Tuan V-D, Hu Z, Siedow JN, Pei Z-M (2019) Plant cell-surface GIPC sphingolipids sense salt to trigger Ca²⁺ influx. *Nature* **572**: 341-346

Johnson MA, Harper JF, Palanivelu R (2019) A fruitful journey: pollen tube navigation from germination to fertilization. *Annu Rev Plant Biol* **70**: 809-837

Johnson NA, Liu FL, Weeks PD, Hentzen AE, Kruse HP, Parker JJ, Laursen M, Nissen P, Costa CJ, Gatto C (2009) A tomato ER-type Ca²⁺-ATPase, LCA1, has a low thapsigargin-sensitivity and can transport manganese. *Arch Biochem Biophys* **481**: 157-168

Kamer KJ, Sancak Y, Fomina Y, Meisel JD, Chaudhuri D, Grabarek Z, Mootha VK (2018) MICU1 imparts the mitochondrial uniporter with the ability to discriminate between Ca²⁺ and Mn²⁺. *Proc Natl Acad Sci USA* **115**: E7960-E7969

Kapusi E, Corcuera-Gómez M, Melnik S, Stoger E (2017) Heritable genomic fragment deletions and small indels in the putative ENGase gene induced by CRISPR/Cas9 in barley. *Front Plant Sci* **8**: 540

Kim S-J, Held MA, Zemelis S, Wilkerson C, Brandizzi F (2015) CGR2 and CGR3 have critical overlapping roles in pectin methylesterification and plant growth in *Arabidopsis thaliana*. *Plant J* **82**: 208-220

Kim SA, Punshon T, Lanzirotti A, Li LT, Alonso JM, Ecker JR, Kaplan J, Gueriot ML (2006) Localization of iron in *Arabidopsis* seed requires the vacuolar membrane transporter VIT1. *Science* **314**: 1295-1298

Klaassen MT, Trindade LM (2020) RG-I galactan side-chains are involved in the regulation of the water-binding capacity of potato cell walls. *Carbohydrate Polymers* **227**

Knott GJ, Doudna JA (2018) CRISPR-Cas guides the future of genetic engineering. *Science* **361**: 866-869

Kobayashi K (2016) Role of membrane glycerolipids in photosynthesis, thylakoid biogenesis and chloroplast development. *Journal of Plant Research* **129**: 565-580

Kohorn BD, Kohorn SL (2012) The cell wall-associated kinases, WAKs, as pectin receptors. *Front Plant Sci* **3**: 88

Krieger-Liszkay A, Thomine S (2018) Importing manganese into the chloroplast: many membranes to cross. *Mol Plant* **11**: 1109-1111

Kumar N, Galli M, Ordon J, Stuttmann J, Kogel K-H, Imani J (2018) Further analysis of barley MORC1 using a highly efficient RNA-guided Cas9 gene-editing system. *Plant Biotechnol J* **16**: 1892-1903

Kumar S, Tamura K, Nei M (1994) MEGA: Molecular evolutionary genetics analysis software for microcomputers. *Comput Appl Biosci* **10**: 198-191

Lampert DTA, Tan L, Held MA, Kieliszewski MJ (2018) Pollen tube growth and guidance: Occam's razor sharpened on a molecular arabinogalactan glycoprotein Rosetta Stone. *New Phytol* **217**: 491-500

Lanquar V, Schnell Ramos M, Lelièvre F, Barbier-Brygoo H, Krieger-Liszkay A, Krämer U, Thomine S (2010) Export of vacuolar manganese by AtNRAMP3 and AtNRAMP4 is required for optimal photosynthesis and growth under manganese deficiency. *Plant Physiol* **152**: 1986-1999

Larkin MA, Blackshields G, Brown NP, Chenna R, McGettigan PA, McWilliam H, Valentin F, Wallace IM, Wilm A, Lopez R, Thompson JD, Gibson TJ, Higgins DG (2007) Clustal W and clustal X version 2.0. *Bioinformatics* **23**: 2947-2948

Laursen T, Stonebloom SH, Pidatala VR, Birdseye DS, Clausen MH, Mortimer JC, Scheller HV (2018) Bifunctional glycosyltransferases catalyze both extension and termination of pectic galactan oligosaccharides. *Plant J* **94**: 340-351

Lawrenson T, Shorinola O, Stacey N, Li C, Ostergaard L, Patron N, Uauy C, Harwood W (2015) Induction of targeted, heritable mutations in barley and *Brassica oleracea* using RNA-guided Cas9 nuclease. *Genome Biology* **16**: 258

LeClere S, Tellez R, Rampey RA, Matsuda SPT, Bartel B (2002) Characterization of a family of IAA-amino acid conjugate hydrolases from *Arabidopsis*. *J Biol Chem* **277**: 20446-20452

Lee JH, Won HJ, Tran PHN, Lee S-M, Kim H-Y, Jung JH (2021) Improving lignocellulosic biofuel production by CRISPR/Cas9-mediated lignin modification in barley. *GCB Bioenergy* **13**: 742-752

Li X, Chanroj S, Wu Z, Romanowsky SM, Harper JF, Sze H (2008) A distinct endosomal $\text{Ca}^{2+}/\text{Mn}^{2+}$ pump affects root growth through the secretory process. *Plant Physiol* **147**: 1675-1689

Liang F, Cunningham KW, Harper JF, Sze H (1997) ECA1 complements yeast mutants defective in Ca^{2+} pumps and encodes an endoplasmic reticulum-type Ca^{2+} -ATPase in *Arabidopsis thaliana*. *Proc Natl Acad Sci USA* **94**: 8579-8584

Liebmingner E, Hüttner S, Vavra U, Fischl R, Schoberer J, Grass J, Blaukopf C, Seifert GJ, Altmann F, Mach L, Strasser R (2009) Class I α -mannosidases are required for N-glycan processing and root development in *Arabidopsis thaliana*. *Plant Cell* **21**: 3850-3867

Liu XL, Liu LF, Niu QK, Xia CA, Yang KZ, Li R, Chen LQ, Zhang XQ, Zhou YH, Ye D (2011) MALE GAMETOPHYTE DEFECTIVE 4 encodes a rhamnogalacturonan II xylosyltransferase and is important for growth of pollen tubes and roots in *Arabidopsis*. *Plant Journal* **65**: 647-660

Long L, Persson DP, Duan F, Jorgensen K, Yuan L, Schjoerring JK, Pedas PR (2018) The iron-regulated transporter 1 plays an essential role in uptake, translocation and grain-loading of manganese, but not iron, in barley. *New Phytol* **217**: 1640-1653

Lopez-Hernandez F, Tryfona T, Rizza A, Yu XL, Harris MOB, Webb AAR, Kotake T, Dupree P (2020) Calcium binding by arabinogalactan polysaccharides is important for normal plant development. *Plant Cell* **32**: 3346-3369

Luk EE-C, Culotta VC (2001) Manganese superoxide dismutase in *Saccharomyces cerevisiae* acquires its metal co-factor through a pathway involving the Nramp metal transporter, Smf2p. *J Biol Chem* **276**: 47556-47562

Lund CH, Stenbaek A, Atmodjo MA, Rasmussen RE, Moller IE, Erstad SM, Biswal AK, Mohnen D, Mravec J, Sakuragi Y (2020) Pectin synthesis and pollen tube growth in *Arabidopsis* involves three GAUT1 Golgi-anchoring proteins: GAUT5, GAUT6, and GAUT7. *Front Plant Sci* **11**: 585774

Marschner P (2012) *Marschner's Mineral Nutrition of Higher Plants*, Ed 3rd. Elsevier, Amsterdam

Marshall WF, Young KD, Swaffer M, Wood E, Nurse P, Kimura A, Frankel J, Wallingford J, Walbot V, Qu X, Roeder AHK (2012) What determines cell size? *BMC Biology* **10**: 101

- Matsushima R, Hayashi Y, Yamada K, Shimada T, Nishimura M, Hara-Nishimura I** (2003) The ER body, a novel endoplasmic reticulum-derived structure in *Arabidopsis*. *Plant Cell Physiol* **44**: 661-666
- Meents MJ, Motani S, Mansfield SD, Samuels AL** (2019) Organization of xylan production in the Golgi during secondary cell wall biosynthesis. *Plant Physiol* **181**: 527-546
- Mei H, Cheng NH, Zhao J, Park S, Escareno RA, Pittman JK, Hirschi KD** (2009) Root development under metal stress in *Arabidopsis thaliana* requires the H⁺/cation antiporter CAX4. *New Phytol* **183**: 95-105
- Melnyk CW** (2017) Grafting with *Arabidopsis thaliana*. *Methods in Molecular Biology* **1497**: 9-18
- Millaleo R, Reyes-Diaz M, Ivanov AG, Mora ML, Alberdi M** (2010) Manganese as essential and toxic element for plants: transport, accumulation and resistance Mechanisms. *Journal of Soil Science and Plant Nutrition* **10**: 476-494
- Mills RF, Doherty ML, López-Marqués RL, Weimar T, Dupree P, Palmgren MG, Pittman JK, Williams LE** (2008) ECA3, a Golgi-localized P_{2A}-type ATPase, plays a crucial role in manganese nutrition in *Arabidopsis*. *Plant Physiol* **146**: 116-128
- Milner MJ, Seamon J, Craft E, Kochian LV** (2013) Transport properties of members of the ZIP family in plants and their role in Zn and Mn homeostasis. *J Exp Bot* **64**: 369-381
- Mohnen D** (2008) Pectin structure and biosynthesis. *Curr Opin Plant Biol* **11**: 266-277
- Mollet J-C, Leroux C, Dardelle F, Lehner A** (2013) Cell wall composition, biosynthesis and remodeling during pollen tube growth. *Plants* **2**: 107-147
- Montanini B, Blaudez D, Jeandroz S, Sanders D, Chalot M** (2007) Phylogenetic and functional analysis of the Cation Diffusion Facilitator (CDF) family: improved signature and prediction of substrate specificity. *BMC Genom* **8**: 107
- Moremen KW, Haltiwanger RS** (2019) Emerging structural insights into glycosyltransferase-mediated synthesis of glycans. *Nature Chem Biol* **15**: 853-864
- Mortimer JC, Scheller HV** (2020) Synthesis and function of complex sphingolipid glycosylation. *Trends Plant Sci* **25**: 522-524
- Nagashima Y, von Schaewen A, Koiwa H** (2018) Function of N-glycosylation in plants. *Plant Sci* **274**: 70-79

Navazio L, Formentin E, Cendron L, Szabò I (2020) Chloroplast calcium signaling in the spotlight. *Front Plant Sci* **11**: 186

Nelson BK, Cai X, Nebenführ A (2007) A multicolored set of *in vivo* organelle markers for co-localization studies in *Arabidopsis* and other plants. *Plant J* **51**: 1126-1136

Nevo Y, Nelson N (2006) The NRAMP family of metal-ion transporters. *Biochim Biophys Acta* **1763**: 609-620

Nguema-Ona E, Vicré-Gibouin M, Gotté M, Plancot B, Lerouge P, Bardor M, Driouich A (2014) Cell wall O-glycoproteins and N-glycoproteins: aspects of biosynthesis and function. *Front Plant Sci* **5**: 499

Nour-Eldin HH, Hansen BG, Norholm MHH, Jensen JK, Halkier BA (2006) Advancing uracil-excision based cloning towards an ideal technique for cloning PCR fragments. *Nucl Acid Res* **34**: e122

Ogawa-Ohnishi M, Matsubayashi Y (2015) Identification of three potent hydroxyproline O-galactosyltransferases in *Arabidopsis*. *Plant J* **81**: 736-746

Ogawa-Ohnishi M, Matsushita W, Matsubayashi Y (2013) Identification of three hydroxyproline O-arabinosyltransferases in *Arabidopsis thaliana*. *Nature Chem Biol* **9**: 726-730

Ohtsuru M, Kawatani H (1979) Studies on the myrosinase from *Wasabia japonica*: purification and some properties of Wasabi myrosinase. *Agric Biol Chem* **43**: 2249-2255

Oomen RJFJ, Wu J, Lelièvre F, Blanchet S, Richaud P, Barbier-Brygoo H, Aarts MGM, Thomine S (2009) Functional characterization of NRAMP3 and NRAMP4 from the metal hyperaccumulator *Thlaspi caerulescens*. *New Phytol* **181**: 637-650

Pagny S, Bouissonnie F, Sarkar M, Follet-Gueye ML, Driouich A, Schachter H, Faye L, Gomord V (2003) Structural requirements for *Arabidopsis* b1,2-xylosyltransferase activity and targeting to the Golgi. *Plant J* **33**: 189-203

Palma AS, Morais VA, Coelho AV, Costa J (2004) Effect of the manganese ion on human α 3/4 fucosyltransferase III activity. *Biometals* **17**: 35-43

Park YB, Cosgrove DJ (2012) Changes in cell wall biomechanical properties in the xyloglucan-deficient *xxt1/xxt2* mutant of *Arabidopsis*. *Plant Physiol* **158**: 465-475

Park YB, Cosgrove DJ (2015) Xyloglucan and its interactions with other components of the growing cell wall. *Plant Cell Physiol* **56**: 180-194

Peaucelle A, Braybrook SA, Le Guillou L, Bron E, Kuhlemeier C, Höfte H (2011) Pectin-induced changes in cell wall mechanics underlie organ initiation in *Arabidopsis*. *Curr Biol* **21**: 1720-1726

Pedas P, Schiller Stokholm M, Hegelund JN, Ladegard AH, Schjoerring JK, Husted S (2014) Golgi localized barley *MTP8* proteins facilitate Mn transport. *PLOS ONE* **9**: e113759

Pedas P, Ytting CK, Fuglsang AT, Jahn TP, Schjoerring JK, Husted S (2008) Manganese efficiency in barley: identification and characterization of the metal ion transporter HvIRT1. *Plant Physiol* **148**: 455-466

Peiter E, Montanini B, Gobert A, Pedas P, Husted S, Maathuis FJM, Blaudez D, Chalot M, Sanders D (2007) A secretory pathway-localized cation diffusion facilitator confers plant manganese tolerance. *Proc Natl Acad Sci USA* **104**: 8532-8537

Petersen BL, Egelund J, Damager I, Faber K, Jensen JK, Yang Z, Bennett EP, Scheller HV, Ulvskov P (2009) Assay and heterologous expression in *Pichia pastoris* of plant cell wall type-II membrane anchored glycosyltransferases. *Glycoconjugate J* **26**: 1235-1246

Pillai SE, Kumar C, Patel HK, Sonti RV (2018) Overexpression of a cell wall damage induced transcription factor, OsWRKY42, leads to enhanced callose deposition and tolerance to salt stress but does not enhance tolerance to bacterial infection. *BMC Plant Biol* **18**: 177

Pittman JK, Hirschi KD (2016) CAX-ing a wide net: Cation/H⁺ transporters in metal remediation and abiotic stress signalling. *Plant Biol* **18**: 741-749

Pittman JK, Shigaki T, Marshall JL, Morris JL, Cheng N-H, Hirschi KD (2004) Functional and regulatory analysis of the *Arabidopsis thaliana* CAX2 cation transporter. *Plant Mol Biol* **56**: 959-971

Potelle S, Morelle W, Dulary E, Duvet S, Vicogne D, Spriet C, Krzewinski-Recchi MA, Morsomme P, Jaeken J, Matthijs G, De Bettignies G, Foulquier F (2016) Glycosylation abnormalities in Gdt1p/TMEM165 deficient cells result from a defect in Golgi manganese homeostasis. *Hum Mol Genet* **25**: 1489-1500

Rennie EA, Ebert B, Miles GP, Cahoon RE, Christiansen KM, Stonebloom S, Khatab H, Twell D, Petzold CJ, Adams PD, Dupree P, Heazlewood JL, Cahoon EB, Scheller HV (2014) Identification of a sphingolipid a-

glucuronosyltransferase that is essential for pollen function in *Arabidopsis*. *Plant Cell* **26**: 3314-3325

Rennie EA, Hansen SF, Baidoo EEK, Hadi MZ, Keasling JD, Scheller HV (2012) Three members of the *Arabidopsis* glycosyltransferase family 8 are xylan glucuronosyltransferases. *Plant Physiol* **159**: 1408-1417

Ricachenevsky FK, Menguer PK, Sperotto RA, Williams LE, Fett JP (2013) Roles of plant metal tolerance proteins (MTP) in metal storage and potential use in biofortification strategies. *Front Plant Sci* **4**: 144

Rissel D, Heym PP, Thor K, Brandt W, Wessjohann LA, Peiter E (2017) No silver bullet - Canonical poly(ADP-ribose) polymerases (PARPs) are no universal factors of abiotic and biotic stress resistance of *Arabidopsis thaliana*. *Front Plant Sci* **8**: 59

Rohdich F, Lauw S, Kaiser J, Feicht R, Köhler P, Bacher A, Eisenreich W (2006) Isoprenoid biosynthesis in plants - 2C-methyl-D-erythritol-4-phosphate synthase (IspC protein) of *Arabidopsis thaliana*. *FEBS J* **273**: 4446-4458

Rui Y, Anderson CT (2016) Functional analysis of cellulose and xyloglucan in the walls of stomatal guard cells of *Arabidopsis*. *Plant Physiol* **170**: 1398-1419

Rui Y, Chen Y, Yi H, Purzycki T, Puri VM, Anderson CT (2019) Synergistic pectin degradation and guard cell pressurization underlie stomatal pore formation. *Plant Physiol* **180**: 66-77

Ruiz MCM, Jung HJ, Webb AAR (2020) Circadian gating of dark-induced increases in chloroplast- and cytosolic-free calcium in *Arabidopsis*. *New Phytol* **225**: 1993-2005

Saint-Jore-Dupas C, Nebenführ A, Boulaflous A, Follet-Gueye M-L, Plasson C, Hawes C, Driouich A, Faye L, Gomord V (2006) Plant N-glycan processing enzymes employ different targeting mechanisms for their spatial arrangement along the secretory pathway. *Plant Cell* **18**: 3182-3200

Schindelin J, Arganda-Carreras I, Frise E, Kaynig V, Longair M, Pietzsch T, Preibisch S, Rueden C, Saalfeld S, Schmid B, Tinevez J-Y, White DJ, Hartenstein V, Eliceiri K, Tomancak P, Cardona A (2012) Fiji: an open-source platform for biological-image analysis. *Nature Methods* **9**: 676-682

Schmidt SB, Eisenhut M, Schneider A (2020) Chloroplast transition metal regulation for efficient photosynthesis. *Trends Plant Sci* **25**: 817-828

Schmidt SB, Powikrowska M, Krogholm KS, Naumann-Busch B, Schjoerring JK, Husted S, Jensen PE, Pedas PR (2016) Photosystem II functionality in

barley responds dynamically to changes in leaf manganese status. *Front Plant Sci* **7**: 1772

Schneider A, Steinberger I, Herdean A, Gandini C, Eisenhut M, Kurz S, Morper A, Hoecker N, Ruhle T, Labs M, Flugge UI, Geimer S, Schmidt SB, Husted S, Weber APM, Spetea C, Leister D (2016) The evolutionarily conserved protein PHOTOSYNTHESIS AFFECTED MUTANT71 is required for efficient manganese uptake at the thylakoid membrane in *Arabidopsis*. *Plant Cell* **28**: 892-910

Schoberer J, Liebming E, Botchway SW, Strasser R, Hawes C (2013) Time-resolved fluorescence imaging reveals differential interactions of N-glycan processing enzymes across the Golgi stack in planta. *Plant Physiol* **161**: 1737-1754

Schoberer J, Strasser R (2011) Sub-compartmental organization of Golgi-resident N-glycan processing enzymes in plants. *Mol Plant* **4**: 220-228

Schoberer J, Strasser R (2018) Plant glyco-biotechnology. *Sem Cell Dev Biol* **80**: 133-141

Seifert GJ (2020) On the potential function of type II arabinogalactan O-glycosylation in regulating the fate of plant secretory proteins. *Front Plant Sci* **11**: 563735

Shigaki T, Pittman JK, Hirschi KD (2003) Manganese specificity determinants in the *Arabidopsis* metal/H⁺ antiporter CAX2. *J Biol Chem* **278**: 6610-6617

Shikanai Y, Yoshida R, Hirano T, Enomoto Y, Li B, Asada M, Yamagami M, Yamaguchi K, Shigenobu S, Tabata R, Sawa S, Okada H, Ohya Y, Kamiya T, Fujiwara T (2020) Callose synthesis suppresses cell death induced by low-calcium conditions in leaves. *Plant Physiol* **182**: 2199-2212

Showalter AM, Basu D (2016) Extensin and arabinogalactan-protein biosynthesis: glycosyltransferases, research challenges, and biosensors. *Front Plant Sci* **7**: 814

Silva J, Ferraz R, Dupree P, Showalter AM, Coimbra S (2020) Three decades of advances in arabinogalactan-protein biosynthesis. *Front Plant Sci* **11**: 610377

Smithers ET, Luo J, Dyson RJ (2019) Mathematical principles and models of plant growth mechanics: from cell wall dynamics to tissue morphogenesis. *J Exp Bot* **70**: 3587-3599

Spurr AR (1969) A low-viscosity epoxy resin embedding medium for electron microscopy. *J Ultrastruct Res* **26**: 31-43

Stael S (2019) Chloroplast calcium signalling quenches a thirst. *Nat Plants* **5**: 559-560

Stepka M, Ciampolini F, Charzynska M, Cresti M (2000) Localization of pectins in the pollen tube wall of *Ornithogalum virens* L. Does the pattern of pectin distribution depend on the growth rate of the pollen tube? *Planta* **210**: 630-635

Strasser R (2016) Plant protein glycosylation. *Glycobiology* **26**: 926-939

Strasser R, Bondili JS, Vavra U, Schoberer J, Svoboda B, Glössl J, Léonard R, Stadlmann J, Altmann F, Steinkellner H, Mach L (2007) A unique b 1,3-galactosyltransferase is indispensable for the biosynthesis of *N*-glycans containing Lewis a structures in *Arabidopsis thaliana*. *Plant Cell* **19**: 2278-2292

Stribny J, Thines L, Deschamps A, Goffin P, Morsomme P (2020) The human Golgi protein TMEM165 transports calcium and manganese in yeast and bacterial cells. *J Biol Chem* **295**: 3865-3874

Tartaglio V, Rennie EA, Cahoon R, Wang G, Baidoo E, Mortimer JC, Cahoon EB, Scheller HV (2017) Glycosylation of inositol phosphorylceramide sphingolipids is required for normal growth and reproduction in *Arabidopsis*. *Plant J* **89**: 278-290

Teardo E, Carraretto L, Moscatiello R, Cortese E, Vicario M, Festa M, Maso L, De Bortoli S, Cali T, Vothknecht UC, Formentin E, Cendron L, Navazio L, Szabo I (2019) A chloroplast-localized mitochondrial calcium uniporter transduces osmotic stress in *Arabidopsis*. *Nat Plants* **5**: 581-588

Thines L, Deschamps A, Sengottaiyan P, Savel O, Stribny J, Morsomme P (2018) The yeast protein Gdt1p transports Mn²⁺ ions and thereby regulates manganese homeostasis in the Golgi. *J Biol Chem* **293**: 8048-8055

Thines L, Deschamps A, Stribny J, Morsomme P (2019) Yeast as a tool for deeper understanding of human manganese-related diseases. *Genes* **10**: 545

Thines L, Stribny J, Morsomme P (2020) From the Uncharacterized Protein Family 0016 to the GDT1 family: Molecular insights into a newly-characterized family of cation secondary transporters. *Microbial Cell* **7**: 202-214

Thomine S, Lelièvre F, Debarbieux E, Schroeder JI, Barbier-Brygoo H (2003) AtNRAMP3, a multispecific vacuolar metal transporter involved in plant responses to iron deficiency. *Plant J* **34**: 685-695

Ülker B, Peiter E, Dixon DP, Moffat C, Capper R, Bouché N, Edwards R, Sanders D, Knight H, Knight MR (2008) Getting the most out of publicly available T-DNA insertion lines. *Plant J* **56**: 665-677

Veit C, Vavra U, Strasser R (2015) N-glycosylation and plant cell growth. *Methods in Molecular Biology* **1242**: 183-194

Vlcko T, Ohnoutkova L (2020) Allelic variants of CRISPR/Cas9 induced mutation in an inositol trisphosphate 5/6 kinase gene manifest different phenotypes in barley. *Plants* **9**: 195

Voiniciuc C, Günl M (2016) Analysis of monosaccharides in total mucilage extractable from *Arabidopsis* seeds. *Bio-protocol* **6**: e1801

Wagner TA, Kohorn BD (2001) Wall-associated kinases are expressed throughout plant development and are required for cell expansion. *Plant Cell* **13**: 303-318

Waight AB, Pedersen BP, Schlessinger A, Bonomi M, Chau BH, Roe-Zurz Z, Risenmay AJ, Sali A, Stroud RM (2013) Structural basis for alternating access of a eukaryotic calcium/proton exchanger. *Nature* **499**: 107-110

Walton RT, Christie KA, Whittaker MN, Kleinstiver BP (2020) Unconstrained genome targeting with near-PAMless engineered CRISPR-Cas9 variants. *Science* **368**: 290-296

Wang C, Xu W, Jin H, Zhang T, Lai J, Zhou X, Zhang S, Liu S, Duan X, Wang H, Peng C, Yang C (2016) A putative chloroplast-localized $\text{Ca}^{2+}/\text{H}^{+}$ antiporter CCHA1 is involved in calcium and pH homeostasis and required for PSII function in *Arabidopsis*. *Mol Plant* **9**: 1183-1196

Wang L, Wang W, Wang Y-Q, Liu Y-Y, Wang J-X, Zhang X-Q, Ye D, Chen L-Q (2013) *Arabidopsis* galacturonosyltransferase (GAUT) 13 and GAUT14 have redundant functions in pollen tube growth. *Mol Plant* **6**: 1131-1148

Wang Y, Li X, Fan B, Zhu C, Chen Z (2021) Regulation and function of defense-related callose deposition in plants. *Int J Mol Sci* **22**: 2393

Wei X, Guo J, Li M, Liu Z (2015) Structural mechanism underlying the specific recognition between the *Arabidopsis* state-transition phosphatase TAP38/PPH1 and phosphorylated light-harvesting complex protein Lhcb1. *Plant Cell* **27**: 1113-1127

Weraduwage SM, Kim S-J, Renna L, Anozie FC, Sharkey TD, Brandizzi F (2016) Pectin methylesterification impacts the relationship between photosynthesis and plant growth. *Plant Physiol* **171**: 833-848

Widemann E, Miesch L, Lugan R, Holder E, Heinrich C, Aubert Y, Miesch M, Pinot F, Heitz T (2013) The amidohydrolases IAR3 and ILL6 contribute to

jasmonoyl-isoleucine hormone turnover and generate 12-hydroxyjasmonic acid upon wounding in *Arabidopsis* leaves. *J Biol Chem* **288**: 31701-31714

Wu DY, N., Yamane M, Kashino-Fujii M, Sato K, Ma JF (2016) The HvNramp5 transporter mediates uptake of cadmium and manganese, but not iron. *Plant Physiol* **172**: 1899-1910

Wu H-C, Bulgakov VP, Jinn T-L (2018) Pectin methylesterases: cell wall remodeling proteins are required for plant response to heat stress. *Front Plant Sci* **9**: 1612

Wu Z, Liang F, Hong B, Young JC, Sussman MR, Harper JF, Sze H (2002) An endoplasmic reticulum-bound $\text{Ca}^{2+}/\text{Mn}^{2+}$ pump, ECA1, supports plant growth and confers tolerance to Mn^{2+} stress. *Plant Physiol* **130**: 128-137

Xie X, Ma X, Zhu Q, Zeng D, Li G, Liu YG (2017) CRISPR-GE: A convenient software toolkit for CRISPR-based genome editing. *Mol Plant* **10**: 1246-1249

Yamada K, Hara-Nishimura I, Nishimura M (2011) Unique defense strategy by the endoplasmic reticulum body in plants. *Plant Cell Physiol* **52**: 2039-2049

Yamada K, Nagano AJ, Nishina M, Hara-Nishimura I, Nishimura M (2013) Identification of two novel endoplasmic reticulum body-specific integral membrane proteins. *Plant Physiol* **161**: 108-120

Yamaguchi K, Suzuki L, Yamamoto H, Lyukevich A, Bodrova I, Los DA, Piven I, Zinchenko V, Kanehisa M, Murata N (2002) A two-component Mn^{2+} -sensing system negatively regulates expression of the *mntCAB* operon in *Synechocystis*. *Plant Cell* **14**: 2901-2913

Yang C-H, Wang C, Singh S, Fan N, Liu S, Zhao L, Cao H, Xie W, Yang C, Huang C-F (2021) Golgi-localised manganese transporter PML3 regulates *Arabidopsis* growth through modulating Golgi glycosylation and cell wall biosynthesis. *New Phytol*

Yang Q, Zhong X, Li Q, Lan J, Tang H, Qi P, Ma J, Wang J, Chen G, Pu Z, Li W, Lan X, Deng M, Harwood W, Li Z, Wei Y, Zheng Y, Jiang Q (2020) Mutation of the D-hordein gene by RNA-guided Cas9 targeted editing reducing the grain size and changing grain compositions in barley. *Food Chem* **311**: 125892

Yi H, Rui Y, Kandemir B, Wang JZ, Anderson CT, Puri VM (2018) Mechanical effects of cellulose, xyloglucan, and pectins on stomatal guard cells of *Arabidopsis thaliana*. *Front Plant Sci* **9**: 1566

Zeng W, Lampugnani ER, Picard KL, Song L, Wu A-M, Farion IM, Zhao J, Ford K, Doblin MS, Bacic A (2016) Asparagus IRX9, IRX10, and IRX14A are

components of an active xylan backbone synthase complex that forms in the Golgi apparatus. *Plant Physiol* **171**: 93-109

Zeng Z, Han N, Liu C, Buerte B, Zhou C, Chen J, Wang M, Zhang Y, Tang Y, Zhu M, Wang J, Yang Y, Bian H (2020) Functional dissection of *HGGT* and *HPT* in barley vitamin E biosynthesis via CRISPR/Cas9-enabled genome editing. *Ann Bot* **126**: 929-942

Zhang B, Zhang C, Liu C, Fu A, Luan S (2021) A Golgi-localized manganese transporter functions in pollen tube tip growth to control male fertility in *Arabidopsis*. *Plant Commun* **2**: 100178

Zhang B, Zhang C, Liu C, Jing Y, Wang Y, Jin L, Yang L, Fu A, Shi J, Zhao F, Lan W, Luan S (2018) Inner envelope CHLOROPLAST MANGANESE TRANSPORTER 1 supports manganese homeostasis and phototrophic growth in *Arabidopsis*. *Mol Plant* **11**: 943-954

Zhang D, Zhang Z, Unver T, Zhang B (2021) CRISPR/Cas: A powerful tool for gene function study and crop improvement. *J Adv Res* **29**: 207-221

Zhang GF, Staehelin LA (1992) Functional compartmentation of the Golgi apparatus of plant cells. Immunocytochemical analysis of high-pressure frozen- and freeze-substituted sycamore maple suspension culture cells. *Plant Physiol* **99**: 1070-1083

Zhao F, Chen W, Sechet J, Martin M, Bovio S, Lionnet C, Long Y, Battu V, Mouille G, Monéger F, Traas J (2019) Xyloglucans and microtubules synergistically maintain meristem geometry and phyllotaxis. *Plant Physiol* **181**: 1191-1206

Zykwinska A, Thibault J-F, Ralet M-C (2007) Organization of pectic arabinan and galactan side chains in association with cellulose microfibrils in primary cell walls and related models envisaged. *J Exp Bot* **58**: 1795-1802

10 Bibliography

10.1 Peer-reviewed publications

He J, Rössner N, Hoang MTT, Alejandro S, Peiter E (2021). Transport, functions, and interaction of calcium and manganese in plant organellar compartments. *Plant Physiology* doi: 10.1093/plphys/kiab122.

Ding H, He J, Wu Y, Wu X, Ge C, Wang Y, Zhong S, Peiter E, Liang J, Xu W (2018). The tomato mitogen activated protein kinase SIMPK1 is a negative regulator of the high temperature stress response. *Plant Physiology* **177**: 633-651.

He J, Wang Y, Ding H, Ge C (2016). Epibrassinolide confers zinc stress tolerance by regulating antioxidant enzyme responses, osmolytes, and hormonal balance in *Solanum melongena* seedlings. *Brazilian Journal of Botany* **39**: 295-303.

Wu X, He J, Ding H, Zhu Z, Chen J, Xu S, Zha D (2015). Modulation of zinc-induced oxidative damage in *Solanum melongena* by 6-benzylaminopurine involves ascorbate–glutathione cycle metabolism. *Environmental and Experimental Botany* **116**: 1-11.

Wang L, He J, Ding H, Liu H, Lü B, Liang J (2015). Overexpression of AT14A confers tolerance to drought stress-induced oxidative damage in suspension cultured cells of *Arabidopsis thaliana*. *Protoplasma* **252**: 1111-1120.

10.2 Poster presentations

He J, Meier B, Höller S, Gohlisch J, Janssen A, Peiter-Volk T, Peiter E (2019). A Golgi-localized cation transporter crucial for plant performance under limiting manganese supply.

Presented at:

- 18th International Workshop on Plant Membrane Biology, 7th-12th July 2019, Glasgow, UK

The Biochemical Society Poster prize for the best poster.

- Annual Meeting of the German Society of Plant Nutrition, 25th – 27th September 2019, Berlin, Germany

3rd prize at poster awards.

11 Curriculum Vitae

Personal data

Name	Jie He
Nationality	Chinese

Education

Since October 2016

PhD student in Plant Nutrition Laboratory, Institute of Agricultural and Nutritional Sciences, Martin Luther University Halle-Wittenberg, Germany

September 2013 – June 2016

Master in Biophysics, College of Bioscience and Biotechnology, Yangzhou University, China

September 2009 – June 2013

Bachelor in Biotechnology, College of Bioscience and Biotechnology, Yangzhou University, China

12 Acknowledgments

First of all, I want to thank China Scholar Council (CSC) for offering me financial support to study abroad, and to Deutscher Akademischer Austauschdienst (DAAD) and AGRIPOLY-DPP graduate school for providing me with scholarships for finalizing my PhD.

I want to express my special thanks to Professor Dr. Edgar Peiter for his attentive supervision. I'm really impressed by his comprehensive knowledge, dynamic and active mind, enthusiasm in science, and rigorous research attitude. Without his great ideals and divergent thinking, my project would not have gone so smoothly. I thank him for being my map in science and guide me to the right path. In addition, I appreciate him for supporting me not only in scientific works but also inspiring me to be self-confident.

Numerous thanks to my friendly colleagues and collaborators that passionately supported me all the way. I would like to thank our lab superman, Dr. Bastian Meier, for helping me whenever I needed. I thank Dr. Minh Thi Than Hoang and Dr. Santiago Alejandro Martinez for their encouragement, enlightening discussion, unending support. Thanks to Dr. Stefanie Höller and Nico Rössner for helping me with confocal microscopy. Thanks to our talented technicians, Anja Janssen, Liane Freitag, and Tina Peiter-Volk, for supporting my works. Thanks to Julia Rödiger for helping me with registrations and all the paperwork. I'm also appreciative for the great efforts from our collaborators, Dr. Dr. Gerd Hause, Dr. Catalin Voiniciuc, Dr. Bo Yang, and Dr. Johannes Stuttmann.

I am also thankful to all my friends in Germany and China, who continually stand with me no matter whether I'm happy or upset, encourage me, give me advice, communicate, and travel together, brighten my life in Germany.

Last but not least, I am grateful that my parents strengthened me with their love and put courage in my heart. I thank my fiancé and his parents for giving me complete understanding and support. Without your support, I cannot be here without worries to finish my PhD studies.

13 Declaration under Oath

Eidesstattliche Erklärung / Declaration under Oath*

Ich erkläre an Eides statt, dass ich die Arbeit selbstständig und ohne fremde Hilfe verfasst, keine anderen als die von mir angegebenen Quellen und Hilfsmittel benutzt und die den benutzten Werken wörtlich oder inhaltlich entnommenen Stellen als solche kenntlich gemacht habe.

I declare under penalty of perjury that this thesis is my own work entirely and has been written without any help from other people. I used only the sources mentioned and included all the citations correctly both in word or content.

Datum / Date

Unterschrift des Antragstellers / Signature of the applicant